Multiwavelength Studies of Cluster Evolution from $z \sim 1$ to the Present

by

A. K. Hicks

B.A., Macalester College, 1994

M.S., Massachusetts Institute of Technology, 2001

A thesis submitted to the

Faculty of the Graduate School of the

University of Colorado in partial fulfillment

of the requirements for the degree of

Doctor of Philosophy

Department of Astrophysical and Planetary Sciences

2005

This thesis entitled:
Multiwavelength Studies of Cluster Evolution from $z \sim 1$ to the Present
written by A. K. Hicks
has been approved for the Department of Astrophysical and Planetary Sciences

Erica Ellingson

Prof. Webster Cash

Date

The final copy of this thesis has been examined by the signatories, and we find that both the content and the form meet acceptable presentation standards of scholarly work in the above mentioned discipline.

Hicks, A. K. (Ph.D., Astrophysics)

Multiwavelength Studies of Cluster Evolution from $z \sim 1$ to the Present

Thesis directed by Prof. Erica Ellingson

The characterization of clusters of galaxies at high redshift provides an important contribution to constraints on cosmological models. In particular, reliable mass estimations of cluster samples over a broad range in redshift supply essential information on the evolution of the cluster mass function, and place critical constraints on cosmological parameters (Ω_m, σ_8, and w). This thesis provides the first in depth analysis of Chandra X-ray observations of high redshift ($0.6 < z < 1.1$) optically selected clusters of galaxies from the Red-sequence Cluster Survey (RCS).

In the first chapter we present a detailed Chandra analysis of the Canadian Network for Observational Cosmology (CNOC) cluster sample. These are moderate redshift ($0.17 < z < 0.55$) X-ray selected clusters, and their analysis sets the stage for comparisons between optical and X-ray selection, investigations of cluster redshift evolution, and initial calibrations of optical richness as a predictor of global cluster properties. We also confirm the reliability of X-ray mass determinations by direct comparison to alternate methods.

Following chapters supply a thorough X-ray investigation of the properties of RCS clusters, high z mass comparisons, and the characterization of optical richness as a mass estimator at high redshift. Chandra observations of RCS clusters are presented in Chapter 3. The next chapter details a comprehensive Chandra analysis of the lensing cluster RCS0224-0002. Chapter 5 presents comparisons of independent mass estimations for RCS clusters from optical richness, Sunyaev Zeldovich (SZ) observations, and X-ray analysis.

The major findings of this work are numerous and varied, but our most significant

results can be summarized as follows. High redshift optically selected clusters exhibit smaller gas mass fractions than their lower redshift X-ray selected counterparts, due to high entropy of their gaseous components. RCS clusters exhibit a wide array of dynamical states, from highly relaxed to formative. The propensity for the RCS survey to detect closely spaced structures along the line of sight is partially responsible for the high incidence of strong gravitational lensing found in this sample. Finally, SZ and optical richness mass estimation techniques are faced with significant challenges at high redshift, however both methods are highly promising should redshift calibrations be effectively implemented.

Dedication

To my family.

Acknowledgements

Contents

Tables

Table

Figures

Figure

Chapter 1

Introduction

"Call me Ishmael."

–Melville, 1851 [90]

Clusters of galaxies are the most immense objects in the vast ocean of the universe. They form from large-scale density perturbations in the cold dark matter that makes up the bulk of gravitating mass in the cosmos. Clusters themselves are composed mostly of this dark component, but also contain both galaxies and gas. Because of their size, they are considered to be representative of the universe as a whole, and are therefore ideal objects with which to study its history and evolution. Investigations of clusters can be performed from many vantage points. They are observable in X-ray, optical, radio, and microwave frequencies. Each of these observation methods provides us with complementary information that can be used to more thoroughly characterize these cosmologically crucial objects.

1.1 Cluster Elements

"Now the various species of whales need some sort of popular comprehensive classification, if only an easy outline one for the present, hereafter to be filled in all its departments by subsequent laborers."

–Melville, 1851 [90]

Clusters of galaxies can be defined as gravitationally bound objects that have masses ranging from $10^{14} - 10^{15}$ $M_{\odot}$. Gravitational potentials of this size heat the gaseous component of clusters to temperatures of $1 - 10$ keV ($\sim 10^7 - 10^8$ K). Lower mass clusters ($10^{12.5} - 10^{14}$ $M_\odot$) are known of as groups. Individual galaxies typically have masses below $10^{12.5}$. The composition of cluster mass is described below.

1.1.1 Galaxy Content

Clusters of galaxies generally contain between 20 and 1000 galaxies, concentrated in a region with a radius of about 1.5 h_{70}^{-1} Mpc. The distribution of galaxies in a cluster is typical of a relaxed system in gravitational equilibrium, and is similar to other objects that meet this criterion, such as the distribution of stars in a globular cluster. It is often compared to that of an isothermal sphere, and modeled as:

$$N(R) = N_0 \left[1 + \left(\frac{R}{R_C}\right)^2\right]^{-3/2} \tag{1.1}$$

(King, 1962 [80]), where R_C is the core radius and N_0 is the central density. The velocities of the galaxies in a cluster can be quite large, ranging from 500 to 1300 km s^{-1}.

The galaxy population found in clusters differs somewhat from that of the field. In the richest clusters, 75% are elliptical or S0 galaxies, in contrast to about 30% in the field. Large, dynamically relaxed clusters often contain a giant cD elliptical galaxy at or near the center of the potential well. cD galaxies are typically more extended than normal ellipticals, and very luminous, with luminosities of about $10^{11} L_\odot$ in the B band, and bolometric X-ray luminosities of order 10^{43} ergs s^{-1}.

The luminosity function (LF) of a cluster describes the distribution of luminosities within its galactic population. This is most commonly expressed via the Schecter function (Schecter 1976 [108]):

$$n(L)\ dL = N^*(L/L^*)^{-a}\ \exp(-\mathrm{L/L^*})\mathrm{d(L/L^*)} \tag{1.2}$$

Where $n(L)\,dL$ is the number of galaxies with luminosities between L and $L+dL$, L^* is a characteristic luminosity (usually corresponding to an absolute magnitude of $M^*_{B_j} = -20.16$) and the slope α is typically around 1.2 (Girardi et al. 2000 [59]). The total number of galaxies diverges at low L, however the integral of this function is finite and can be used to obtain the total optical luminosity of a cluster.

1.1.2 Dark Matter

In 1937 Zwicky [127] first reported that the measured velocity dispersion of the Coma cluster was much higher than could be attributed to only the mass of the luminous matter. This finding was the first observational evidence of dark matter, heralding a new age in observational cosmology. It is called "dark" matter because it does not emit light and is therefore unobservable other than through its gravitational effects on the luminous matter around it.

X-ray, dynamical, and lensing observations of clusters have shown that dark matter makes up about 90% of their mass. Therefore clusters are dominated by their dark matter component. Its gravitational potential sets both the velocity dispersion of the galaxies and the temperature of the hot gas. The distribution of the dark matter is slightly more concentrated than that of the galaxies, because dark matter has an extremely low cross section for self interaction. This distribution is usually modeled by an NFW profile (Navarro, Frenk, and White 1997 [95]):

$$\frac{\rho(r)}{\rho_{\rm crit}} = \frac{\delta_c}{(r/r_s)(1+r/r_s)^2} \tag{1.3}$$

where δ_c is a characteristic density, r_s is a scale radius, and $\rho_{\rm crit} = 3H(z)^2/8\pi{\rm G}$ is the critical density of the universe.

1.1.3 Hot Gas

In the 1960's, significant X-ray emission was observed to emanate from clusters of galaxies (Byram et al. 1966 [19]). Scientists initially found the source of this emission puzzling, however instrumental improvements in the 1970's brought about the detection of ionized He-like iron in cluster X-ray emission (Mitchell, Culhane, Davison, and Ives 1976 [91]). These discoveries made it clear that the emission was being produced by gas that had been heated to X-ray emitting temperatures by adiabatic compression during its fall into the cluster potential well. The hot plasma that permeates clusters of galaxies is called the intra cluster-medium (ICM).

The X-ray emission of clusters of galaxies is generally fit with a thermal bremsstrahlung model. The high temperatures resulting from these fits indicate that the gas exists in thermal equilibrium with the cluster galaxies. Metallicities of the ICM are of the order of 0.3 solar, confirming that the gas in clusters is enriched by processed material from stars. A more detailed treatment of the properties of the X-ray emitting gas in clusters is given in Section 1.3

1.1.4 Groups

Groups of galaxies are, in essence, scaled down versions of clusters. They are made up of tens rather than hundreds of galaxies. They are often (somewhat arbitrarily) distinguished from clusters by criteria such as having velocity dispersions of less than 500 km s^{-1}, $L_X < 10^{43}$ erg s^{-1}, $M_{tot} < 5 \times 10^{13}$ $M_{\odot}$, and/or kT< 3 keV. They are often filled with hot gas, like clusters, however the gas is more likely to be influenced by energy injection from supernovae or AGN, which can raise the entropy of the gas and even cause it to be expelled from the gravitational potential.

1.2 Cluster Surveys and Cosmological Context

"Already we are boldly launched upon the deep; but soon we shall be lost in its unshored, harborless immensities."

–Melville, 1851 [90]

Since their discovery, clusters of galaxies have continuously been sought in larger numbers and at higher redshifts. The motivation for these relentless searches is manifold. Clusters of galaxies are by themselves interesting objects - the goal of studying the characteristics, variations, and evolution of the largest gravitationally bound objects in the universe stands alone.

Clusters are also an important source of information about the underlying cosmology of the universe, for two main reasons. First, because their deep gravitational potentials retain all of their gaseous material despite energy injections by active galactic nuclei (AGN) and supernovae, they are model environments in which to study galaxy formation and evolution. Secondly, clusters are the largest objects for which we can obtain accurate mass estimates. Through these we are able to investigate the amount of structure in the universe on large scales. By comparing current mass distributions to those at higher redshifts (i.e. in the past), we can also measure the rate of structure formation, which provides an enormous contribution toward constraining cosmological models. Some of the most important cosmological parameters for which cluster studies have relevance include Ω_m, σ_8, and w.

Ω_m represents the contribution of mass (baryonic + dark) to the energy density of the universe. We already know the mean baryon density of the universe from chemical abundances, therefore if we can accurately measure the relationship between baryonic and dark mass, we are also measuring Ω_m. Because rich clusters retain their entire primordial gaseous component, it is believed that measurements of the fraction of gas mass to total mass in clusters is a good proxy for that of the entire universe. Everything we know about the universe indicates that it is flat (i.e. $\Omega_m + \Omega_\Lambda = 1$; Bahcall et al. 1999 [12]), therefore determining Ω_m also gives us Ω_Λ. Recent determinations of Ω_m (~ 0.3) indicate that the dark energy component, Ω_Λ, currently dominates the total energy density of the universe.

The existence of everything that we know of, in fact our very existence itself, is only possible because the very early universe was not perfectly homogeneous. That is, the matter density of the early universe was slightly lumpy. These lumps then grew into the structures that we see today. The initial shape of the density perturbation spectrum has been parameterized and predictions for its evolution have been made based on inflationary theory. The normalization of the density perturbation spectrum, σ_8 (pertaining to mass perturbations on scales of 8 h^{-1} Mpc), must be determined observationally (Voit 2004 [116]). Modeling the growth of the power spectrum, $D(z)$, also requires observations. $D(z)$ is a well defined function of Ω_m, Ω_Λ, and w. Of these, w, the dark energy equation of state ($P = w\rho c^2$) is the least well constrained.

Constraints can be placed on these parameters through accurate determinations of the cluster mass function and its evolution (e.g. Eke et al. 1998 [37]; Bahcall, Fan & Cen 1997 [11]). The cluster mass function, $n_M(M)$, represents the number of clusters of mass greater than M in a given (comoving) volume. It is therefore the goal of precisely determining the cluster mass function over a significant range in redshift that drives many contemporary cluster surveys.

Because clusters have a detectable signature in many wavebands, there are a number of methods for finding them. The two approaches that are currently most commonly applied, and which are most pertinent to this thesis, are optical and X-ray detection methods. A description of their respective strengths and weaknesses is given in detail below.

1.2.1 X-ray Surveys

The earliest detections of clusters in the X-ray came from objects that were discovered via optical techniques. It soon became clear that X-ray surveys were a reliable (if expensive) way to expand our sample of known clusters. X-ray surveys have the advantage of being untroubled by the projection effects that have consistently plagued optical surveys. The detection of extended X-ray emission provides direct evidence of the deep gravitational wells characteristic of massive clusters.

X-ray surveys often can be placed into one of two categories: shallow, low redshift surveys that cover wide areas of the sky, or deep searches that are very small in area but cover broader ranges in redshift. Examples of the first type of survey include the ROSAT Brightest Cluster Sample (BCS; Ebeling et al. 1998 [34]), the RASS1 survey (DeGrandi et al. 1999 [42]), and the Northern ROSAT All-Sky Galaxy Cluster Survey (NORAS; Bohringer at al. 2000 [10]). These surveys cover nearly the entire sky, excepting the galactic plane, and consist of several hundred clusters extending to a redshift of ~ 0.3. Deep surveys are often serendipitous and based on the detection of extended X-ray emission in observations that have been targeted on other objects. The most recognizable example of this type of survey may be the Einstein Observatory Extended Medium-Sensitivity Survey (EMSS; Gioia et al. 1990a [58]), which uncovered ~ 100 clusters in fields observed by the Einstein satellite, and produced the 14 moderate-redshift clusters that we investigate in this thesis. Other examples of this type of survey include the RDCS survey (Rosati et al. 1998 [103]), the CfA 160 deg^2 Survey (Vikhlinin et al. 1998 [115], SHARC (Romer et al. 2000 [39]), XMM-LSS (Valtchanov et al. 2004 [114]), and ChaMP (Wilkes et al. 2000 [121]).

X-ray surveys were initially challenged by poor spatial resolution, sometimes confusing extended sources with closely spaced groups of point sources. With the launch of satellites with improved spatial resolution such as Chandra and XMM, this no longer poses a significant problem. However X-ray surveys still rely somewhat on optical spectroscopic follow-up of cluster member galaxies to provide redshifts for the objects.

1.2.2 Optical Surveys

Clusters of galaxies, as the name implies, were first defined as overdensities in the spatial distribution of galaxies. Optical identification of clusters generally involves the specification of a threshold galactic surface density enhancement within a particular area. In other words, a detection is defined by the identification of a specific number of galaxies within a certain radius. This definition is also a simple explanation of the optical richness of a cluster. In addition to richness limits, to create a statistically complete sample optical surveys must also specify a limiting magnitude and redshift, because galaxies grow fainter with increasing distance and in a given cluster the number of galaxies increases with decreasing brightness.

The first and most well-known catalogue of rich clusters was created by Abell (1958) [1] from plates taken from the Palomar Observatory Sky Survey (POSS). Abell identified, by eye, clusters that met the criteria of having at least 50 bright galaxies within 3 h_{50}^{-1} Mpc, within the redshift range $0.02 < z < 0.2$ and a magnitude range of m_3 to $m_3 + 2$ (m_3 being the magnitude of the third brightest galaxy in the cluster). His completed catalogues contain thousands of clusters.

Other catalogues which were created via optical selection include The Catalogue of Galaxies and Clusters of Galaxies (CGCG; Zwicky et al 1969 [128]), and Hickson Compact Groups (HCGs; Hickson 1982 [74]), both of which were also compiled from POSS plates. More recently, optical surveys have begun to use CCD imaging and automated finding algorithms. Postman et al. (1996) [100] identified 79 clusters by the simultaneous use of positional and photometric data.

The primary challenge that optical surveys have faced is that they are susceptible to false identification due to galaxies that lie in front of or behind a cluster candidate but along the same line of sight (i.e. projection). In cases of poor clusters and objects at high redshift, this difficulty becomes particularly prominent. This has been one of the main motivations behind carrying out surveys in other wavelengths.

1.2.2.1 The Red-sequence Cluster Survey

In spite of the challenge posed by projection effects, optical selection techniques have continued to improve. One of the most recent advancements in the optical detection of clusters involves combining our knowledge of the galaxy population in clusters with the use of color filters to provide added contrast between cluster members and foreground/background galaxies.

Cosmologically, density perturbations on a given length scale collapse at similar times. Therefore the galaxies that exist in the centers of clusters can be roughly assumed to be the same age (depending, of course on the redshift that they are observed at). We have already mentioned that clusters have a much higher population of elliptical and S0 galaxies than the field. This is ostensibly due to the fact that the star formation of many of these galaxies has been "turned off" by some effect of the cluster potential (i.e. ram pressure stripping, mergers, tidal stripping). Since elliptical galaxies have extremely low star formation rates, they emit light mostly in the red wavelengths of the optical spectrum - red is the characteristic color of an old stellar population. Because they were formed at comparable times and their stellar populations have evolved in parallel, the color-magnitude relationship of the galaxies within a particular cluster produces a characteristic "red sequence".

The Red-sequence Cluster Survey (RCS; Gladders 2005 [63]) uses these properties of cluster member galaxies to minimize the projection effects that have traditionally plagued optical surveys. The detection of a cluster is dependent upon both an overdensity of galaxies and the detection of a red sequence. Currently there are two RCS surveys, the first (RCS1) has been completed and covers a 90 deg^2 area of the sky. The second (RCS2) is in progress and will survey 1000 deg^2.

RCS1 was performed at both the Canada-France Hawaii 3.6m Telescope (CFHT) and the Cerro Tololo Inter-American Observatory (CTIO), using R_c (centered at 6500$\mathring{A}$) and z' (centered at 9100$\mathring{A}$) filters. This filter selection optimizes the detection of clusters with redshifts in the range $0.2 < z < 1.4$ The color information (i.e. the use of two filters) also immediately provides redshift estimates for the cluster candidates which are expected to be accurate to 10%. So far the survey has identified between 3000 and 4000 clusters, 1500 of which are expected to be at least as optically rich as Abell class 0 clusters (30-49 galaxies brighter than m_3). Simulations indicate that false detection rates should be less than 5%. One of the main thrusts of this work is to characterize the cluster population that has been detected via this survey.

1.3 Cluster X-ray Properties

"It is some systemized exhibition of the whale that I would now fain put before you. Yet it is no easy task. The classification of the constituents of a chaos, nothing less is here essayed. Listen to what the best and latest authorities have laid down."

–Melville, 1851 [90]

1.3.1 Gas Distribution

In 1976 it was noticed that the spatial distribution of gas in clusters was comparable to the distribution of the galaxies (Cavaliere and Fusco-Femiano 1976 [22]). This resulted in modeling the density of the ICM with a modified King model:

$$\rho(r) = \rho_0 \left[1 + \left(\frac{r}{r_c} \right)^2 \right]^{-3\beta/2} \tag{1.4}$$

where ρ_0 is the central gas density, r_c is a characteristic core radius, and β is the asymptotic slope of the gas at large radii.

The luminosity of the ICM is the integral of the emission measure:

$$L = \int \rho^2(r)\Lambda(T)dV \tag{1.5}$$

where Λ is the cooling function of the gas for thermal bremsstrahlung in the X-ray band. Assuming isothermality, the resulting surface brightness profile is:

$$I(r) = I_0 \left[1 + \left(\frac{r}{r_c}\right)^2\right]^{-3\beta+1/2} \tag{1.6}$$

where r is the projected radius from the center of the cluster. This parameterization is commonly known as a β model. In practice, a β model is often fit to the surface brightness profile of a cluster and a central density is derived from the emission measure. With these two ingredients the density distribution of the gas can then be solved for. The total gas mass of the cluster is obtained by integrating the expression for gas density. Comparisons of cluster gas mass to the total mass in the galaxies indicate that the ICM makes up close to 80% of the total luminous matter in a cluster. Typically, the densities of clusters are of the order of 10^{-3} cm^{-3}.

1.3.2 X-ray Spectra

The main contributor to the X-ray spectra of clusters is thermal bremsstrahlung. Thermal bremsstrahlung is free-free emission and results from hot gas in thermal equilibrium interacting with itself. Its emissivity is proportional to the square of the electron density:

$$\epsilon = 6.8 \times 10^{-38} Z^2 n_e n_i T^{-1/2} e^{-h\nu/kT} g_{ff} \tag{1.7}$$

where Z is the ionic charge, n_e and n_i are the electron and ion densities ($n_i \sim n_e$), T is the temperature of the gas, and g_{ff} is the free-free Gaunt factor. Since the gas in clusters has relatively low density, and is optically thin, radiative transfer effects are negligible.

Another component of the X-ray spectra of clusters is line emission from metals in the gas ("metals" meaning anything other than hydrogen). The most prominent lines come from transitions between low lying energy levels in the K-shells ($n \rightarrow 1$) of abundant elements. Oxygen through nickel produce K-shell lines that can be found between $0.5 - 10$ keV. The equivalent width of these lines is a function of both temperature and the abundance of the elements. Examples of elements found in abundance in the ICM are oxygen, neon, magnesium, silicon, sulfur, iron and nickel.

1.3.2.1 Spectral Fitting

To extract cluster temperature and abundance information from a spectrum, the actual spectral data must be fit to a model. Though it would be ideal if this data came in the form of flux as a function of energy, $F(E)$, in actuality it is delivered from an instrument as a number of counts per detector channel I, or $C(I)$. The number of these channels over a spectral range varies from instrument to instrument, but is of the order of hundreds to thousands.

The difference between $C(I)$ and $F(E)$ primarily has to do with an imperfect instrumental response. This response has two pieces, $R(E, I)$ and $A(E)$. $R(E, I)$ is a matrix that relates pulse height to photon energy. $A(E)$ contains the total effective area at each region of the detector. The total effective area contains contributions from the quantum efficiency of the detector, the filter transmission function, and the effective area of the X-ray mirror. The combined effects of the two response functions produce the photon count spectrum:

$$C(I) = \int F(E)R(E, I)A(E)dE \tag{1.8}$$

The instrument is usually calibrated with a known spectrum and the results are used to form redistribution matrix files (RMFs) and ancillary response files (ARFs), corresponding to $R(E, I)$ and $A(E)$ respectively.

Fitting of the spectrum proceeds by generating a model source spectrum, $M(E)$ and folding it through the response files to create a model spectrum:

$$C_p(I) = \int M(E)R(E,I)A(E)dE \tag{1.9}$$

after which the model spectrum is compared to the actual counts spectrum and through an iterative process the best match to the data is eventually found. In this work we use the commonly employed software package XSPEC (Arnaud 1996 [8]) to perform model generation and numerical fitting.

The determination of the best fit is done through a χ^2 minimization process. χ^2 is a measure of the goodness of a fit, described by:

$$S^2 = \Sigma \frac{(C(I) - C_p(I)))^2}{\sigma(I)^2} \tag{1.10}$$

where $\sigma(I)$ is the uncertainty of the count measurement in channel I. S^2 is characterized by the χ^2 statistic.

Acceptable fits are gauged via the reduced χ^2 of a model. χ^2_r is defined as χ^2/ν where ν is the number of degrees of freedom (in this case the number of detector channels less the number of free parameters in the fit). Reduced χ^2s of 1 are ideal. χ^2_r much less than 1 usually indicates an overestimation of errors, while χ^2_r much greater than 1 means that the model is not a particularly good representation of the data.

χ^2_r is also used to determine errors on the fit parameters of a model. One parameter is varied until the χ^2 of the fit goes up from its minimum by a particular amount. The corresponding range in the varied parameter is called the confidence interval of that parameter. Practically, it means that if the fit were repeated on data drawn from the same statistical distribution, the true value of that parameter would lie within that confidence interval. For example if a 90% confidence interval (corresponding to $\Delta\chi^2 = 2.71$) were calculated, repeated fits on data from the same distribution would result in that parameter falling into the 90% confidence interval 90% of the time.

1.3.2.2 Cooling Flows

Massive, relaxed clusters often exhibit excess emission in their cores that is not well fit by a single β model. This emission is due to a region of high gas density in the center of the cluster ($L \propto \rho^2$). High density gas cools more rapidly than low density gas, according to the equation:

$$\delta t_{cool} = \frac{3}{2}\,\frac{k}{n\;\Lambda(T)}\;\delta T \tag{1.11}$$

where n is the electron density, Λ(T) is the total emissivity of the plasma (the cooling function), and k is Boltzmann's constant. In the case of isobaric cooling, 3/2 is replaced by 5/2. A plot of the cooling function vs. temperature is given in Figure 1.1.

To put it simply, the bremsstralung emission of clusters of galaxies removes energy from the gas. This process occurs throughout the lifetime of the cluster. When the time that it takes the plasma in the center of a cluster to cool is shorter than the age of the universe, a "cooling flow" develops.

The presence of cool gas in the centers of cooling flow clusters can pose a challenge to spectral fitting, if single temperature fits to integrated spectra are attempted. Similarly, cooling flow clusters often require an adjustment to the standard β model to adequately model their surface brightness profiles. For these reasons, all of the clusters in our sample that exhibit central cooling have been treated slightly differently than those which do not exhibit cooling. The particulars of this treatment are given in the individual chapters.

The details of how thoroughly the gas cools, where the cooled material goes, whether alternative sources of energy in the clusters (AGN, etc.) are sufficient to curtail the complete cooling of the gas, are still being actively investigated and are not required in detail for the scope of this work.

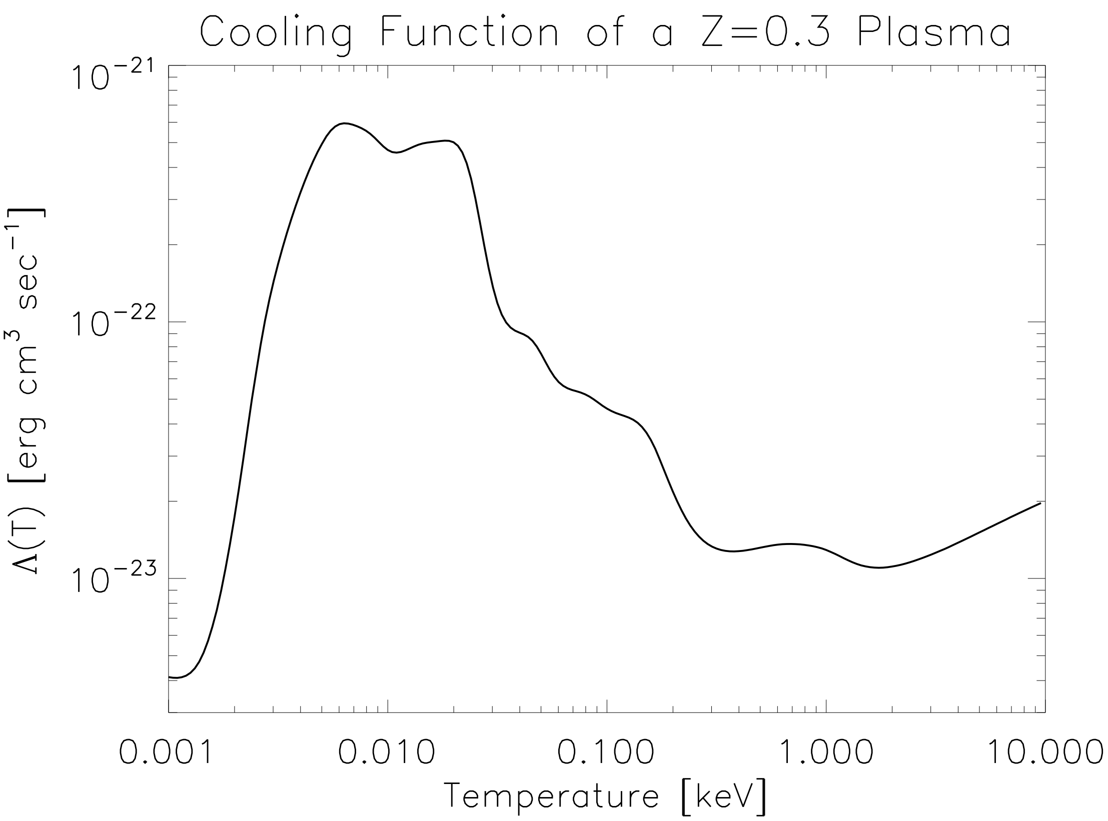

Figure 1.1 This plot shows the cooling function for a 0.3 solar abundance plasma. At temperatures below 2 keV, line cooling begins to dominate, and is responsible for the inflection in the cooling curve at low temperature.

1.3.3 Hydrostatic Equilibrium and Cluster Mass

Since the sound crossing time of clusters is much shorter than the age of the universe, the gas can be treated as a hydrostatic fluid (Sarazin 1988 [107]), where:

$$\Delta P_{\mathrm{gas}} = -\rho_g \Delta\phi \tag{1.12}$$

can be used to describe the spatial structure of the gas. Under the assumption of spherical symmetry this becomes:

$$\frac{1}{\rho_g}\frac{dP}{dr} = -\frac{d\phi}{dr} = -\frac{GM(r)}{r^2} \tag{1.13}$$

where ϕ is the gravitational potential and $M(r)$ is the mass interior to the radius r. Because of the low density of the gas we can assume a perfect gas law, $P = \rho_g kT/\mu m_p$ where ρ_g is the gas number density, m_p is the mass of a proton, $\mu = 0.6$ is the mean molecular weight of the gas, and T is the gas temperature. Combining this with Equation 1.13, one gets:

$$M(<r) = -\frac{kT}{G\mu m_p}\, r \left[\frac{d\ \log\ \mathrm{T(r)}}{d\ \log\ \mathrm{r}} + \frac{d\ \log\ \rho_{\mathrm{g}}(\mathrm{r})}{d\ \log\ \mathrm{r}}\right] \tag{1.14}$$

which gives the total mass of the cluster as a function of density and temperature.

1.3.4 Other Mass Predictors

Alternate approaches to predicting cluster mass that are pertinent to this thesis include those involving velocity dispersions, weak lensing, the Sunyaev Zeldovich (SZ) effect, and optical richness. In general these estimates have been provided through collaborations for the purpose of comparison, so they will only briefly be described here.

1.3.4.1 Velocity Dispersion

The velocity distribution of galaxies in a relaxed cluster tends to follow a Gaussian distribution. It is conventionally characterized by the radial velocity dispersion of the galaxies, σ_r, which is defined as:

$$\sigma_r = \left\langle (v_r - < v_r >)^2 \right\rangle^{1/2} \tag{1.15}$$

where v_r is the velocity of a galaxy along the line of sight. Because velocities of galaxies in a cluster reflect the depth of the cluster potential well, the total mass of a cluster can be estimated from its velocity dispersion via the virial theorem ($2U + T = 0$; where U is the potential energy and T represents kinetic energy). In its simplest form, the equation for the virial mass of a cluster is:

$$M_{\rm vir} = \frac{3}{G}\sigma_r^2 r_{\rm vir} \tag{1.16}$$

where $r_{\rm vir}$ represents the virial radius of the system, in essence the boundary which separates the region of the cluster which is in hydrostatic equilibrium from any matter which continues to fall into the cluster potential. Under the assumption that the velocities of the galaxies are uncorrelated to their position (i.e. $\sigma_r(r) = \sigma_r$), both σ_r and $r_{\rm vir}$ can be calculated from observations of the galaxy distribution.

Assumptions inherent in this technique are that velocity distributions are isotropic, and that the mass of the cluster is distributed in the same way as the galaxies (i.e. mass follows light). Also, to accurately estimate the mass of the cluster, galaxies out to the virial radius must be sampled in the measurement of velocity dispersions.

1.3.4.2 Weak Lensing

In 1937 Zwicky first proposed that cluster masses could be measured from the gravitational lensing of background objects (Zwicky 1937 [127]). Only recently has the application of this technique become feasible. The basic idea behind gravitational lensing is that, because of their large masses, clusters deflect the photons emitted by background galaxies toward our line of sight. This results in a slight distortion of the image of the background galaxy. Because the exact shape of each unlensed galaxy is unknown, observers obtain weak lensing information by measuring the distortion of an entire field of background galaxies.

Lensing is sensitive to all of the mass within a given projected radius ($r_\perp$) along a particular line of sight, therefore obtaining the mass $M(< r_\perp)$ along a column bounded by $r_\perp$ requires additional assumptions about how that mass is distributed along the column. Commonly used assumptions include spherical symmetry and isothermality. The main challenges facing weak lensing mass estimates are in obtaining a wide enough field of view to normalize the shear field, and the possibility of superpositions of additional mass along the line of sight (Cen 1997 [23]; Floor & Evrard 2004 [48]; Hoekstra 2003 [76]).

1.3.4.3 The Sunyaev Zeldovich Effect

The cosmic microwave background (CMB) is an isotropic radiation bath that permeates the entire universe. It was created only a few hundred thousand years after the big bang, at the time that photons and matter last significantly interacted. Since then the radiation has cooled and is observed today as a 2.7 K blackbody spectrum.

Shortly after the CMB was discovered, Weymann (1965) [118] determined how Compton scattering from hot intergalactic gas would affect the spectrum of the CMB by slightly shifting some of its photons to higher energies. Sunyaev and Zeldovich (1970) [110] later predicted that the hot ICM in clusters would in fact produce such distortions. The effect is now known as the Sunyaev-Zeldovich (SZ) effect.

The ultimate shape of the distorted spectrum depends upon the product of the amount of energy that a scattered photon gains and the probability that a photon on its way through the cluster will Compton scatter:

$$y = \int \frac{kT}{m_e c^2} n_e \sigma_T dl \tag{1.17}$$

where σ_T is the Thompson cross section and the integral is calculated over the line of sight through the cluster. In practice, because current SZ instruments generally have poor angular resolution, what is actually measured is an integrated version of this parameter:

$$Y = \int y \; dA \propto \int n_e T \; dV \tag{1.18}$$

This Y parameter measures the thermal energy of the electrons in the cluster, which is akin to the gas mass times its temperature. If we know the relationship of gas mass to total mass, then Y can be used as a measure of cluster mass. The main drawback of this technique is once again confusion due to projection effects. This is especially disquieting in light of the fact that the magnitude of SZ distortions does not diminish with distance, however this redshift independence also makes the technique a valuable probe of the distant universe.

1.3.4.4 Optical Richness

Optical richness is in essence a measurement of the galaxy excess in the direction of a cluster above a certain magnitude limit and within a specific aperture. The particular optical richness parameter that is used in this work, $\mathrm{B_{gc}}$, is defined as the amplitude of the galaxy-cluster correlation function (Longair & Seldner 1979 [84]):

$$\xi(r) = \left(\frac{r}{r_0}\right)^{-\gamma} = \mathrm{B}_{gc}\; r^{-\gamma} \tag{1.19}$$

Galaxies are observed as projections on the sky, therefore what is measured is the angular two-point correlation function of galaxies, $\omega(\theta)$, where θ is the angle on the sky.

$\omega(\theta)$ is approximated by a powerlaw of the form:

$$\omega(\theta) = A_{\rm gg}\theta^{1-\gamma} \tag{1.20}$$

(Davis & Peebles 1983 [25]; Yee & Lopez-Cruz 1999 [124]), where $A_{\rm gg}$ is the galaxy-galaxy angular correlation amplitude. ω_θ is taken as the the distribution of galaxies around the the center of the cluster, and the amplitude is then relabeled as $A_{\rm gc}$. This amplitude can be measured from an image by counting the background-corrected excess of galaxies within a certain θ to a particular magnitude limit.

$\rm B_{gc}$ is then calculated through a deprojection analysis which assumes spherical symmetry (Longair & Seldner 1979 [84]):

$$\rm B_{gc} = N_{bg}\frac{D^{\gamma-3}A_{gc}}{I_\gamma \Phi[M(m_0, z)]} \tag{1.21}$$

where N_{bg} represents the background galaxy counts to apparent magnitude m_0, $D = (c/H_0)q_0z + (q_0 - 1)[(2q_0z + 1)^{1/2} - 1]/q_0^2(1 + z)^2$ is the angular diameter distance to the cluster redshift z, I_γ is an integration constant, and $\Phi[M(m_0, z)]$ is the integrated luminosity function of galaxies to the absolute magnitude M which corresponds to m_0 at z.

The evolution of galaxies in clusters is highly uncertain at $z > 0.5$, therefore a modified optical richness parameter is used. $\rm B_{gc,red}$ (Gladders & Yee 2005 [63]) is effectively a red-sequence $\rm B_{gc}$, calculated solely from galaxies that lie in the red-sequence of a particular cluster, within a 500 h_{50}^{-1} kpc radius aperture. The underlying motivation for constructing a red-sequence $\rm B_{gc}$ is that the red galaxies in clusters evolve much more slowly than the blue (star forming) galaxies, therefore $\rm B_{gc,red}$ should be a more reliable parameter.

Optical richness can be related to the total optical luminosity of the cluster through the luminosity function of galaxies (Equation 1.2). If light traces mass in clusters, the optical luminosity of a cluster becomes an indicator of its mass, therefore optical richness should in theory provide an efficient way to estimate the masses of clusters. One of the goals of this work is to characterize optical richness as an estimator of cluster properties and attempt to calibrate it for the RCS survey.

1.3.5 Scaling Relationships

Under assumptions that the ICM is in both thermal and hydrostatic equilibrium, relationships between its large scale properties can be obtained using simple theoretical arguments. For example, in the case of cluster mass and temperature

$$E \sim kT \text{ and } \mathrm{E} \sim \frac{\mathrm{GM}}{\mathrm{r}} \text{ and } \mathrm{M} \propto \mathrm{r}^3 \tag{1.22}$$

leads to

$$M \sim T^{3/2} \tag{1.23}$$

similarly, given that the X-ray emission of clusters is largely produced from thermal bremsstrahlung (i.e. $L \sim \rho_g M T^{1/2}$), luminosity and temperature should be related as

$$L \sim T^2 \tag{1.24}$$

At low redshift, most studies have found M and T to scale nearly as expected, however L and T have not proven quite as cooperative. The slope of the L-T relationship at low redshift has been repeatedly measured at values which are closer to 3 than 2 (e.g. Arnaud and Evrard 1999 [9]; Ettori et al. 2002 [44]). This is generally attributed to non-gravitational processes in the cluster, such as galaxy formation, raising the entropy of the gaseous material (Voit 2004 [116]). The redshift evolution of scaling relationships is also a subject of much recent interest (Ettori 2004 [46]), however the data at higher redshifts tends to have lower signal to noise and is thus often poorly constrained. Initial findings provide indications that there is some negative evolution in the L-T relationship, with lower luminosities being observed at a given temperature for higher redshift clusters (Ettori 2004 [46]).

1.4 Current Work

"As no better (wo)man advances to take this matter in hand, I hereupon offer my own poor endeavors. I promise nothing complete; because any human thing supposed to be complete, must for that very reason infallibly be faulty."

–Melville, 1851 [90]

1.4.1 The Chandra X-ray Observatory

All of the data that has been reduced and analyzed for this thesis comes from clusters that have been observed with the Chandra X-ray Observatory (CXO). Chandra, NASA's third Great Observatory, was launched from the space shuttle on July 23, 1999 and though the lifetime of the instrument was expected to be ~ 5 years, it has taken data ever since. Figure 1.2 shows a schematic of the telescope.

The mirrors on Chandra are made up of four nested pairs of grazing incidence mirrors (called the High Resolution Mirror Assembly, HRMA). Grazing incidence mirrors are required because the reflectivity at normal incidence of most materials is very low at X-ray energies. Chandra has two primary operating modes, one for high resolution imaging and the other for detailed spectroscopic studies. In the spectroscopic mode, transmission gratings are inserted in front of the CCDs, one specifically for high energy photons (the High Energy Transmission Grating, HETG) and the other for low energy photons (LETG). Chandra's imaging mode also provides spectroscopic information and is the configuration that has been used for the observations in this study.

X-rays are focused by the mirror onto a CCD array located at the focal plane of the telescope. The array used by the observations analyzed in this thesis is the Advanced CCD Imaging Spectrometer (ACIS). This array is made up of ten CCDs placed into two

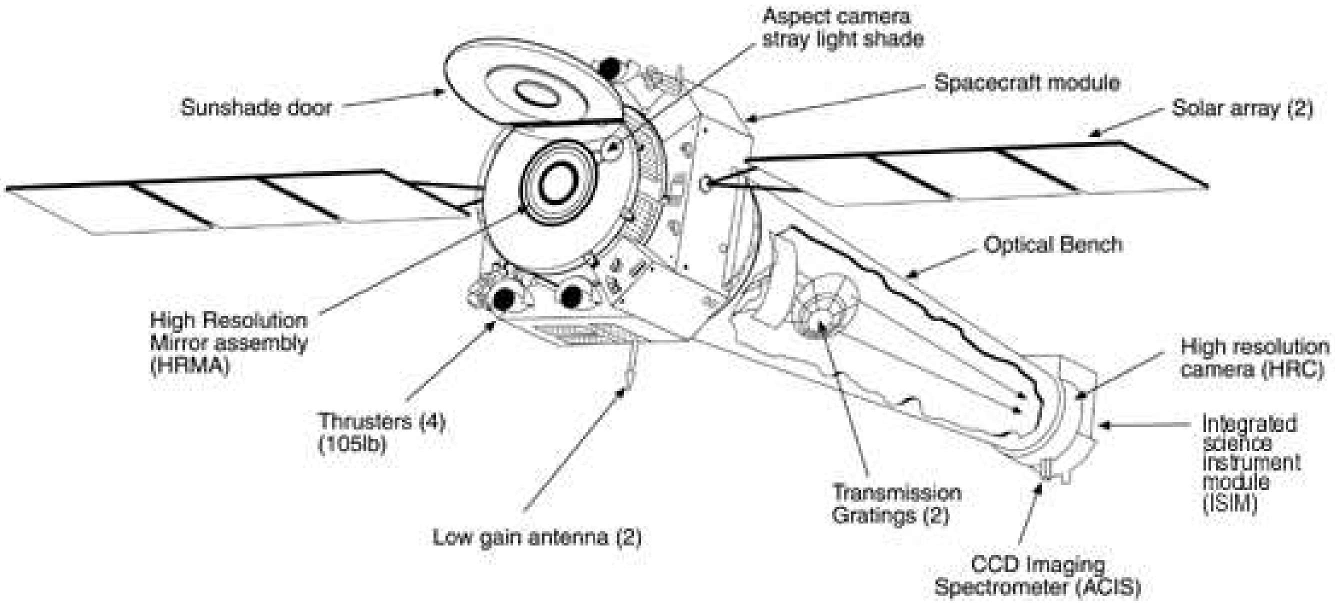

Figure 1.2 This is a schematic of the Chandra spacecraft. The size of the craft is 13.8 m $\times$ 19.5 m and it weighs 4,800 kg.

configurations, ACIS-I and ACIS-S, ostensibly for imaging and spectroscopy, however ACIS-S can be used in either mode. One of Chandra's most impressive accomplishments is its $\sim 0.5''$ spatial resolution, which results from the combination of Chandra's mirrors and the ACIS CCDs. The CCDs are $8' \times 8'$ in size and contain 1024×1024 pixels. Figure 1.3 indicates the layout of the ACIS CCDs.

The data analysis package that is commonly used in reducing and analyzing Chandra data is called the Chandra Interactive Analysis of Observations (CIAO) software package. It provides a wide array of tools that can be used to manipulate data produced by the telescope. Frequently used tools include DMCOPY (which allows files to be written from data which is filtered by spatial regions and/or energy ranges), and ACISSPEC (which creates a spectrum and its associated instrument response files).

1.4.2 Objectives

The main objectives of this thesis are threefold. The first goal is to compare independent mass estimates of clusters of galaxies. The second is to examine correlations between optical richness and cluster properties, and our third objective is to characterize the properties of high redshift optically selected clusters. Throughout this thesis we adopt a ΛCDM cosmology with $H_0 = 70$ km s^{-1} Mpc^{-1}, $\Omega_m = 0.3$, and Λ_0=0.7

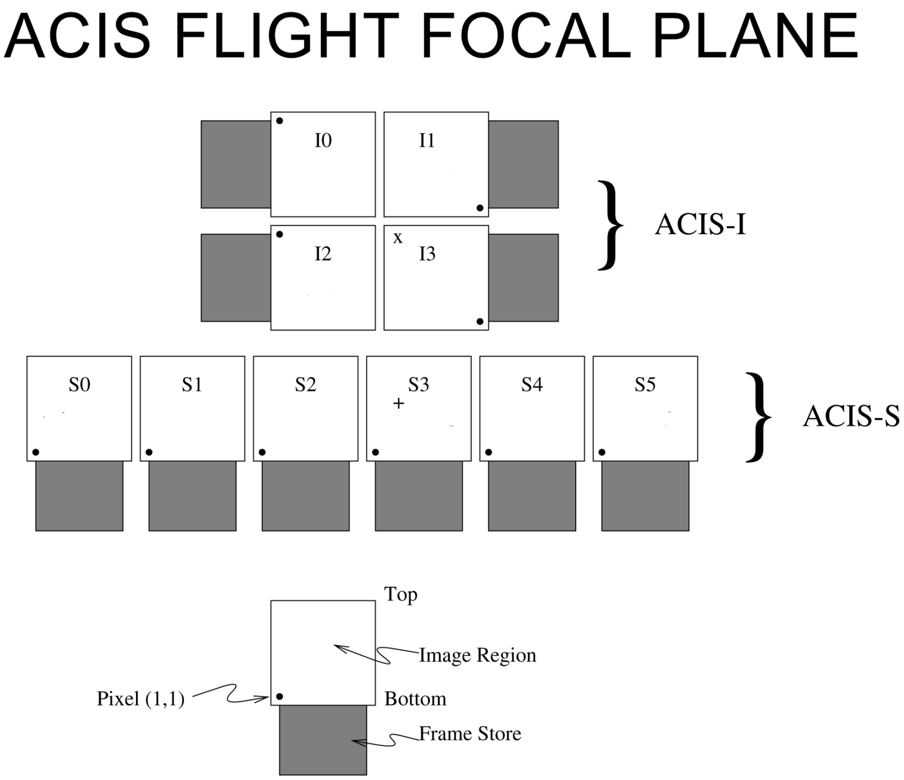

Figure 1.3 This is a schematic of the ACIS CCD array. ACIS-I was designed primarily for high resolution imaging, while ACIS-S is the array over which Chandra's transmission gratings disperse photons in a broad X like pattern centered at the aimpoint on the S-3 chip.

Chapter 2

X-ray Selected Clusters at Moderate Redshift: the CNOC Sample

2.1 Introduction

Clusters of galaxies are valuable cosmological probes. As the largest gravitationally bound objects in the universe, they play a key role in the tracing and modeling of large scale structure formation and evolution (e.g. Voit 2004 [116]). Because of our rapidly expanding sample of known clusters, finding efficient means of estimating cluster properties is a highly desirable goal.

The contribution of cluster studies to the field of observational cosmology hinges on our ability to accurately estimate cluster masses. In particular, through the determination of both gas mass and total mass, cluster analysis can lead to estimations of the cosmological mass density, Ω_m. On a more contemporary note, accurate measurement of the evolution of the cluster mass function provides constraints on the dark energy equation of state, w, which is complimentary to alternate methods (e.g. Levine, Schultz & White 2002 [82]). In addition, gaining an understanding of the evolution of X-ray scaling relationships (such as L-T and M-T) with redshift provides an important contribution to our ability to accurately model the evolution of large-scale structure in the universe (Voit 2004 [116]).

Intermediate redshift ($0.2 < z < 0.6$) clusters are well situated for the study of cluster properties. They are compact enough to be observed in a single Chandra field of view and they are present in statistically significant numbers. Intermediate redshift clusters are also luminous enough to permit detailed investigation, with the potential for placing strong contraints on cluster evolution.

Three frequently applied approaches to estimating cluster masses are gravitational lens modeling, optical measurements of velocity dispersion, and characterizing X-ray emission as a means of tracing the underlying potential well of the cluster. Each of these methods uses different observations and assumptions, which can be tested through their direct comparison. An alternate optical approach to the efficient estimation of cluster masses involves the use of optical richness. This method relies on the assumption that light is a reliable tracer of total cluster mass, and requires calibration via other methods.

Lensing mass estimates test both the assumption of hydrostatic equilibrium and our knowledge of the mass distribution in clusters. Because they probe all of the projected mass along the line of sight, which may include additional mass concentrations, they are susceptible to overestimation of cluster mass (Cen 1997 [23]; Floor & Evrard 2004 [48]; Hoekstra 2003 [76]). Dynamical mass estimates work under the assumption that velocity dispersion is directly related to the underlying gravitational potential of the cluster. Pitfalls of this technique also include the danger of overestimating the cluster mass in cases where substructure or mergers drive up velocity dispersions measurements (Bird 1994 [15]).

The hot, diffuse intracluster medium (ICM), which is observed in the X-ray, should be a direct tracer of a cluster's underlying potential well. Under assumptions of isothermality and hydrostatic equilibrium, the surface brightness of a cluster of galaxies can provide information on gas density as well as total gravitating mass. Factors that may influence the accuracy of X-ray mass estimates are temperature gradients, substructure, and mergers, which can compromise the previously stated assumptions.

One of the main objectives of this work is to, through direct comparison, identify any systematic biases in these methods with the ultimate goal of determining a robust calibration between optical richness and cluster mass. An accurate calibration of the relationship between mass and optical richness would allow us to determine the masses of large samples of clusters in a highly efficient manner, providing strong constraints on the evolution of the cluster mass function and, consequently, key cosmological parameters.

In this paper we present a detailed analysis of high resolution Chandra X-ray observations of 14 CNOC (Yee, Ellingson & Carlberg 1996 [126]) clusters at z $\sim$ 0.3. Our analysis probes the temperature, enrichment, morphology, and surface brightness of the hot ICM present in each cluster. From this initial analysis, we examine the X-ray scaling laws of our sample, and derive mass estimates which are then compared to dynamical and weak lensing mass estimates. Finally, we use our results to calibrate relationships between red-sequence optical richness ($\mathrm{B_{gc,red}}$) and global cluster X-ray properties (T_X, $\mathrm{R_{200}}$, L_X and $\mathrm{M_{200}}$).

2.2 Cluster Sample & Observations

The data in our sample were retrieved from the Chandra Data Archive (CDA) after conducting a search for currently available Chandra observations of the Canadian Network for Observational Cosmology (CNOC) [126] intermediate redshift ($0.1709 < z < 0.5466$) subsample of 15 EMSS clusters (Gioia et al. 1990 [57]; Henry et al. 1992 [72]) and one Abell cluster (Abell 1958 [1]). The selection criterion for this sample can be found in Yee, Ellingson & Carlberg 1996 [126].

Chandra Advanced CCD Imaging Spectrometer (ACIS) observations of 14 of the 16 CNOC clusters were obtained. Six of these clusters were observed with the ACIS-S CCD array, and eight were observed with ACIS-I, with an overall range in individual exposures of $11.7 - 91.9$ kiloseconds. Three of the clusters in our sample were observed on multiple occasions, in which case we have chosen the longest of those observations to include in our analysis. Each of the observations analyzed in this study possesses a start date which falls on or after 24 April, 2000, indicating a focal plane temperature of -120^o C for the entire sample.

Aspect solutions were examined for irregularities and none were found. Background contamination due to charged particle flares were reduced by removing time intervals during which the background rate exceeded the average background rate by more than 20%. The event files were filtered on standard grades and bad pixels were removed. A two-dimensional elliptical Lorentzian was fit to the counts image of each dataset to locate the center of the X-ray emission peak. In the case of the heavily substructured cluster MS0451+02, there is no obvious central peak, so a position at the center of the extended emission was chosen for spectral analysis at an RA, Dec of 04:54:09.941,+02:55:14.52 (J2000), and the surface brightness profile was centered on a slightly offset peak of emission at an RA, Dec of 04:54:07.249, +02:54:27.31 (J2000).

Table 2.1 provides a list of each of the clusters in our sample, including redshifts, obsid, array, and corrected exposure information for each observation.

2.3 Data Reduction

After initial cleaning of the data (Section 2.2), 0.6-7.0 keV images, instrument maps, and exposure maps were created using the CIAO tools DMCOPY, MKINSTMAP and MKEXPMAP. Data with energies below 0.6 keV and above 7.0 keV were excluded due to uncertainties in the ACIS calibration and background contamination, respectively.

Flux images were created by dividing the resulting images by their respective exposure maps. Point source detection was performed by running the tools WTRANSFORM and WRECON on the flux images. Adaptively smoothed flux images were created with CSMOOTH. Figure 2.1 contains CFHT images obtained from the CNOC database [126], and, where available, HST images obtained from the MAST archive, each of which is overlayed with X-ray contours created from smoothed Chandra flux images.

Table 2.1. Cluster Sample

Cluster	z	$1''$ $[h_{70}^{-1}$ kpc]	obsid	Array	Chandra Exposure[a] [seconds]
Abell 2390	0.2279	3.65	4193	ACIS-S	89624
MS 0015.9+1609	0.5466	6.39	520	ACIS-I	69235
MS 0302.7+1658	0.4246	5.57	525	ACIS-I	11764
MS 0440.5+0204	0.1965	3.17	4196	ACIS-S	45104
MS 0451.5+0250	0.2010	3.31	4215	ACIS-I	66275
MS 0451.6-0305	0.5392	6.34	902	ACIS-S	43652
MS 0839.8+2938	0.1928	3.21	2224	ACIS-S	31383
MS 0906.5+1110	0.1709	2.91	924	ACIS-I	31392
MS 1006.0+1202	0.2605	4.03	925	ACIS-I	25590
MS 1008.1-1224	0.3062	4.52	926	ACIS-I	37376
MS 1358.4+6245	0.3290	4.74	516	ACIS-S	53055
MS 1455.0+2232	0.2570	3.99	4192	ACIS-I	91886
MS 1512.4+3647	0.3726	5.14	800	ACIS-S	14665
MS 1621.5+2640	0.4274	5.59	546	ACIS-I	30062

[a]Corrected exposure time (see text for corrections applied).

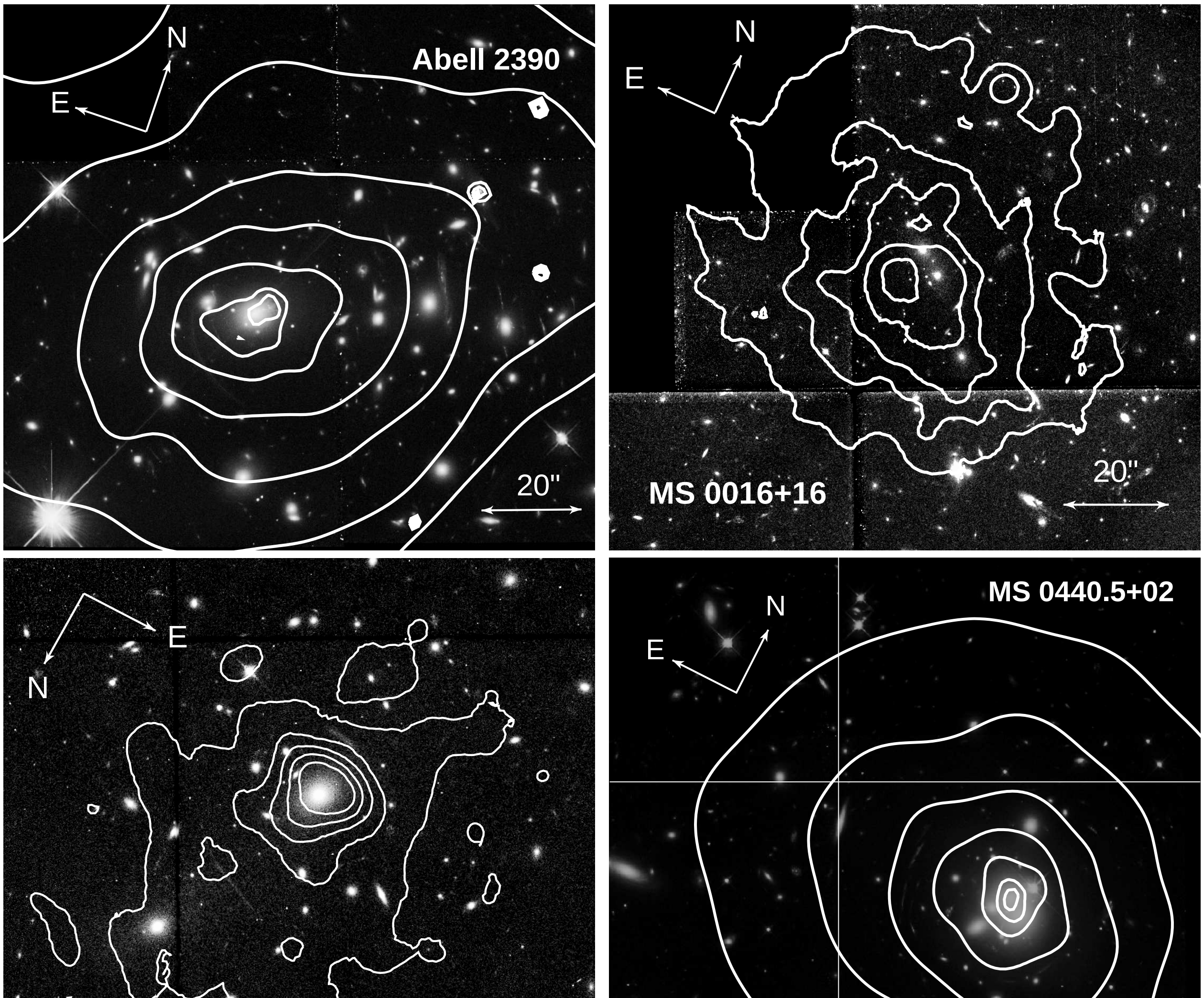
Abell 2390
N
E
20"
MS 0016+16
N
E
20"
MS 0302+16
E
N
20"
MS 0440.5+02
N
E
20"
MS 0451+02
N
E
20"
MS 0451-03
N
E
20"

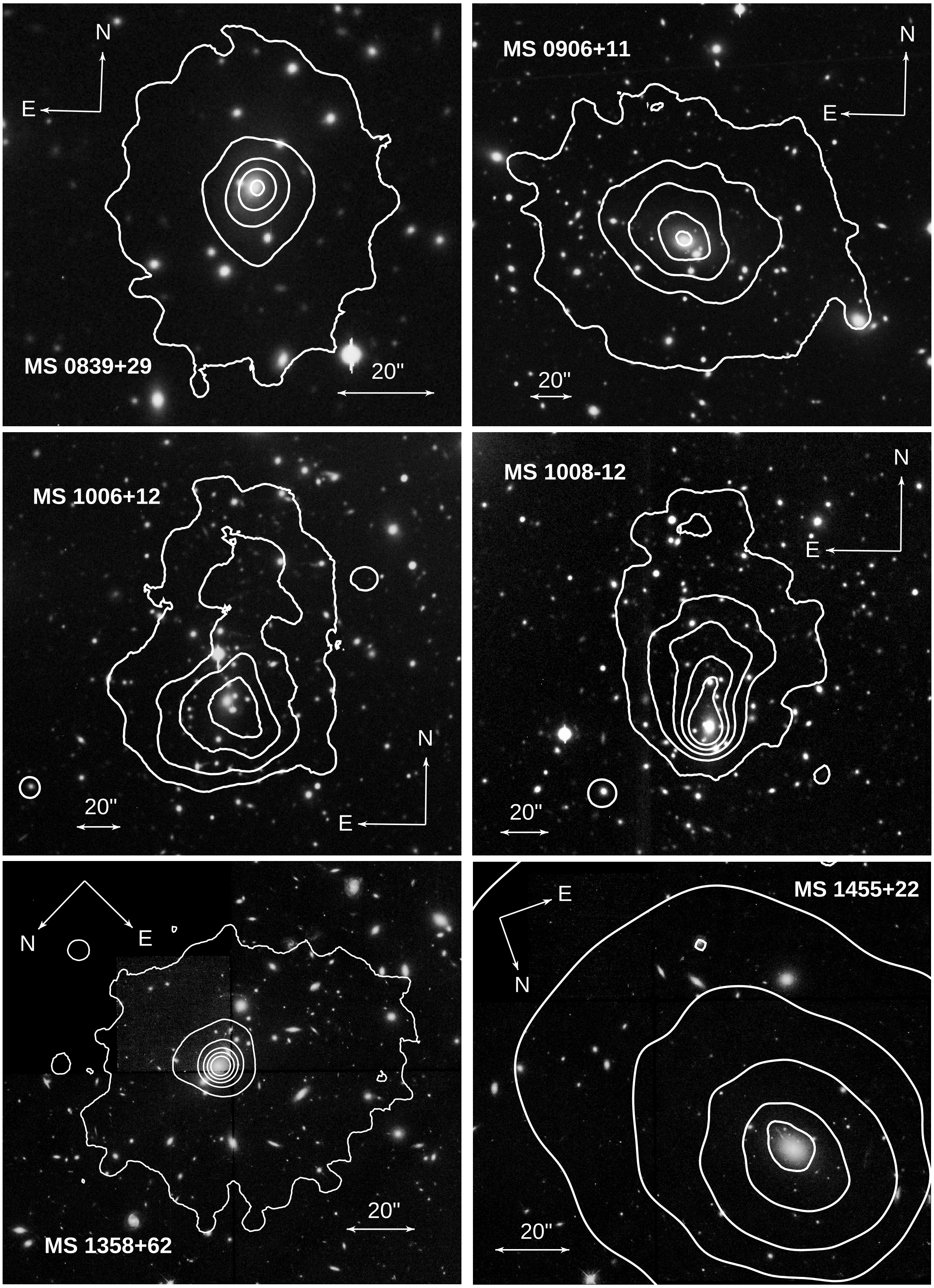
MS 0839+29
MS 0906+11
MS 1006+12
MS 1008-12
MS 1358+62
MS 1455+22
N
E
20''

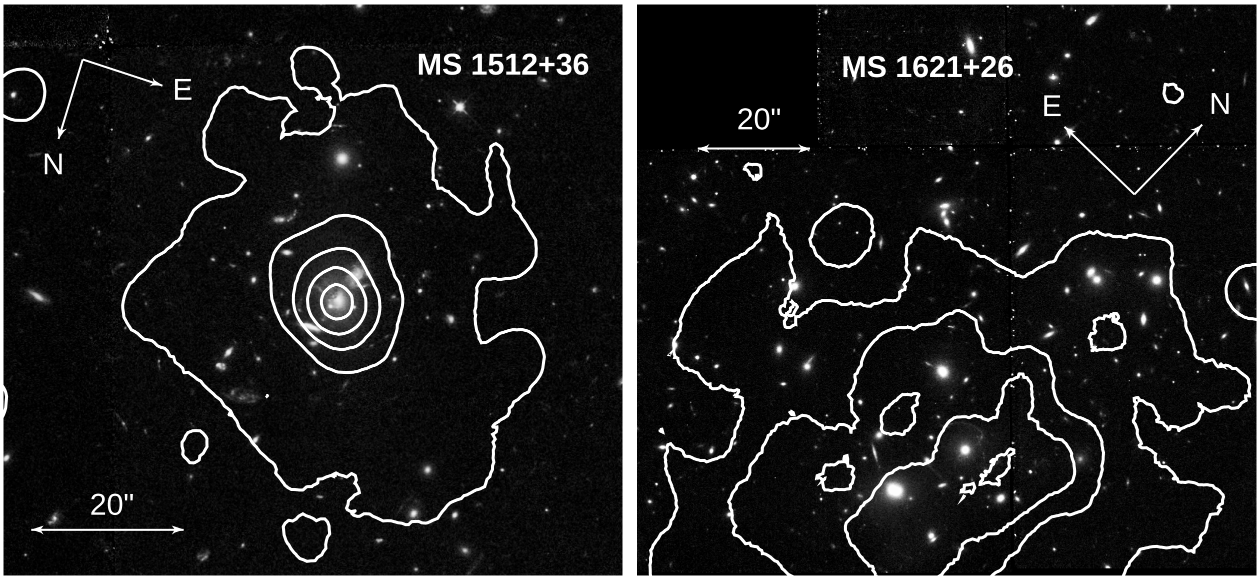

Figure 2.1 X-ray contours are overlaid on optical images of clusters in our sample. HST images of Abell 2390, MS0016+16, MS0302+16, MS0440.5+02, MS0451-03, MS1358+62, MS1455+22, MS1512+36, and MS1621+26 were retrieved from the MAST archive, with respective filters F814W, F555W, F814W, F702W, F702W, F814W, F606W, F555W, and F814W. Gunn r band (to $r \sim 24$) CFHT images were obtained for the remaining five clusters (MS0451+02, MS0839+29, MS0906+11, MS1006+12, and MS1008-12). X-ray countours were created from adaptively smoothed Chandra 0.6-7.0 keV flux images, and all have linear values except for three of the cooling core clusters (Abell 2390, MS0440+02, and MS1455+22) which are overlayed with logarithmic X-ray contours. Note the significant amount of substructure present in MS0451+02, MS1006+12, and MS1008-12.

2.4 Surface Brightness

A radial surface brightness profile was computed over the range 0.6-7.0 keV in circular annuli for each cluster. These profiles were then fit with both single and double β models. Single β models take the form

$$I(r) = I_B + I_0 \left(1 + \frac{r^2}{r_c^2}\right)^{-3\beta+\frac{1}{2}} \tag{2.1}$$

where I_B is a constant representing the surface brightness contribution of the background, I_0 is the normalization and r_c is the core radius.

The double β-model has the form

$$I(r) = I_B + I_1 \left(1 + \frac{r^2}{r_1^2}\right)^{-3\beta_1+\frac{1}{2}} + I_2 \left(1 + \frac{r^2}{r_2^2}\right)^{-3\beta_2+\frac{1}{2}} \tag{2.2}$$

where each component has fit parameters (I_n, r_n, β_n).

Though a fair number of the clusters in our sample posess detectably elliptical or irregular emission, circular surface brightness profiles were chosen based on a number of factors. First, as discussed in Neumann & Bohringer (1997) [97] and Bohringer et al. (1998) [16], differences in masses derived using elliptical vs. circular β profiles are small ($\sim 5\%$). Secondly, circular β profiles provide a more straightforward comparison between dynamical and X-ray derived masses, since dynamical mass calculations assume sphericity. Finally, temperature uncertainties should outweigh any errors introduced by assuming radial symmetry.

The parameters of the best fitting single β model of each cluster are shown in table 2.2. While nine of the clusters' surface brightness profiles do not exhibit excess unmodeled emission in their cores when fit with a single β model, five of the clusters do exhibit excess emission in their cores. The surface brightness profiles of these clusters are better fit with the addition of a second β component. All of the clusters requiring a double β model are believed to contain cooling flows: Abell 2390, MS0440+02, MS0839+29, MS1358+62, and MS1455+22 (Lewis et al. 1999 [83]; Allen 2000 [2]) and exhibit strong ($L_{\mathrm{H}\alpha+[\mathrm{N_{II}}]} > 10^{42}$ erg s^{-1}) extended Hα emission (Donahue, Stocke & Gioia 1992 [32]; Lewis et al. 1999 [83]). Best fitting double β model parameters are given in Table 2.3. Surface brightness profiles of the clusters in our sample are shown in Figure 2.2. Discrepancies in background values are due to the use of both ACIS-I and ACIS-S arrays (ACIS-S typically has background values which are a factor of three higher than ACIS-I).

2.5 Spectral Analysis

2.5.1 Spatially Resolved Spectra

With the goal of elucidating the radial dependence of temperature for the clusters in our sample, spectra were extracted within circular annuli spanning the central $150 - 600$ h$_{70}^{-1}$ kpc of each cluster, depending on the signal-to-noise ratio of each observation. The extraction regions were sized to include at least 2500 counts per spectrum in the 0.6-7.0 keV band for each data set. This number was chosen as a minimum for achieving reasonable temperature constraints on the emission in each annulus.

Extractions were performed after the removal of previously detected point sources (Section 2.3), using the CIAO tool ACISSPEC, which incorporates the changing response over large areas of the detector. Three of the 14 clusters in this sample did not possess enough signal for more than one extraction region, and were removed from the sample during the subsequent spatial analysis. Spectra from the eleven remaining clusters were then grouped to contain 20 counts per bin, and were analyzed using XSPEC (Arnaud 1996 [8]). Single temperature spectral models with fixed galactic absorption and varying abundances were fitted to the data. The results of these fits were used to create a temperature profile for each cluster.

Figure 2.3 illustrates the eleven resulting temperature profiles. It is clear from

Table 2.2. β-Model Fits

Cluster	R_c $[h_{70}^{-1}\mathrm{kpc}]$	β	I_0[a]	I_B[a]	χ^2/DOF
Abell 2390	63^{+2}_{-2}	$0.531^{+0.003}_{-0.003}$	1575^{+34}_{-35}	$1.7^{+0.2}_{-0.2}$	368.8/145
MS 0015.9+1609	253^{+13}_{-13}	$0.72^{+0.02}_{-0.02}$	100^{+4}_{-4}	$1.17^{+0.04}_{-0.04}$	316.2/230
MS 0302.7+1658	27^{+5}_{-4}	$0.50^{+0.02}_{-0.02}$	337^{+67}_{-56}	$0.89^{+0.04}_{-0.04}$	328.2/324
MS 0440.5+0204	13^{+2}_{-1}	$0.444^{+0.006}_{-0.006}$	933^{+84}_{-93}	$2.4^{+0.1}_{-0.1}$	372.2/191
MS 0451.5+0250	520^{+50}_{-43}	$0.87^{+0.1}_{-0.08}$	51^{+1}_{-1}	$1.7^{+0.3}_{-0.3}$	620.4/227
MS 0451.6-0305	200^{+10}_{-10}	$0.73^{+0.02}_{-0.02}$	154^{+6}_{-6}	$1.81^{+0.05}_{-0.05}$	257.3/205
MS 0839.8+2938	58^{+3}_{-3}	$0.62^{+0.02}_{-0.01}$	407^{+37}_{-27}	$2.33^{+0.07}_{-0.07}$	220.7/208
MS 0906.5+1110	96^{+7}_{-6}	$0.60^{+0.02}_{-0.02}$	185^{+8}_{-7}	$1.2^{+0.2}_{-0.2}$	177/174
MS 1006.0+1202	129^{+15}_{-13}	$0.55^{+0.03}_{-0.02}$	88^{+7}_{-6}	$0.8^{+0.2}_{-0.1}$	270.7/213
MS 1008.1-1224	113^{+9}_{-9}	$0.55^{+0.02}_{-0.02}$	101^{+7}_{-6}	$1.09^{+0.06}_{-0.06}$	329.4/218
MS 1358.4+6245	76^{+5}_{-5}	$0.54^{+0.01}_{-0.01}$	455^{+32}_{-30}	$3.8^{+0.1}_{-0.1}$	349.6/207
MS 1455.0+2232	$36.7^{+0.8}_{-0.8}$	$0.612^{+0.004}_{-0.004}$	3277^{+78}_{-73}	$2.29^{+0.06}_{-0.06}$	789.1/209
MS 1512.4+3647	22^{+3}_{-3}	$0.51^{+0.01}_{-0.01}$	86^{+14}_{-11}	$0.19^{+0.01}_{-0.01}$	192.5/191
MS 1621.5+2640	184^{+28}_{-25}	$0.56^{+0.05}_{-0.04}$	34^{+3}_{-3}	$1.38^{+0.09}_{-0.1}$	234/225

[a]Surface brightness I in units of 10^{-9} photons sec^{-1} cm^{-2} arcsec^{-2}

Table 2.3. Double β-Model Fits

Cluster	R_{c1} $[h_{70}^{-1}\mathrm{kpc}]$	β_1	I_{01} [a]	R_{c2} $[h_{70}^{-1}\mathrm{kpc}]$	β_2	I_{02} [a]	I_{B} [a]	χ^2/DOF
Abell 2390	20^{+4}_{-3}	$0.53^{+0.1}_{-0.07}$	1709^{+157}_{-176}	80^{+11}_{-7}	$0.52^{+0.02}_{-0.01}$	504.9^{+101}_{-84}	$1.7^{+0.2}_{-0.2}$	177.6/106
Abell 0440.5+0204	$11.7^{+1}_{-0.6}$	$1.0^{+0.2}_{-0.2}$	1246^{+149}_{-134}	33^{+2}_{-4}	$0.489^{+0.011}_{-0.007}$	338^{+30}_{-17}	$2.80^{+0.1}_{-0.09}$	221.5/191
MS 0839.8+2938	21^{+4}_{-4}	$0.9^{+0.2}_{-0.1}$	761^{+146}_{-105}	59^{+8}_{-7}	$0.62^{+0.02}_{-0.02}$	366^{+56}_{-61}	$2.3^{+0.1}_{-0.1}$	190/167
MS 1358.4+6245	10^{+2}_{-1}	$0.46^{+0.05}_{-0.02}$	3042^{+423}_{-380}	121^{+24}_{-20}	$0.63^{+0.1}_{-0.05}$	188^{+38}_{-31}	$4.0^{+0.3}_{-0.4}$	156/139
MS 1455.0+2232	36^{+8}_{-4}	$1.1^{+0.2}_{-0.2}$	2635^{+325}_{-383}	56^{+21}_{-18}	$0.64^{+0.01}_{-0.01}$	1306^{+261}_{-218}	$2.45^{+0.07}_{-0.07}$	276.3/183

[a] Surface brightness I in units of 10^{-9} photons sec^{-1} cm^{-2} arcsec^{-2}

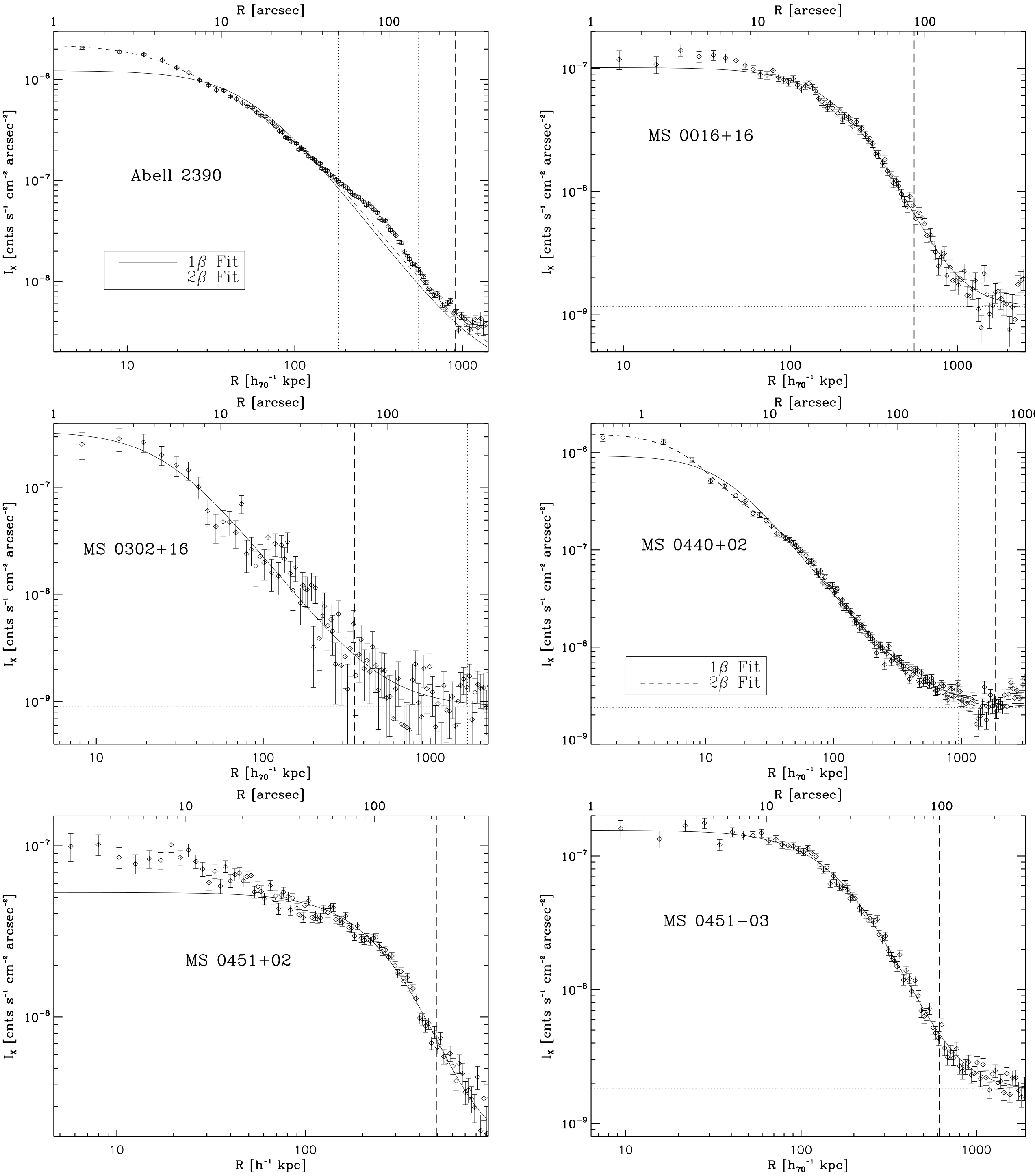
R [arcsec]
I_X [cnts s^{-1} cm^{-2} arcsec^{-2}]
R [h_{70}^{-1} kpc]
R [h^{-1} kpc]
Abell 2390
MS 0016+16
MS 0302+16
MS 0440+02
MS 0451+02
MS 0451−03
1β Fit
2β Fit

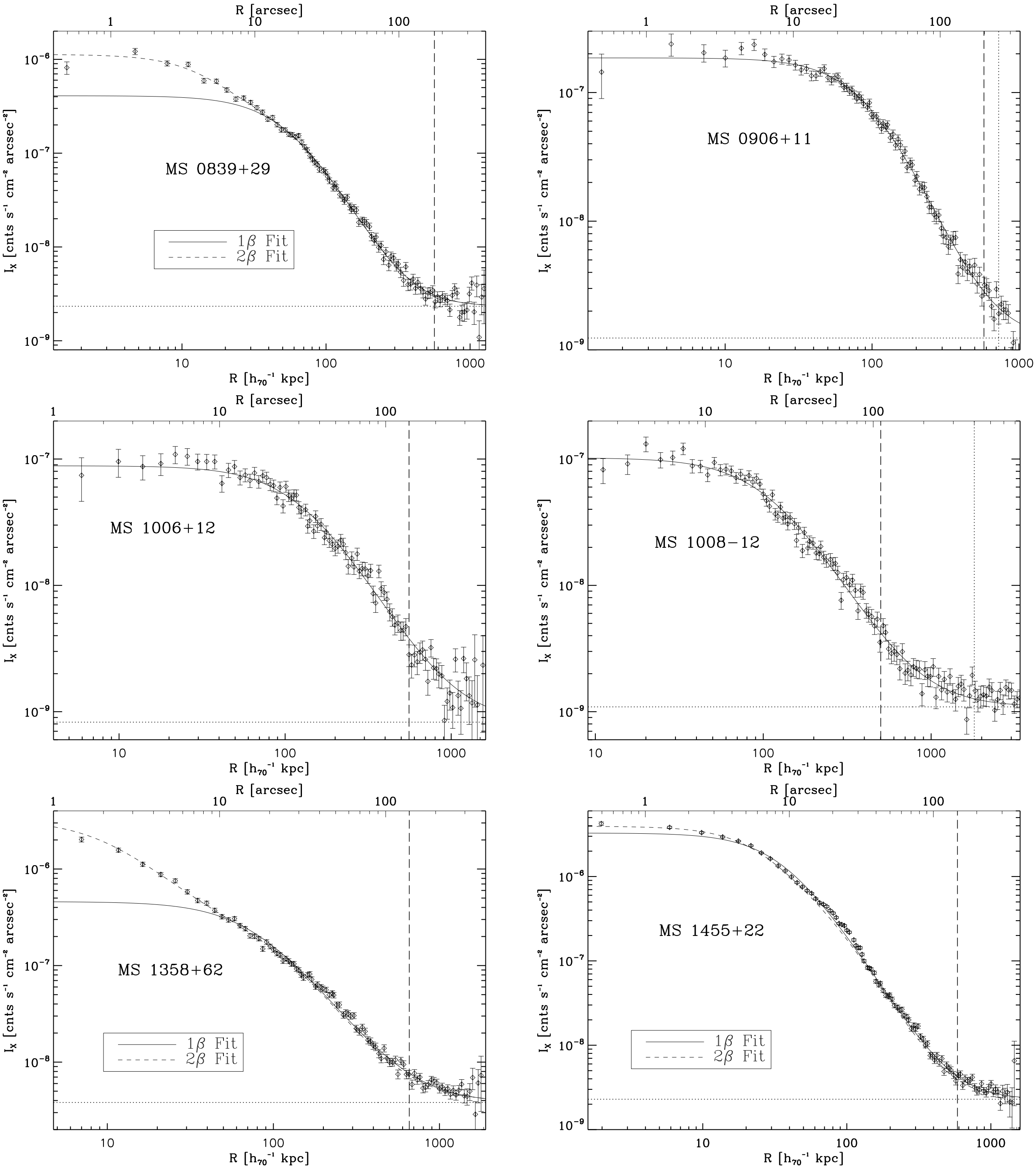
R [arcsec]
I_X [cnts s^{-1} cm^{-2} arcsec^{-2}]
R [h_{70}^{-1} kpc]
MS 0839+29
MS 0906+11
MS 1006+12
MS 1008−12
MS 1358+62
MS 1455+22
1β Fit
2β Fit

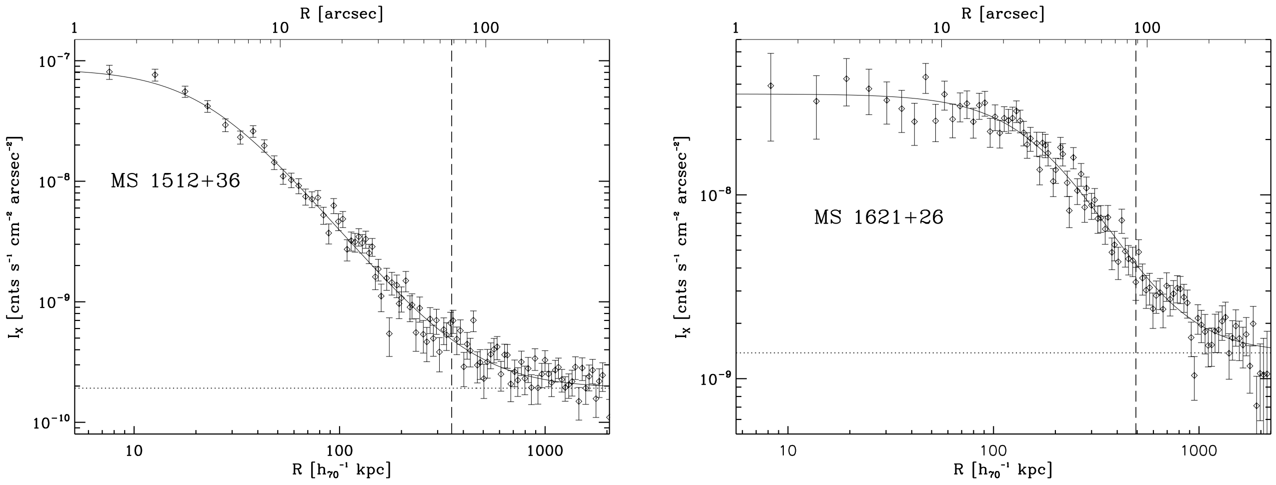

Figure 2.2 Radial surface brightnesses of CNOC clusters calculated in 1″ annular bins using 0.6-7.0 keV data. Horizontal dotted lines denote the best-fitting background of the model, and vertical dotted lines indicate regions of the profile which were excluded from fitting. Solid lines describe the best fitting single β model for each cluster, while short dashed lines indicate double β model fits to the data. Long dashed vertical lines represent R_{2500}. Most clusters are well-fit by either a single or double β model (reduced $\chi^2 < 1.8$), except in the case of MS0451+02, which exhibits a significant amount of substructure.

these figures that significant cooling cores are present in five of the clusters in this sample: Abell 2390, MS0440+02, MS0839+29, MS1358+62, and MS1455+22. These are the same five clusters which required double β model fits to their surface brightness profiles (Section 2.4). The remaining six temperature profiles are consistent with isothermality.

2.5.2 Integrated Spectral Fits and R_{2500}

Using the fitted X-ray centroid positions obtained in Section 2.2 (with the exception of MS0451+02, as noted in Section 2.2), a spectrum was extracted from each cleaned event file in a circular region with a 300 h_{70}^{-1} kpc radius. These spectra were then analyzed with XSPEC, using weighted response matrices (RMFs) and effective area files (ARFs) generated with the CIAO tool ACISSPEC and the latest version of the Chandra calibration database (CALDB 3.0.1). Circular background regions of 100 pixel radius were extracted from the aim point chip as far away from the aimpoint as possible. Each spectrum was grouped to contain at least 20 counts per bin.

Spectra were fitted with single temperature spectral models, inclusive of foreground absorption. Each spectrum was initially fit with the absorbing column frozen at its measured value (Dickey & Lockman 1990 [28]), and redshifts were fixed throughout the analysis. Metal abundances were allowed to vary. Data with energies below 0.6 keV and above 7.0 keV were again excluded.

A second fit was then performed, allowing the absorbing column to vary. No evidence for excess absorption was found in 13 of the 14 clusters. The MS0440+02 spectrum, however, was equally well fit by a model inclusive of excess foreground absorption.

The results of these fits, combined with the best fitting β model parameters from Section 2.4, were then used to estimate the value of R_{2500} for each cluster. This is accomplished by combining the equation for total gravitating mass

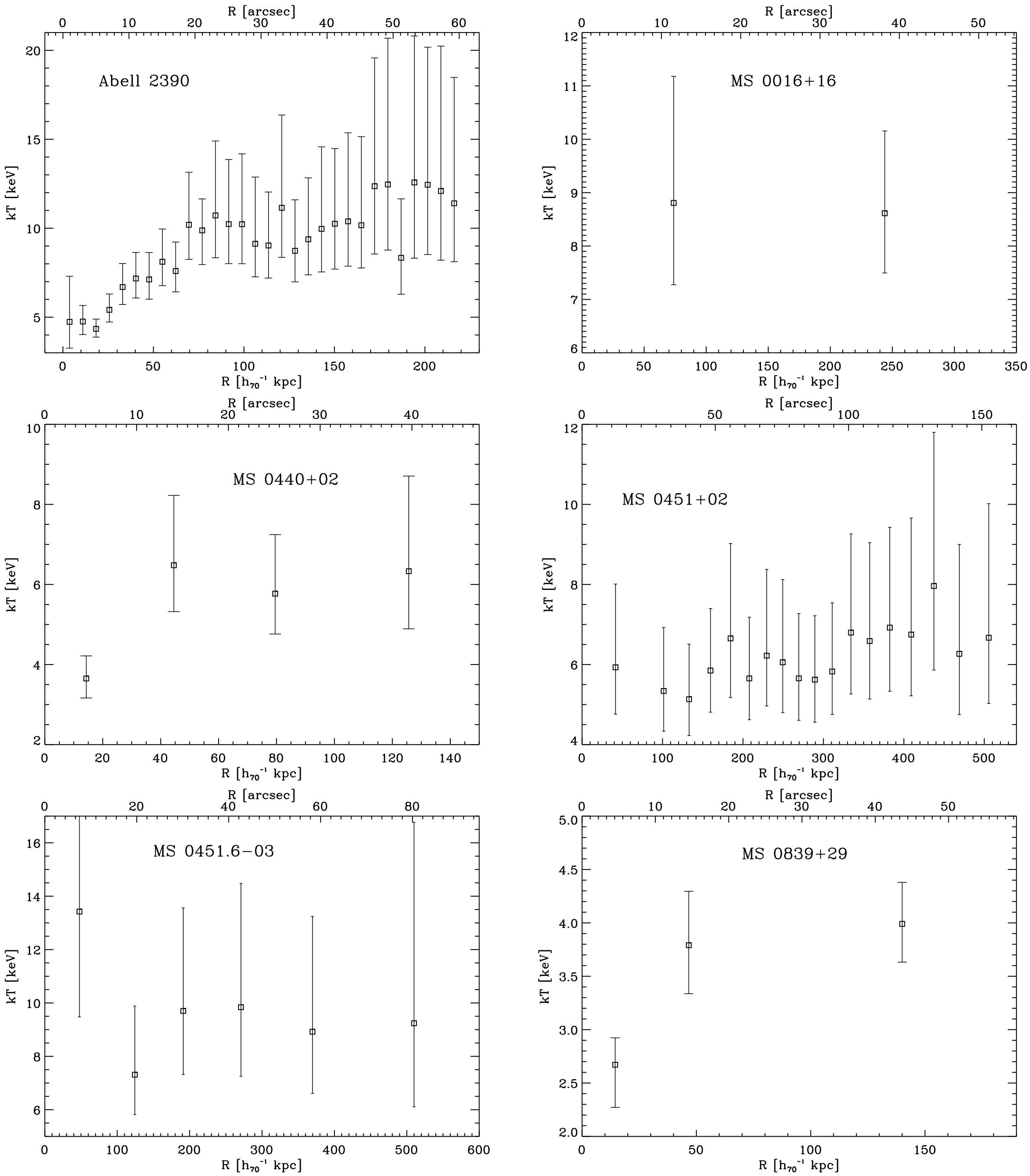
R [arcsec]
kT [keV]
R [h_{70}^{-1} kpc]
Abell 2390
MS 0016+16
MS 0440+02
MS 0451+02
MS 0451.6−03
MS 0839+29

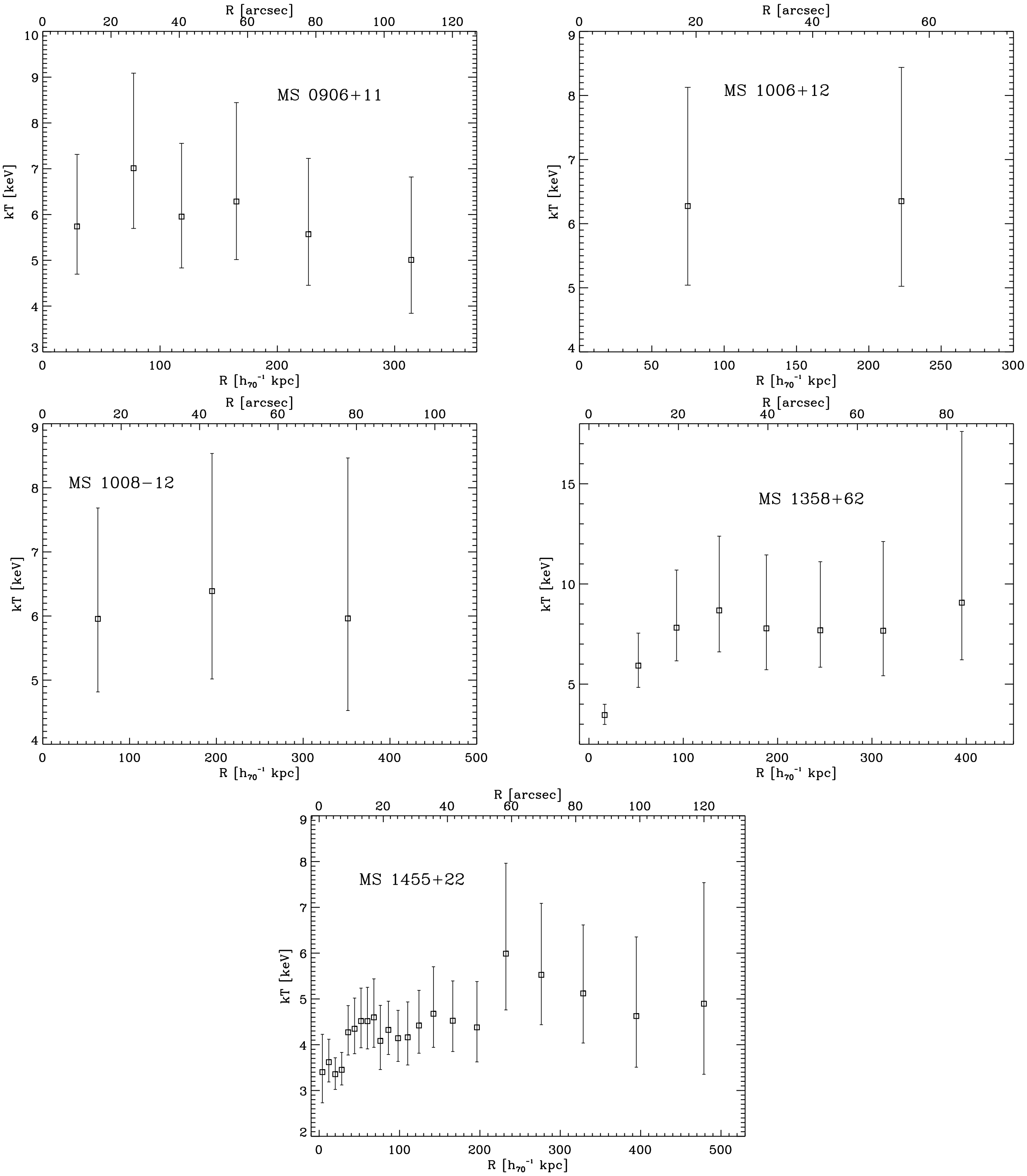

Figure 2.3 Radial temperature profiles determined by fitting, in XSPEC, single temperature spectral models to spectra extracted from circular annuli selected to include a minimum of 2500 counts in the 0.6-7.0 keV band. Error bars represent 90% confidence limits. Indications of cool cores are seen in Abell 2390, MS0440+02, MS0839+20, MS1358+62, and MS1455+22.

$$M_{tot}(r) = -\frac{T(r)r}{G\mu m_p}\left(\frac{\delta \ \ln \ \rho}{\delta \ \ln \ \mathrm{r}} + \frac{\delta \ \ln \ \mathrm{T}}{\delta \ \ln \ \mathrm{r}}\right) \tag{2.3}$$

(where μm_p is the mean mass per particle) with the definition of mass overdensity

$$M_{tot}(r_\Delta) = \frac{4}{3}\pi\rho_c(1+z)^3 r_\Delta^3 \Delta \tag{2.4}$$

where the critical density $\rho_c = 3H_0^2E_z^2/8\pi G$, z is the cluster redshift, Δ is the factor by which the density at r_Δ exceeds the critical density, and $E_z = H_z/H_0 = \left[\Omega_m(1+z)^3 + \Omega_\Lambda\right]^{1/2}$. These equations are then combined with the density profile implied from the β model (assuming hydrostatic equilibrium, spherical symmetry, and isothermality, Equation 1.4)

$$\rho_{gas}(r) = \rho_0\left(1 + \frac{r^2}{r_c^2}\right)^{-3\beta/2} \tag{2.5}$$

resulting in the equation

$$\frac{r_\Delta}{r_c} = \sqrt{\left[\frac{3\beta T}{G\mu m_p(4/3)\pi\rho_c(1+z)^3 r_c^2\Delta}\right] - 1} \tag{2.6}$$

(Ettori 2000 [43]; Ettori et al. 2004 [46]).

After the initial estimation of R_{2500}, additional spectra were extracted from within that radius, and spectral fitting was performed again. This iterative process was continued until fitted temperatures and calculated values of R_{2500} were consistent with extraction radii. The results of this process, including values of R_{2500}, temperatures and abundances are shown in Table 2.4, along with 90% confidence ranges.

An additional process was carried out for the five cooling core clusters in our sample. Using previously determined temperature profiles (Section 2.5.1), the radius within which cooling became prominent in each cluster was estimated. A single annular spectrum was then extracted for each cluster from that radius to R_{2500} and fitted with single temperature spectral models. The observation of MS0440+02 did not possess

Table 2.4. Single Temperature Spectral Fits for R < R_{2500}

Cluster	R_{2500} [h_{70}^{-1} kpc]	kT [keV]	N_H [10^{20} cm^{-2}]	Z [solar]	χ^2/DOF
Abell 2390	701^{+25}_{-19}	$10.3^{+0.6}_{-0.5}$	6.8	$0.4^{+0.1}_{-0.1}$	401.8/434
MS 0015.9+1609	550^{+38}_{-35}	$9.2^{+1.0}_{-0.9}$	4.07	$0.3^{+0.1}_{-0.1}$	185.5/271
MS 0302.7+1658	352^{+139}_{-72}	4^{+3}_{-1}	10.9	$0.1^{+1}_{-0.1}$	10.3/26
MS 0440.5+0204	640^{+120}_{-68}	8^{+2}_{-1}	9.67	$0.8^{+0.6}_{-0.5}$	272.2/378
	583^{+95}_{-66}	7^{+2}_{-2}	12^{+3}_{-3}	$0.8^{+0.5}_{-0.4}$	267.7/377
MS 0451.5+0250	496^{+90}_{-74}	$6.1^{+0.7}_{-0.6}$	7.8	$0.4^{+0.1}_{-0.1}$	443.9/420
MS 0451.6-0305	614^{+48}_{-38}	10.2^{+1}_{-1}	5.07	$0.4^{+0.1}_{-0.1}$	223/258
MS 0839.8+2938	491^{+24}_{-22}	$4.0^{+0.3}_{-0.3}$	4.11	$0.6^{+0.2}_{-0.2}$	241.7/283
MS 0906.5+1110	582^{+44}_{-34}	$5.6^{+0.8}_{-0.6}$	3.54	$0.2^{+0.2}_{-0.2}$	134.2/319
MS 1006.0+1202	557^{+67}_{-45}	7^{+1}_{-1}	3.76	$0.3^{+0.2}_{-0.2}$	100/199
MS 1008.1-1224	501^{+41}_{-32}	$5.9^{+0.9}_{-0.7}$	6.98	$0.2^{+0.2}_{-0.2}$	159.5/203
MS 1358.4+6245	575^{+72}_{-44}	$8.0^{+1.1}_{-0.9}$	1.93	$0.5^{+0.2}_{-0.2}$	272.2/332
MS 1455.0+2232	496^{+7}_{-7}	$4.4^{+0.1}_{-0.1}$	3.13	$0.38^{+0.05}_{-0.05}$	569.6/385
MS 1512.4+3647	351^{+42}_{-32}	$3.4^{+0.8}_{-0.7}$	1.38	$0.6^{+0.5}_{-0.4}$	43.2/74
MS 1621.5+2640	493^{+109}_{-68}	7^{+3}_{-2}	3.57	$0.4^{+0.4}_{-0.4}$	56.3/116

Table 2.5. Cooling Core Corrected Single Temperature Spectral Fits for R < R_{2500}

Cluster	R_{cutoff} [h_{70}^{-1} kpc]	R_{2500} [h_{70}^{-1} kpc]	kT [keV]	N_H [10^{20} cm^{-2}]	Z [solar]	χ^2 [reduced]
Abell 2390	66	761^{+35}_{-30}	$12.1^{+1}_{-0.9}$	6.8	$0.3^{+0.3}_{-0.3}$	355/434
MS 0839.8+2938	109	565^{+72}_{-55}	5^{+1}_{-1}	4.11	$0.6^{+0.5}_{-0.4}$	195.5/237
MS 1358.4+6245	154	658^{+93}_{-59}	9^{+2}_{-1}	1.93	$0.4^{+0.3}_{-0.3}$	209/253
MS 1455.0+2232	68	518^{+17}_{-12}	$4.8^{+0.3}_{-0.2}$	3.13	$0.37^{+0.08}_{-0.08}$	394.2/370

enough signal to constrain a fit to the cooling flow excised spectrum, therefore it was discarded. The results of these fits are shown in Table 2.5, along with inner extraction radii and calculated values of R_{2500}.

Overall, our integrated temperatures are comparable to previous ROSAT results (see Lewis et al. 1999 [83]), though they are better constrained through Chandra observations. More recent analyses of subsets of these clusters have been conducted by Mohr et al. 2000 [92], Matsumoto et al. 2000 [89], Allen et al. 2001 [4], Arabadjis et al. 2002 [7], Donahue et al. 2003 [29], Ettori & Lombardi 2003 [45], Ettori 2004 [46], and Henry 2004 [70]. Our fitted temperatures are consistent within errors of the vast majority of the values reported in these papers. Noticeable discrepancies arise occasionally in the case of cooling flow clusters (where some of these authors have not excised the cooling flow contribution to integrated temperature) and MS1008-1224, for which we consistently derive a lower temperature than other studies. Metallicities for this sample are consistent with an overall value of ~ 0.3 solar, as is seen in lower redshift clusters. This suggests that ICM enrichment occurs early in a cluster's history, evidence which is corroborated by the work of Mushotzky and Loewenstein 1997 [94].

2.6 Mass Determinations

Using the results of the spectral fits and β model fits, along with Equations 2.3, 2.5, and 2.6, gas masses and total masses were calculated out to R_{200} for the clusters in our sample. Central densities were determined via an expression relating the observable cluster X-ray luminosity to gas density, using emission measures obtained during spectral fitting in XSPEC.

For the nine non-cooling core clusters, single temperature spectra fits and single β model parameters were used. For the five clusters which exhibit significant cooling, spectral parameters from cooling core excised spectral fits were used, and β and r_c were taken from the results of double β model fits.

To determine the effects of inner temperature gradients on total cluster mass, least-squares fitting was performed on the temperature profiles obtained in Section 2.5.1 for the five cooling core clusters. The resulting parameterizations were included in Equation 2.3, and masses were calculated out to the edge of the cooling region (Table 2.5). Masses were also calculated without the inclusion of this parameterization, and the results compared. According to the outcome of this exercise, the inclusion of temperature gradients in mass calculations of the five cooling core clusters in our sample would result in, at most, a 0.3% correction to the total mass within the cooling region. This correction is negligible compared to the other uncertainties in mass calculations and is therefore not included in the final results, which are presented in Table 2.6 along with 68% confidence intervals.

Gas mass fractions, f_{gas}, can be used to calculate the cosmological mass density, Ω_m, via the relation

$$\Omega_m = \frac{\Omega_b}{f_{gas}\ (1 + 0.19h^{0.5})} \tag{2.7}$$

(Allen et al. 2002 [5]), where $0.19h^{0.5}$ represents the baryonic contribution from optically luminous matter (White et al. 1993 [120]; Fukugita et al. 1998 [54]). A value of $\Omega_b\ h^{-2}$ of 0.0205 ± 0.0018 is adopted (O'Meara et al. 2001 [98]), and here we take $h = 0.7$. Using a weighted average of $f_{gas} = 0.080 \pm 0.003 h_{70}^{-1}$ for our sample, we calculate a cosmological

Table 2.6. Mass Estimates for R < R_{200}

Cluster	R_{200}[a] $[h_{70}^{-1}$ Mpc$]$	n_0 $[10^{-1}$ cm$^{-3}]$	M_{gas} $[10^{14}$ h_{70}^{-1} $M_\odot]$	M_{tot} $[10^{14}$ h_{70}^{-1} $M_\odot]$	f_{gas} $[h_{70}^{-1}]$
Abell 2390	$2.7^{+0.1}_{-0.1}$	$0.165^{+0.004}_{-0.004}$	$2.9^{+0.2}_{-0.2}$	21^{+1}_{-1}	$0.14^{+0.03}_{-0.03}$
MS 0015.9+1609	$2.1^{+0.1}_{-0.1}$	$0.0498^{+0.001}_{-0.0004}$	$1.36^{+0.05}_{-0.05}$	17^{+1}_{-1}	$0.079^{+0.009}_{-0.1}$
MS 0302.7+1658	$1.2^{+0.5}_{-0.3}$	$0.271^{+0.008}_{-0.008}$	$0.33^{+0.04}_{-0.04}$	3^{+1}_{-1}	$0.10^{+0.05}_{-0.05}$
MS 0440.5+0204	$2.1^{+0.3}_{-0.2}$	$0.214^{+0.003}_{-0.003}$	$0.87^{+0.05}_{-0.05}$	9^{+2}_{-2}	$0.09^{+0.02}_{-0.02}$
MS 0451.5+0250	$2.5^{+0.2}_{-0.1}$	$0.0259^{+0.0003}_{-0.0003}$	$2.1^{+0.1}_{-0.1}$	$15.9^{+0.8}_{-0.8}$	$0.13^{+0.03}_{-0.03}$
MS 0451.6-0305	$2.3^{+0.2}_{-0.1}$	$0.0694^{+0.0005}_{-0.0005}$	$1.22^{+0.05}_{-0.05}$	21^{+2}_{-2}	$0.058^{+0.007}_{-0.008}$
MS 0839.8+2938	$2.0^{+0.3}_{-0.2}$	$0.184^{+0.004}_{-0.004}$	$0.56^{+0.05}_{-0.05}$	8^{+1}_{-1}	$0.07^{+0.02}_{-0.02}$
MS 0906.5+1110	$2.1^{+0.2}_{-0.1}$	$0.0972^{+0.0009}_{-0.001}$	$0.83^{+0.04}_{-0.04}$	$8.6^{+0.7}_{-0.7}$	$0.10^{+0.02}_{-0.02}$
MS 1006.0+1202	$2.0^{+0.2}_{-0.2}$	$0.0558^{+0.0008}_{-0.0009}$	$1.11^{+0.08}_{-0.08}$	9^{+1}_{-1}	$0.12^{+0.03}_{-0.03}$
MS 1008.1-1224	$1.8^{+0.1}_{-0.1}$	$0.0670^{+0.0008}_{-0.0008}$	$0.90^{+0.05}_{-0.05}$	$7.2^{+0.6}_{-0.6}$	$0.13^{+0.02}_{-0.02}$
MS 1358.4+6245	$2.4^{+0.3}_{-0.2}$	$0.091^{+0.003}_{-0.003}$	$1.1^{+0.2}_{-0.2}$	17^{+2}_{-2}	$0.05^{+0.03}_{-0.02}$
MS 1455.0+2232	$1.84^{+0.06}_{-0.04}$	$0.360^{+0.009}_{-0.01}$	$0.76^{+0.07}_{-0.07}$	$6.9^{+0.3}_{-0.3}$	$0.11^{+0.03}_{-0.03}$
MS 1512.4+3647	$1.3^{+0.1}_{-0.1}$	$0.143^{+0.003}_{-0.003}$	$0.13^{+0.01}_{-0.01}$	$2.7^{+0.3}_{-0.4}$	$0.05^{+0.01}_{-0.01}$
MS 1621.5+2640	$1.8^{+0.4}_{-0.2}$	$0.0304^{+0.0006}_{-0.0006}$	$0.86^{+0.08}_{-0.08}$	10^{+2}_{-2}	$0.09^{+0.03}_{-0.03}$

[a]90% confidence intervals

mass density of $\Omega_m = 0.32 \pm 0.03$ (68% confidence). This value is consistent with the currently accepted value of $\Omega_m \sim 0.3$ (Bahcall et al. 1999 [12]; Voit 2004 [116]).

2.7 Mass Comparisons

2.7.1 Dynamical Mass Comparisons

Dynamical masses can be calculated from velocity dispersions via the Jeans equation

$$M(r) = \frac{-\sigma_r^2 r}{G}\left(\frac{\delta \text{ ln } \sigma_\mathrm{r}^2}{\delta \text{ ln r}} + \frac{\delta \text{ ln } \nu(\mathrm{r})}{\delta \text{ ln r}} + 2\beta\right) \tag{2.8}$$

where σ_r represents the radial velocity dispersion, $\nu(r)$ is the galaxy number density profile, and β represents the anisotropy of the system. According to Van der Marel et al. (2000) [27], the CNOC clusters can be treated as isotropic (i.e. $\beta = 0$), and $\nu(r)$ takes the form

$$\nu(r) = \rho_0 (r/a)^{-\gamma} \left[1 + r/a\right]^{\gamma - 3} \tag{2.9}$$

where the best fitting values of a and γ for isotropicity are 0.224 and 0.75, respectively. This relationship was obtained by creating a composite CNOC cluster via dimensionless scaling (Van der Marel et al. (2000) [27]), as was a plot of σ vs. r. This figure (Van der Marel et al. (2000) [27], Figure 2) indicates that σ is not a strong function of radius out to R_{200}, and in keeping with both Lewis et al. (1999) [83] and Carlberg et al. (1996) [20] we assume that $\sigma(r) = \sigma$.

Using Equation 2.8, dynamical masses were calculated for our sample out to R_{200} (as determined by X-ray parameters in Section 2.5.2), using the velocity dispersions of Borgani et al. (1999) [18]. These masses were then compared to X-ray derived masses from the previous section (Section 2.6). A weighted average gives an overall dynamical to X-ray mass ratio of 0.96 ± 0.06. Table 2.7 lists both dynamical and X-ray derived masses along with their ratio and 68% confidence intervals. Figure 2.4 is a plot indicating the dynamical to X-ray mass ratio of each cluster in the sample. A histogram of the log of these ratios with a fitted gaussian (mean ratio 1.0) is plotted in Figure 2.5.

2.7.2 Weak Lensing Mass Comparisons

Weak lensing mass estimates were obtained for seven of the clusters in our sample using deep optical observations at the CFHT 3.6m telescope (Hoekstra 2005, private communication). The model-independent projected mass estimates that we cite in this paper were calculated for the inner 500 h^{-1} kpc of each cluster, using a cosmology of $H_0 = 100$, $\Omega_m = 0.3$ and $\Omega_\Lambda = 0.7$.

To compare X-ray derived masses to weak lensing masses, we calculated a mass within 500 h^{-1} kpc, using the adopted cosmology of Hoekstra and projecting our masses in a cylindrical region out to 10 Mpc from the cluster core. A comparison of weak lensing masses to X-ray derived masses can be found in Table 2.8, a plot of mass ratios is given in Figure 2.6, and a histogram of the log of these ratios with a fitted gaussian (mean ratio 1.2) is plotted in Figure 2.7. A weighted average gives a weak lensing to X-ray mass ratio of 1.10 ± 0.09, which is expected given that weak lensing mass estimates are prone to the overestimation of cluster mass due to projection effects along the line of sight (Cen 1997 [23]; Floor & Evrard 2004 [50]; Hoekstra 2003 [76]).

2.8 X-ray Scaling Laws

2.8.1 The $L_X - T_X$ Relationship

Unabsorbed bolometric X-ray luminosities within R_{2500} were obtained for our sample in the following manner. Unabsorbed X-ray luminosities for the 2-10 keV band were calculated in XSPEC during spectral fitting (Section 2.5.2). In the case of the five clusters which exhibit significant cooling, corrected, integrated luminosities were ob-

Table 2.7. Dynamical Mass Comparisons for R < R_{200}

Cluster	Dynamical Mass $[10^{14}\ h_{70}^{-1}\ M_\odot]$	X-ray Mass $[10^{14}\ h_{70}^{-1}\ M_\odot]$	Ratio [Dynamical/X-ray]
Abell 2390	26^{+4}_{-3}	21^{+1}_{-1}	$1.2^{+0.2}_{-0.1}$
MS 0015.9+1609	16^{+5}_{-3}	17^{+1}_{-1}	$0.9^{+0.3}_{-0.2}$
MS 0302.7+1658	$3.8^{+1}_{-0.6}$	3^{+1}_{-1}	$1.1^{+0.5}_{-0.4}$
MS 0440.5+0204	6^{+2}_{-1}	9^{+2}_{-2}	$0.7^{+0.3}_{-0.2}$
MS 0451.5+0250	15^{+2}_{-2}	$15.9^{+0.8}_{-0.8}$	$1.0^{+0.1}_{-0.1}$
MS 0451.6-0305	24^{+4}_{-3}	21^{+2}_{-2}	$1.2^{+0.2}_{-0.2}$
MS 0839.8+2938	12^{+3}_{-3}	8^{+1}_{-1}	$1.4^{+0.5}_{-0.4}$
MS 0906.5+1110	8^{+2}_{-1}	$8.6^{+0.7}_{-0.7}$	$0.9^{+0.2}_{-0.2}$
MS 1006.0+1202	13^{+4}_{-3}	9^{+1}_{-1}	$1.3^{+0.5}_{-0.3}$
MS 1008.1-1224	12^{+3}_{-2}	$7.2^{+0.6}_{-0.6}$	$1.6^{+0.4}_{-0.3}$
MS 1358.4+6245	14^{+2}_{-1}	17^{+2}_{-2}	$0.8^{+0.1}_{-0.1}$
MS 1455.0+2232	12^{+3}_{-2}	$6.9^{+0.3}_{-0.3}$	$1.7^{+0.4}_{-0.3}$
MS 1512.4+3647	$2.6^{+1}_{-0.8}$	$2.7^{+0.3}_{-0.4}$	$0.9^{+0.5}_{-0.3}$
MS 1621.5+2640	8^{+1}_{-1}	10^{+2}_{-2}	$0.8^{+0.2}_{-0.2}$

Table 2.8. Weak Lensing Mass Comparisons for R < 500 h^{-1} kpc

Cluster	Weak Lensing Mass $[10^{14}\ h^{-1}\ M_\odot]$	X-ray Mass $[10^{14}\ h^{-1}\ M_\odot]$	Ratio [Lensing/X-ray]
Abell 2390	$5.1^{+0.6}_{-0.6}$	$5.3^{+0.5}_{-0.4}$	$1.0^{+0.1}_{-0.1}$
MS 0015.9+1609	8^{+1}_{-1}	$5.2^{+0.4}_{-0.4}$	$1.6^{+0.3}_{-0.3}$
MS 0906.5+1110	$3.3^{+0.9}_{-0.9}$	$2.8^{+0.2}_{-0.2}$	$1.2^{+0.3}_{-0.3}$
MS 1358.4+6245	$4.2^{+0.9}_{-0.9}$	$4.9^{+0.6}_{-0.6}$	$0.9^{+0.2}_{-0.2}$
MS 1455.0+2232	$3.4^{+0.6}_{-0.6}$	$2.6^{+0.1}_{-0.1}$	$1.3^{+0.2}_{-0.2}$
MS 1512.4+3647	$1.6^{+0.7}_{-0.7}$	$1.4^{+0.2}_{-0.2}$	$1.1^{+0.5}_{-0.5}$
MS 1621.5+2640	$5.9^{+0.8}_{-0.8}$	$3.6^{+0.7}_{-0.7}$	$1.6^{+0.4}_{-0.4}$

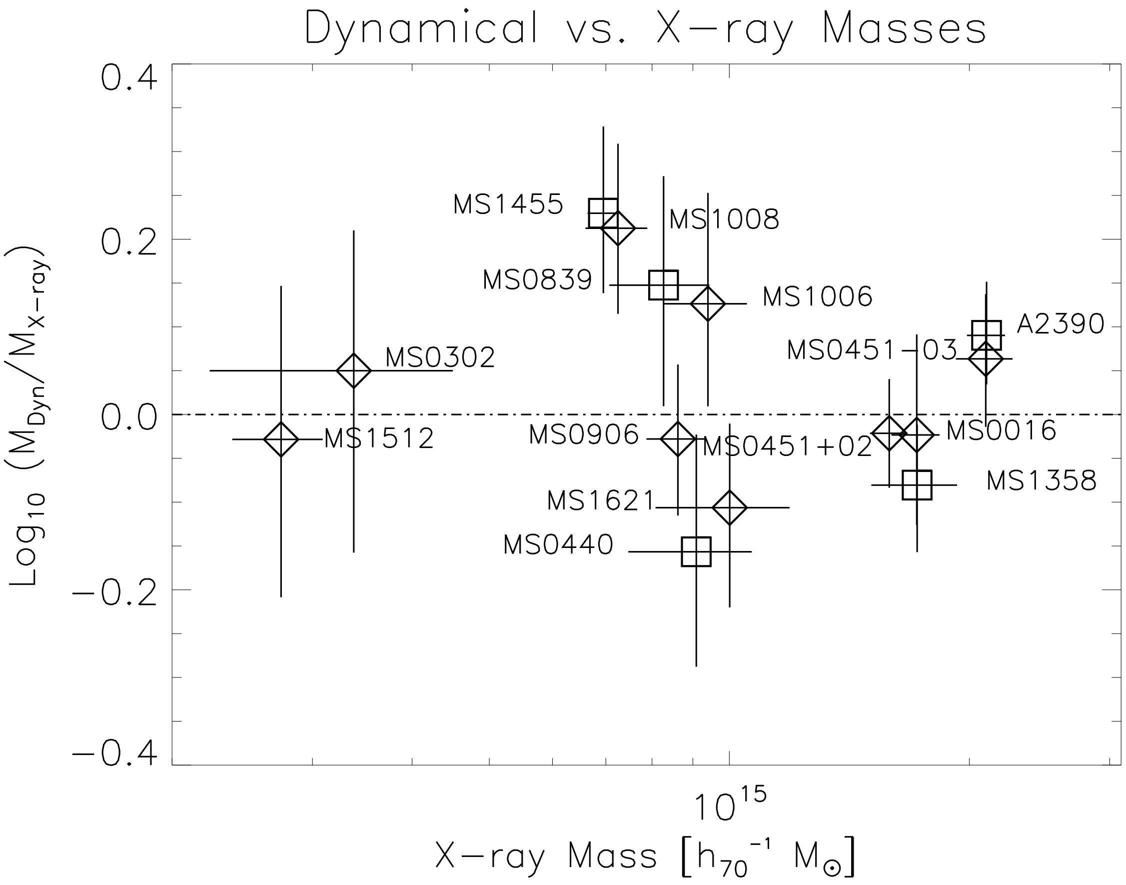

Figure 2.4 X-ray mass estimates are plotted against the log of M_{Dyn}/M_{X-ray}. The dot-dash line at zero represents a mass ratio of 1.0, and 0.3 in either direction represents a factor of two mass discrepancy. Squares indicate cooling core clusters. Error bars denote 68% confidence limits.

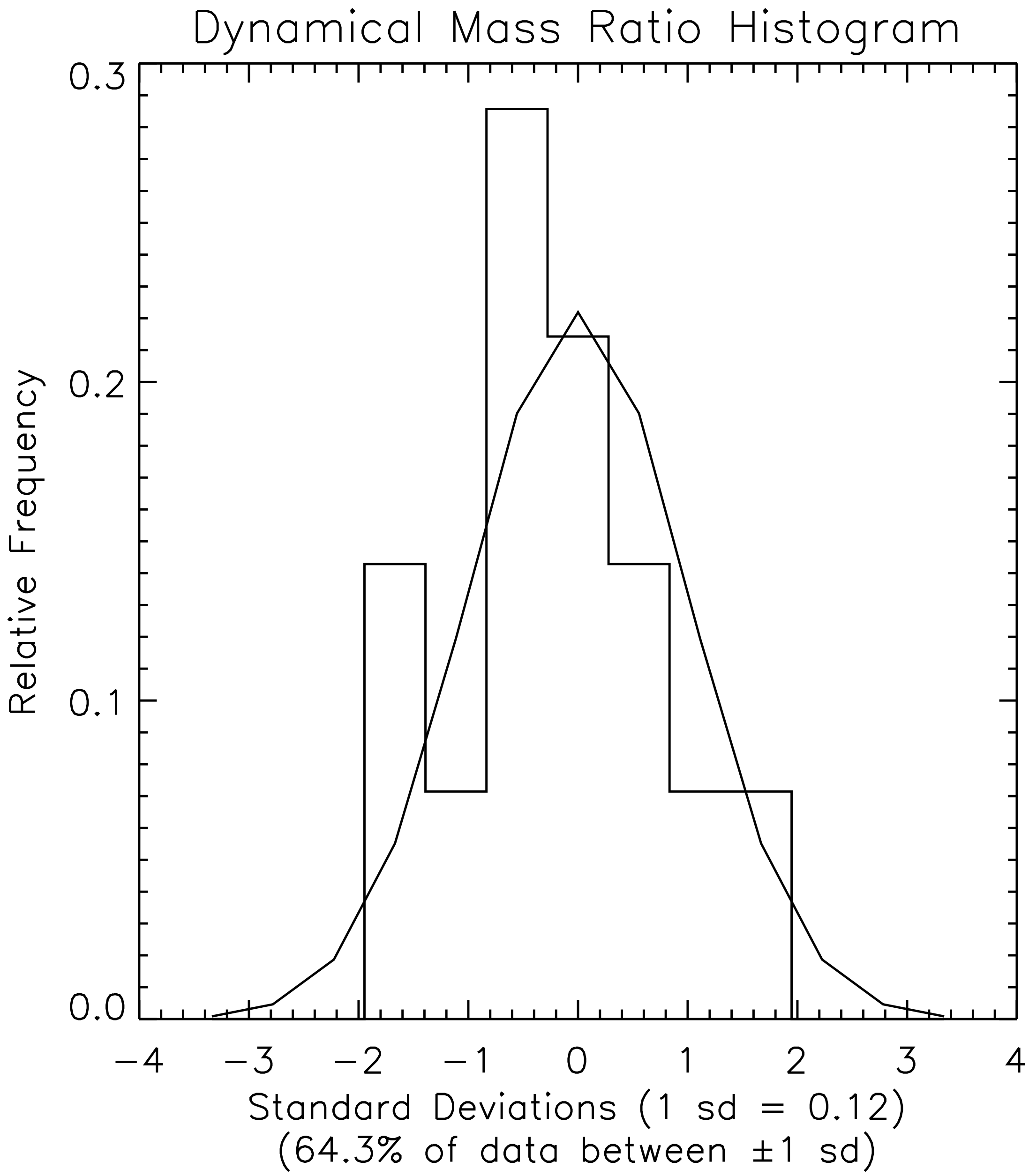

Figure 2.5 Relative frequency histogram of the log of dynamical/X-ray mass ratios with a normal curve overlaid. X-axis units are in standard deviations. One standard deviation represents a change in ratio of 0.32, with zero indicating a mean ratio of 1.0.

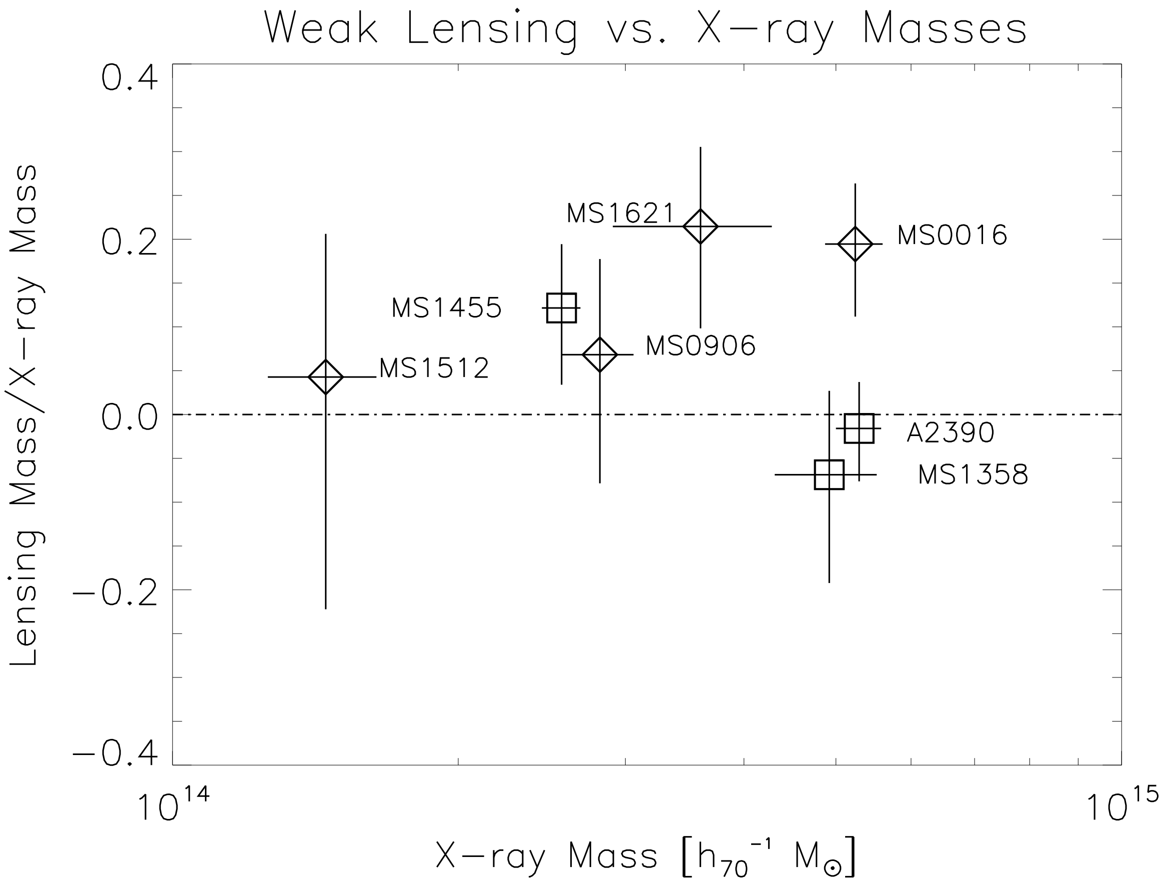

Figure 2.6 X-ray mass estimates are plotted against the log of M_{Lens}/M_{X-ray}. The dot-dash line at zero represents a mass ratio of 1.0, and 0.3 in either direction represents a factor of two mass discrepancy. Squares indicate cooling core clusters, and error bars denote 68% confidence limits.

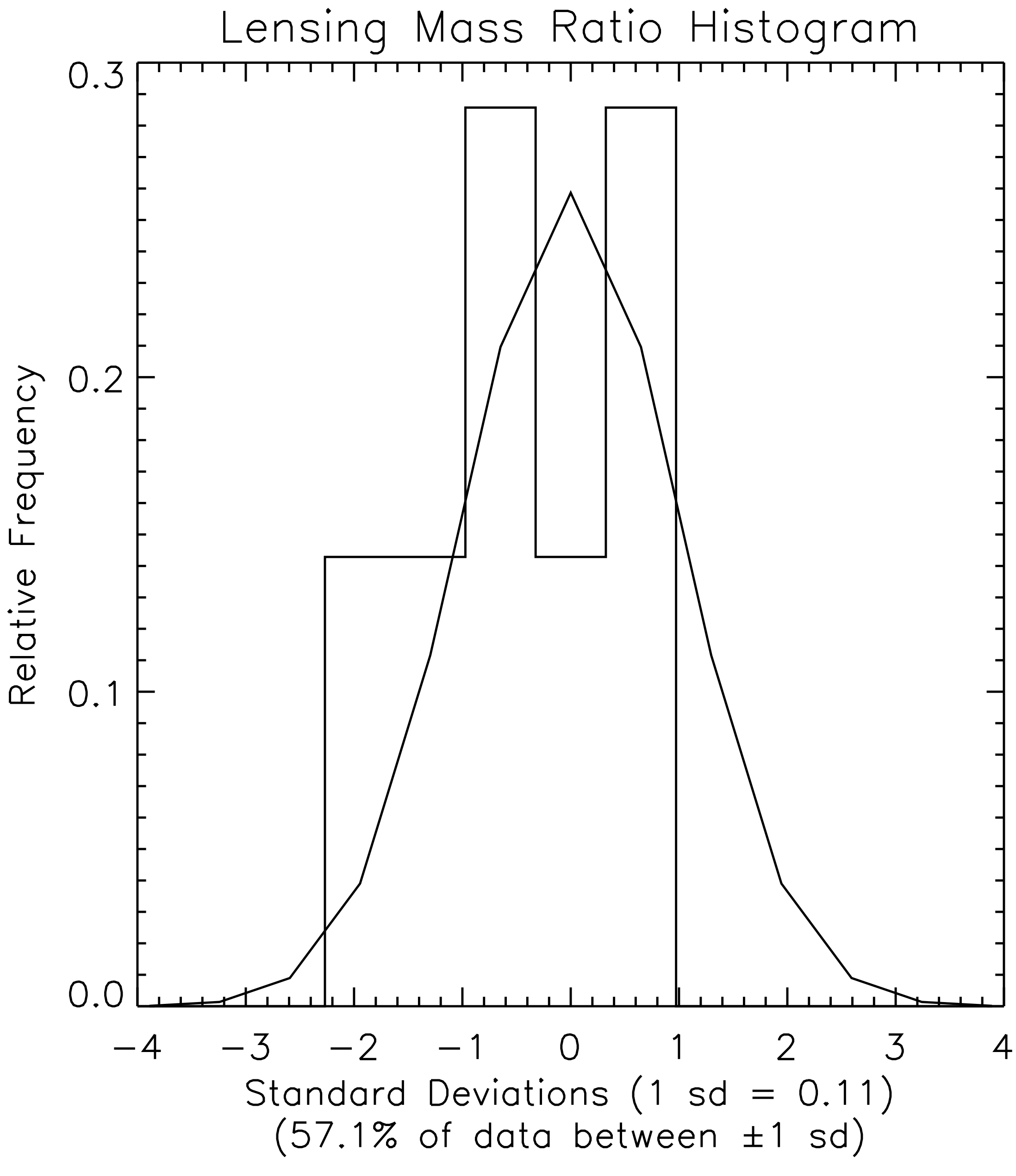

Figure 2.7 Relative frequency histogram of the log of weak lensing/X-ray mass ratios with a normal curve overlaid. X-axis units are in standard deviations. One standard deviation represents a change in ratio of 0.29, with zero indicating a mean ratio of 1.2.

tained by fixing X-ray temperatures at the values determined for cooling core corrected spectra (Table 2.5). To convert 2-10 keV luminosities to bolometric X-ray luminosities, correction factors were obtained via PIMMS for each individual cluster, using a thermal bremsstrahlung model and the spectrally determined temperature of the cluster. The resulting bolometric luminosities are given in Table 2.9.

A linear least-squares fit was then performed on the data. To correct for cosmological effects, a form similar to Allen, Schmidt, & Fabian (2001) [4] was adopted:

$$\left(\frac{L_{2500}}{10^{44}\ \mathrm{erg\ s^{-1}\ E_z}}\right) = C_1\,(\mathrm{kT}_{2500})^{C_2} \tag{2.10}$$

where $E_z = H_z/H_0 = \left[\Omega_m(1+z)^3 + \Omega_\Lambda\right]^{1/2}$. The best fitting values were $C_1 = 0.26^{+0.1}_{-0.08}$ and $C_2 = 2.1 \pm 0.2$, with a reduced χ^2 of 1.51. While this slope is significantly lower than some estimates (Arnaud & Evrard 1999 [9]; Ettori, DeGrandi, & Molendi 2002 citeettori02; Ettori et al. 2004 [46]), it is consistent with both Allen, Schmidt, & Fabian (2001) [4] and a theoretically expectied slope of 2 (Voit 2004 [116]). The scatter in luminosity ($\left[\sum_{i=1,N}(log\ L_{\mathrm{j,obs}} - log\ L_{\mathrm{j,meas}})^2/N\right]^{1/2}$) is 0.22 in log space. This is a smaller scatter than Ettori et al. 2004 [46] find ($\sigma_Y = 0.35$), however he has included significantly higher redshift clusters in his fit. A plot of the data with our relationship overlaid is presented in Figure 2.8.

2.8.2 The Mass$-T_X$ Relationship

A linear least-squares fit was also performed between cluster temperatures and mass estimates. This relationship takes the form:

$$(E_z M_{tot}) = C_1\,(\mathrm{kT})^{C_2} \tag{2.11}$$

[46]. The best fitting values were $C_1 = 8^{+4}_{-3} \times 10^{13}$ and $C_2 = 1.5 \pm 0.2$, with a reduced χ^2 of 1.58, consistent with an expected slope of 1.5 [116]. The scatter in mass is 0.10 in

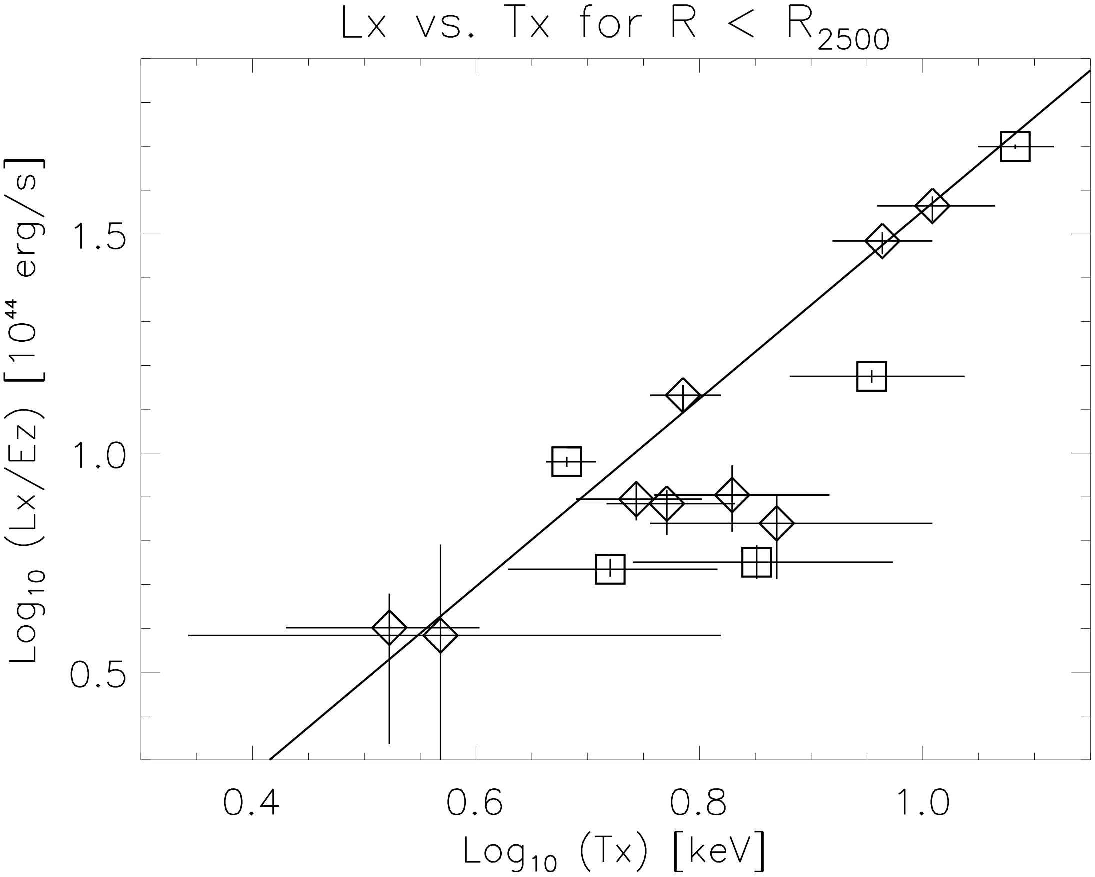

Figure 2.8 X-ray temperatures are plotted against cosmologically corrected unabsorbed bolometric luminosities within R_{2500}. Squares represent clusters with cool cores. The solid line indicates the best fitting relationship, with a slope of 2.1 ± 0.2. Error bars indicate 90% confidence limits.

log space and is again lower than that of Ettori et al. 2004 [46] ($\sigma_Y = 0.15$). A plot of the data with our relationship overlaid is presented in Figure 2.9

2.9 X-ray Properties and Optical Richness

The galaxy-cluster spatial covariance amplitude, B_{gc} (Longair & Seldner 1979 [84]; Yee and Lopez-Cruz 1999 [124]), is a parameter which describes the optical richness of a cluster of galaxies. In essence it is simply a measure of galaxy overdensity within a given aperture, normalized for the expected spatial distribution of galaxies in the cluster and the evolving galaxy luminosity function (Section 1.3.4.4).

One of the challenges in the calculation of B_{gc} involves the lack of a complete knowledge of the galaxy luminosity function at high redshifts. This uncertainty can be minimized by employing the parameter $B_{gc,red}$ (Gladders & Yee 2005 [63]), which is essentially the same as B_{gc}, but is calculated using only galaxies in the red-sequence. In this work we will use only the parameter $B_{gc,red}$. Values of $B_{gc,red}$ for this sample which were obtained from deep CFHT 3.6m observations from the CNOC archive (Yee, Ellingson & Carlberg [20]; H.K.C. Yee 2005, private communication), as well as the cluster X-ray luminosities obtained in Section 2.5.2, are given in Table 2.9.

B_{gc} has previously been shown to correlate strongly with the X-ray properties of relaxed clusters (Yee & Ellingson 2003 [125]). Extending the simple relationships expressed in Yee & Ellingson (2003) [125] to $B_{gc,red}$ one finds

$$B_{gc,red} \propto T_X^{\gamma/2} \tag{2.12}$$

$$B_{gc,red} \propto r_{200}^{\gamma} \tag{2.13}$$

and using our best fit $L_X - T_X$ and Mass$-T_X$ relationships (Section 2.8), in combination with Equation 2.12

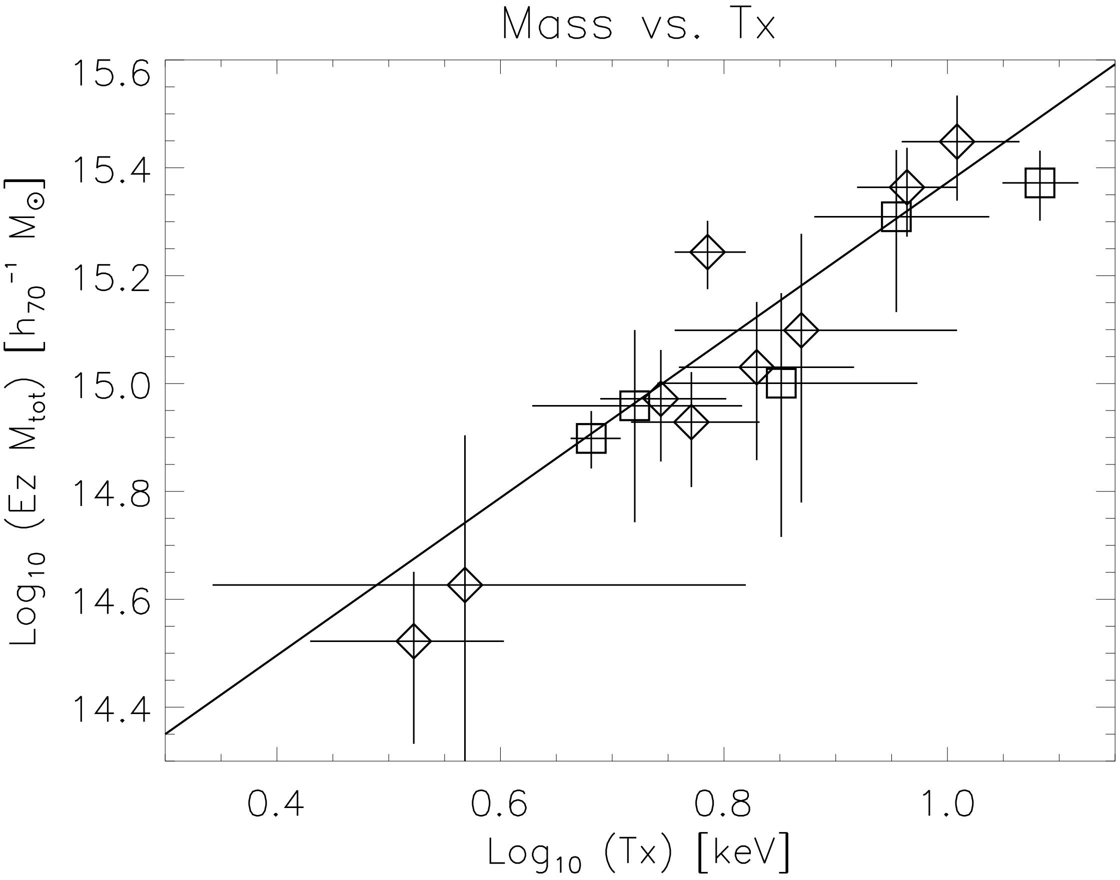

Figure 2.9 X-ray temperatures are plotted against X-ray derived masses within R_{200}. Squares represent clusters with cool cores. The solid line indicates the best fitting relationship, with a slope of 1.5 ± 0.2. Error bars indicate 90% confidence limits.

Table 2.9. Cluster Richness and Luminosity

Cluster	L_x [a] [10^{44} erg s^{-1}]	Bgc_{red} [Mpc$^{1.77}$]
Abell 2390	$56.1^{+0.2\mathrm{b}}_{-0.2}$	1473 ± 218
MS 0015.9+1609	$41.0^{+0.7}_{-1}$	1789 ± 260
MS 0302.7+1658	5^{+1}_{-1}	762 ± 201
MS 0440.5+0204	$6.2^{+0.2}_{-0.2}$	559 ± 154
MS 0451.5+0250	$15.0^{+0.3}_{-0.5}$	1198 ± 208
MS 0451.6-0305	$49.1^{+0.9}_{-1.}$	1232 ± 180
MS 0839.8+2938	$5.97^{+0.1}_{-0.08}$ [b]	1106 ± 187
MS 0906.5+1110	$8.5^{+0.3}_{-0.3}$	1134 ± 209
MS 1006.0+1202	$9.2^{+0.6}_{-0.6}$	1330 ± 216
MS 1008.1-1224	$9.0^{+0.3}_{-0.5}$	1444 ± 212
MS 1358.4+6245	$17.7^{+0.2\mathrm{b}}_{-0.2}$	1182 ± 205
MS 1455.0+2232	$10.9^{+0.1\mathrm{b}}_{-0.1}$	518 ± 154
MS 1512.4+3647	$4.9^{+0.4}_{-0.8}$	582 ± 180
MS 1621.5+2640	$8.7^{+0.5}_{-0.8}$	996 ± 199

[a]Unabsorbed bolometric X-ray luminosity for $R < R_{2500}$

[b]Cooling core corrected

Table 2.10. Fitting Parameters

Relationship	C_1	C_2
$T_X - B_{gc,red}$	$2.4^{+0.3}_{-0.3} \times 10^{-3}$	1.13
$\mathrm{R}_{200} - \mathrm{B}_{\mathrm{gc,red}}$	$3.8^{+0.3}_{-0.2} \times 10^{-2}$	0.56
${E_z}^{-1} L_X - B_{gc,red}$	$7^{+2}_{-2} \times 10^{-7}$	2.37
$E_z\mathrm{M}_{200} - \mathrm{B}_{\mathrm{gc,red}}$	$8^{+2}_{-2} \times 10^{9}$	1.69

$$B_{gc,red} \propto \left(\frac{L_X}{E_z}\right)^{\gamma/4.2} \tag{2.14}$$

and

$$B_{gc,red} \propto E_z {M_{200}}^{\gamma/3} \tag{2.15}$$

In this section we derive the best fitting relationships between cluster X-ray properties and $B_{gc,red}$ for our sample. A generic form for these relationships of

$$\mathrm{X} = \mathrm{C}_1 \times {\mathrm{B}_{\mathrm{gc,red}}}^{\mathrm{C}_2} \tag{2.16}$$

is adopted, where X represents the particular property being fit. For T_X, M_{200}, R_{200}, and L_X/E_z, units of keV, $\mathrm{M}_\odot$, Mpc, and 10^{44}erg s^{-1} were used, respectively. Initial linear least-squares fitting was performed which allowed both C_1 and C_2 to vary, however neither parameter was particularly well constrained by the data in that case. A value of $\gamma = 1.77$ (Yee & Ellingson 2003 [125]) was consistent with each of the indvidual fits, so additional fitting was undertaken with γ fixed at that value.

The data, with the results of the fixed γ fits overlaid, are shown in Figures 2.10-2.16. Best fitting parameters of the constrained fits are given in Table 2.10.

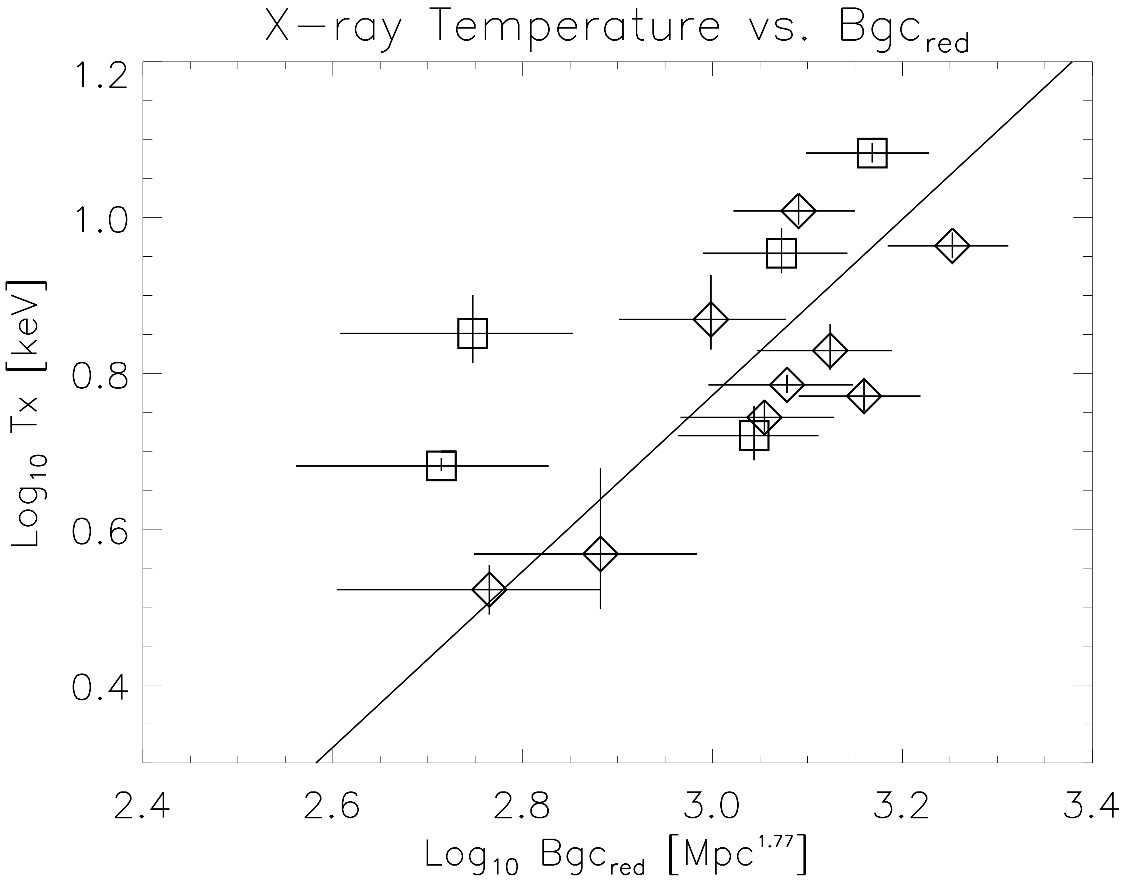

Figure 2.10 A log-log plot of T_X vs. $B_{gc,red}$ for the clusters in our sample. Error bars represent 68% confidence intervals. The line indicates the best fitting relationship between these two parameters given $\gamma = 1.77$ (Section 2.9). Squares denote clusters which exhibit significant cool cores.

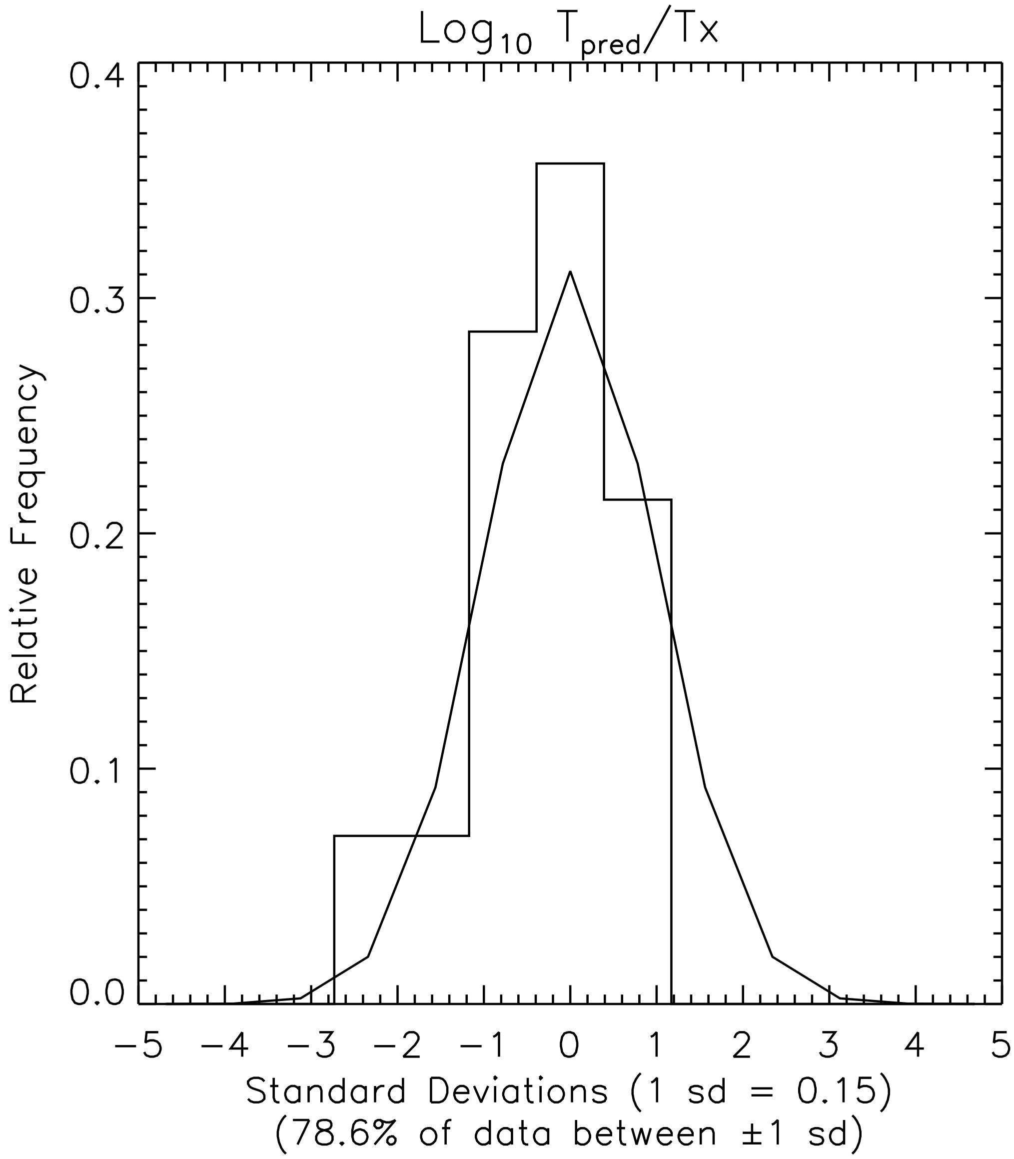

Figure 2.11 Relative frequency histogram of the log of the ratio between B_{gc} predicted temperature and measured temperature, with a normal curve overlaid. X-axis units are in standard deviations. One standard deviation represents a change in ratio of 0.41, with zero indicating a mean ratio of 0.94.

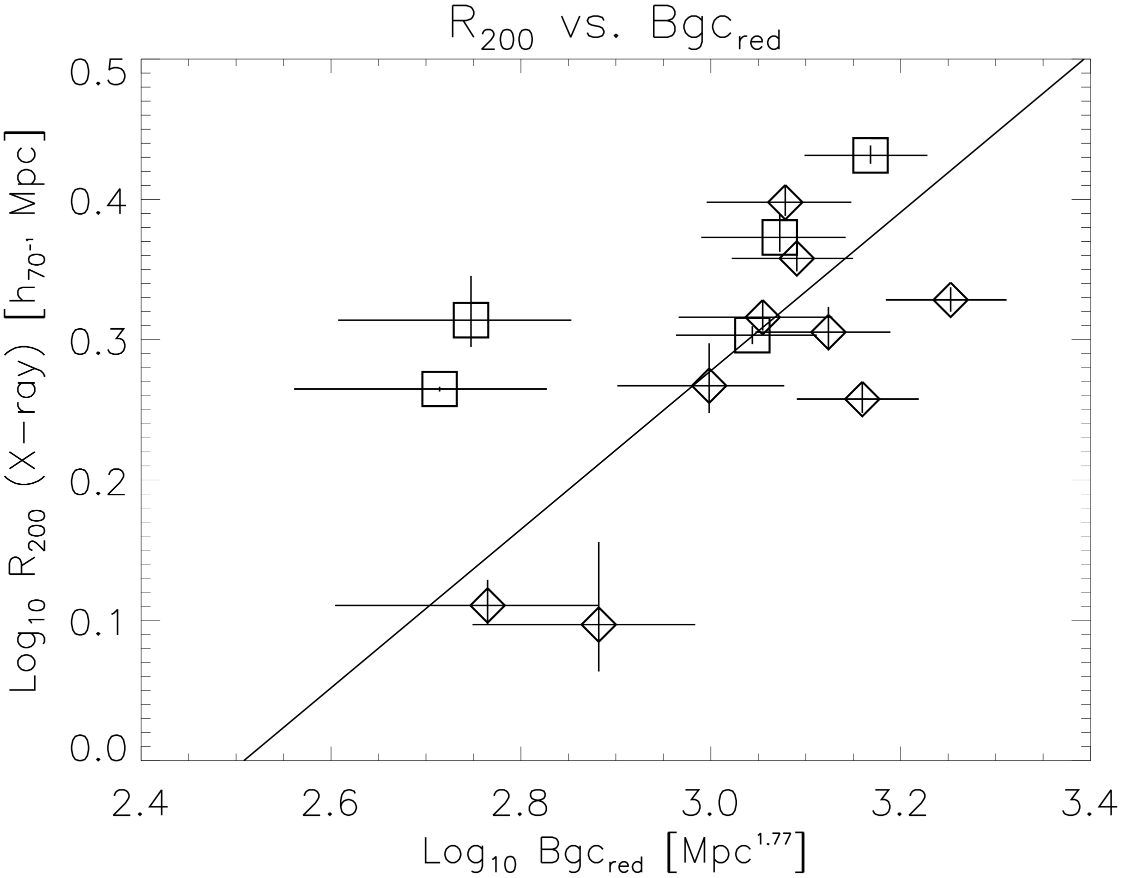

Figure 2.12 A log-log plot of R_{200} vs. $B_{gc,red}$ for the clusters in our sample. Error bars represent 68% confidence intervals. The line indicates the best fitting relationship between these two parameters given γ = 1.77 (Section 2.9). Squares denote clusters which exhibit significant cooling.

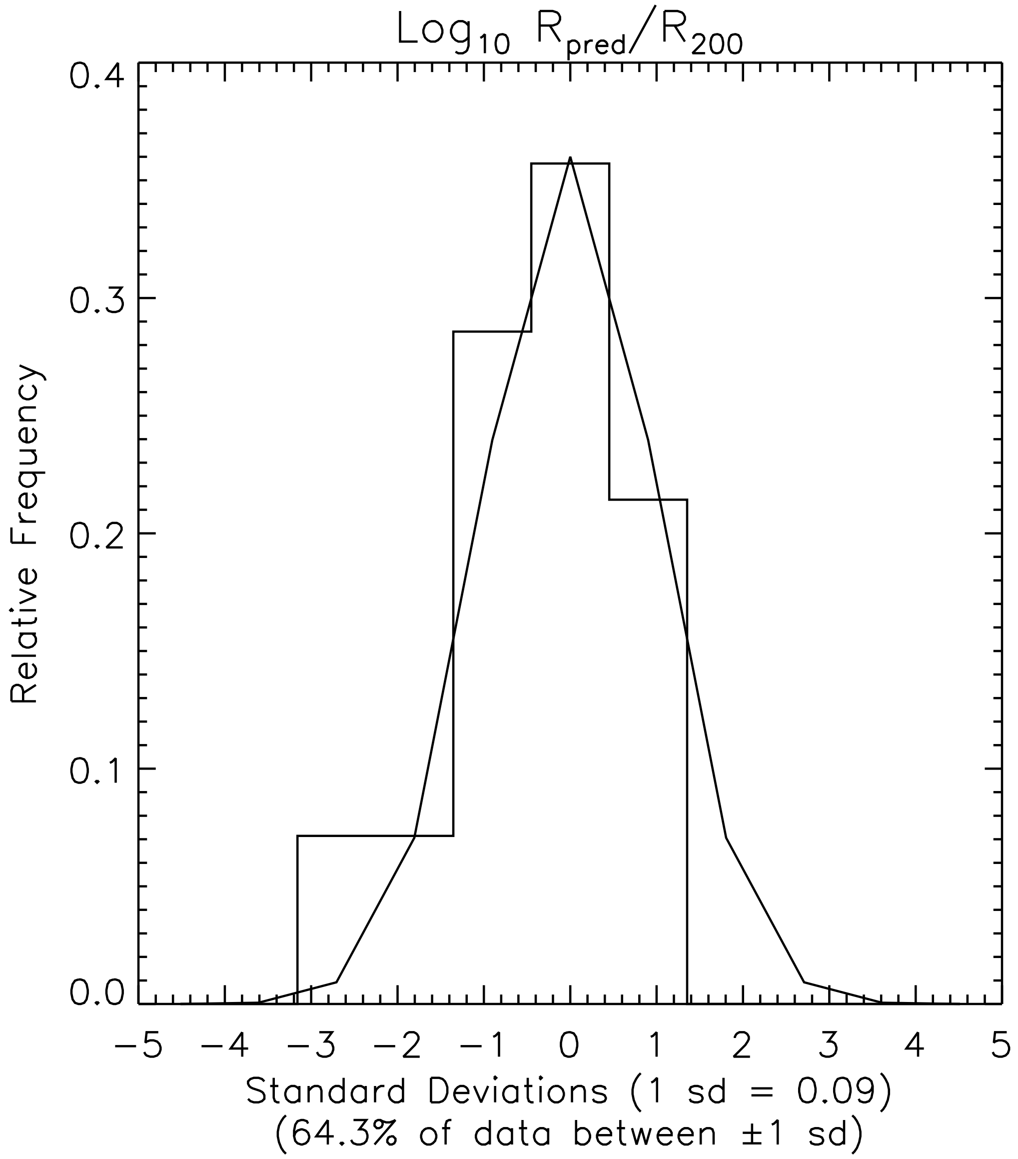

Figure 2.13 Relative frequency histogram of the log of the ratio between B_{gc} predicted R_{200} and X-ray predicted R_{200}, with a normal curve overlaid. X-axis units are in standard deviations. One standard deviation represents a change in ratio of 0.23, with zero indicating a mean ratio of 0.98.

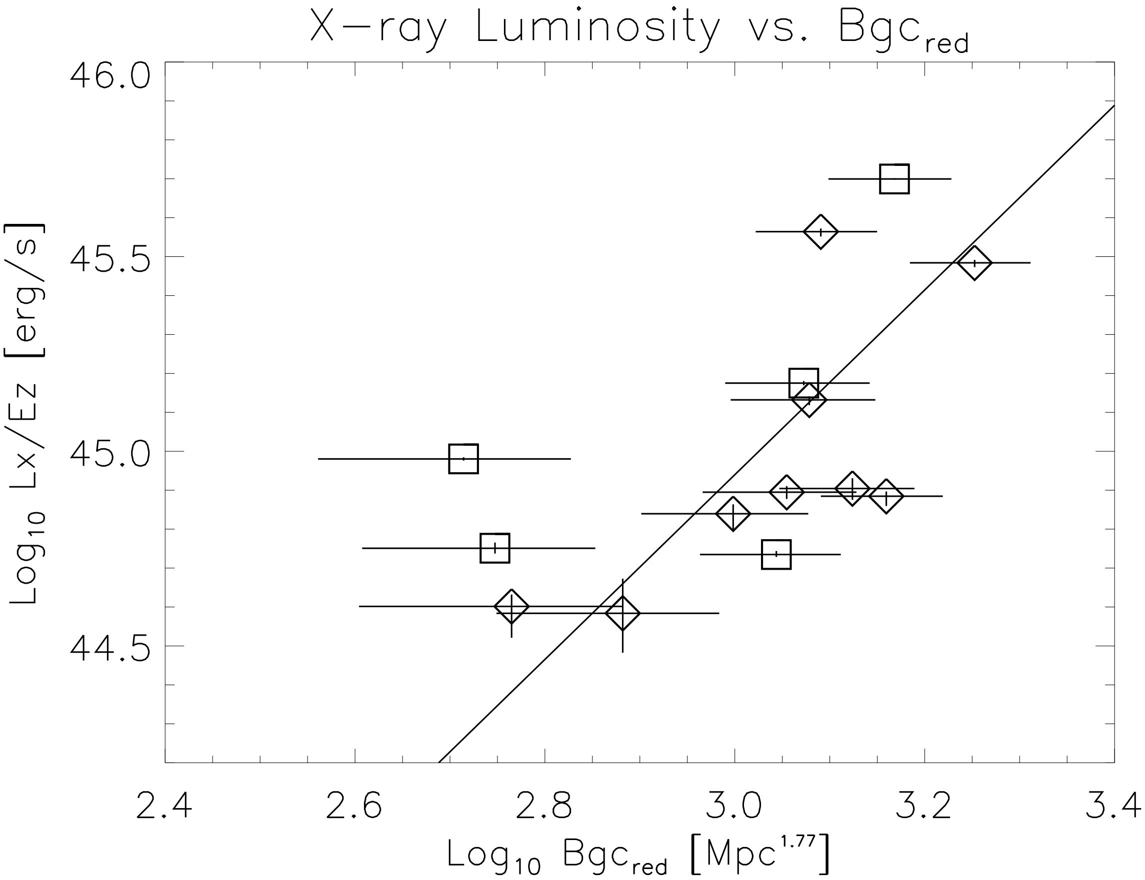

Figure 2.14 A log-log plot of L_X vs. $B_{gc,red}$ for the clusters in our sample. Error bars represent 68% confidence intervals. The line indicates the best fitting relationship between these two parameters given $\gamma = 1.77$ (Section 2.9) and $L_X \sim {T_X}^{2.1}$ (Section 2.8.1). Squares again denote clusters which exhibit significant cool cores.

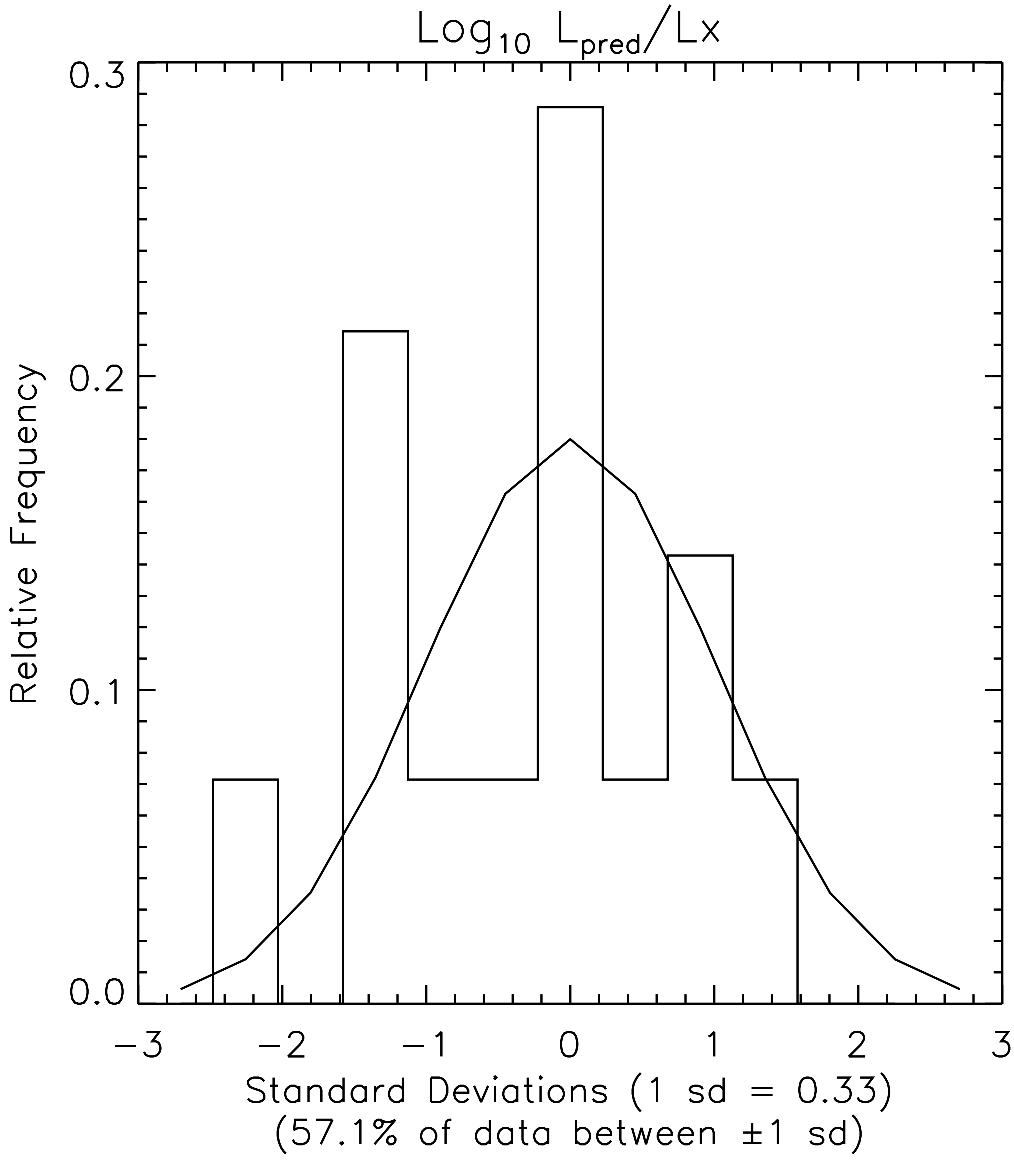

Figure 2.15 Relative frequency histogram of the log of the ratio between B_{gc} predicted L_X and measured L_X, with a normal curve overlaid. X-axis units are in standard deviations. One standard deviation represents a factor of two difference between predicted and measured luminosities, with zero indicating a mean ratio of 0.89.

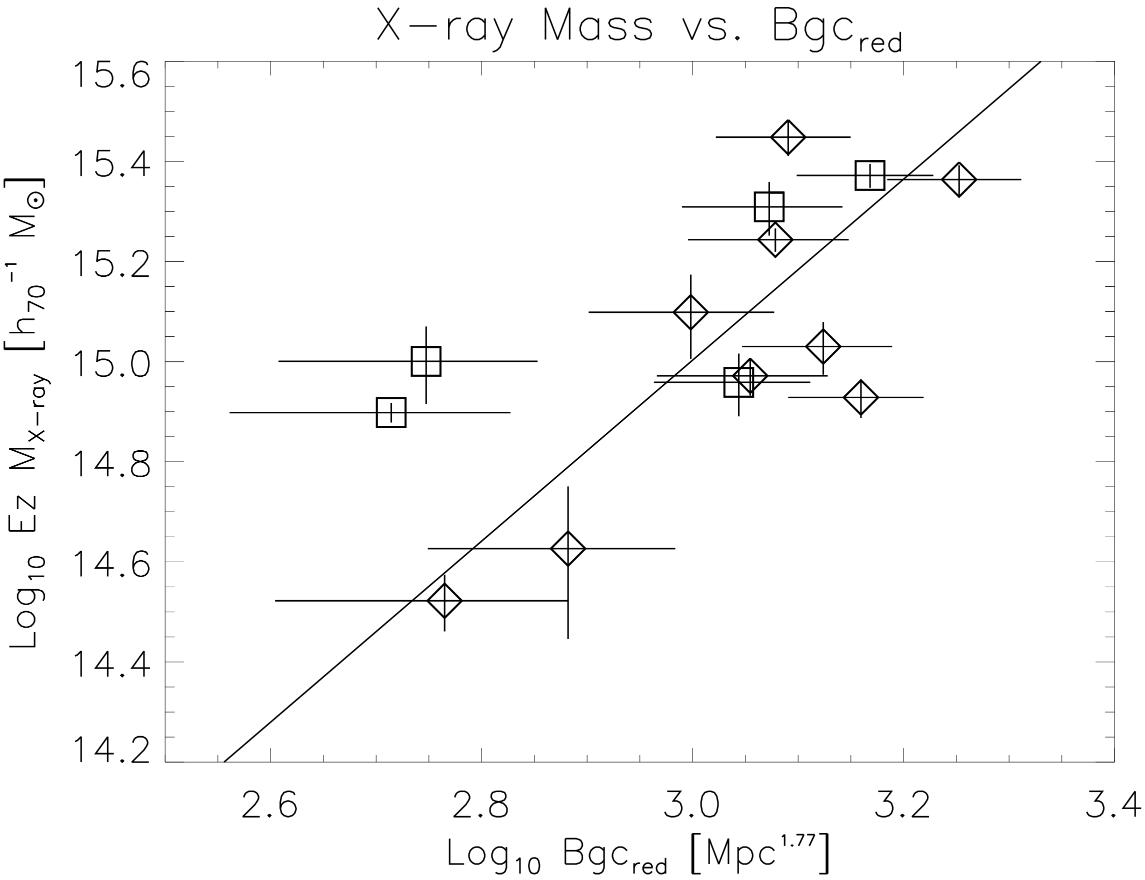

Figure 2.16 A log-log plot of X-ray mass estimates vs. $B_{gc,red}$ for the clusters in our sample. Error bars represent 68% confidence intervals. The line indicates the best fitting relationship between these two parameters given $\gamma = 1.77$ (Section 2.9) and Mass$\sim T_X{}^{1.6}$ (Section 2.8.2). Squares denote cooling core clusters.

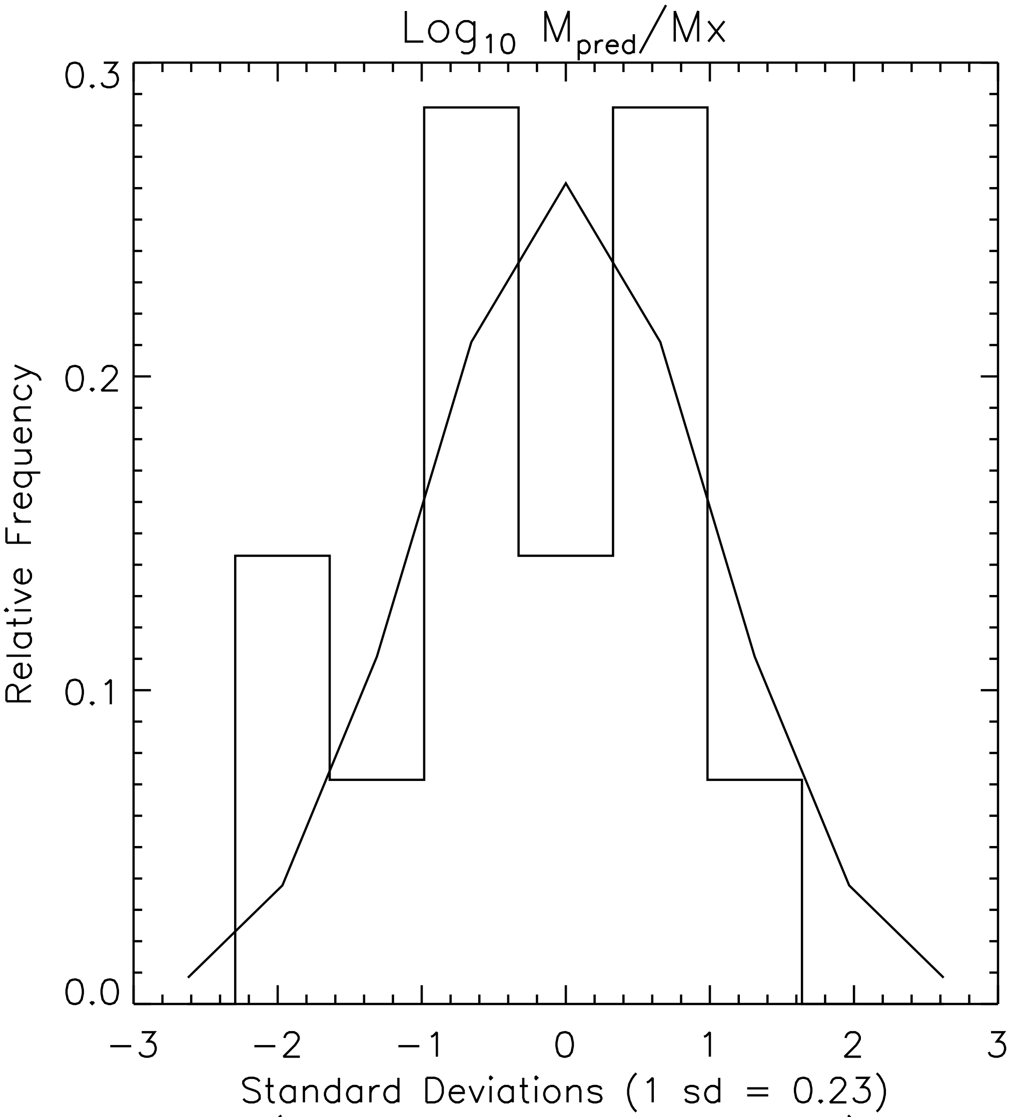

Figure 2.17 Relative frequency histogram of the log of the ratio between B_{gc} predicted mass and X-ray mass estimates, with a normal curve overlaid. X-axis units are in standard deviations. One standard deviation represents a change in ratio of 0.7, with zero indicating a mean ratio of 0.95.

2.10 Summary and Discussion

We have presented a comprehensive analysis of Chandra observations of 14 medium redshift ($0.1709 < z < 0.5466$) clusters of galaxies from the CNOC subsample of the EMSS (Table 2.1). This work, which explores in detail the properties of X-ray selected clusters, paves the way for a comparison with and characterization of optically selected high redshift clusters.

Imaging analysis has provided information on the relative quiescence of each cluster (Figure 2.1). Clusters exhibiting significant substructure include MS0451+02, MS1006+12, and MS1008-12. The spatial resolution of Chandra has allowed us to determine the surface brightness profiles of these clusters down to $1''$ scales (Figure 2.2). This has enabled us to obtain precise models of cluster emission (Table 2.2), except in the case of MS0451+02 which displays a considerable amount of substructure. Five clusters in our sample (Abell 2390, MS0440+02, MS0839+29, MS1358+62, and MS1455+22) exhibit excess emission in their cores, indicating the presence of cool gas. The surface brightnesses of these five clusters are better fit with the inclusion of a second β component to model the excess core emission (Table 2.3).

Chandra's $0.5''$ spatial resolution has enabled us to study the radial distribution of temperatures on small scales ($\sim 7 - 100$ kpc) in the inner 150-600 kpc of eleven of these objects (Figure 2.3). While nine clusters in our sample have temperature profiles which are consistent with isothermality, the five cooling core clusters (listed above) show clear temperature gradients in their innermost $\sim 60 - 150$ kpc.

The energy resolution of the instrument has provided well constrained spectral analyses of the central R_{2500} ($\sim 350 - 760$) kpc of each object. Temperatures obtained initially from 300 kpc radius extraction regions began an iterative spectral extraction and fitting process culminating in the determination of robust integrated temperatures, luminosities, and abundances within R_{2500} (Tables 2.4 and 2.5). Cooling core corrected spectra were used to determine global temperatures for the clusters in our sample which exhibit significant cooling. These temperatures were then employed in the spectral determination of integrated luminosities for these objects. Overall, our sample displays temperatures in the range of $3.4 - 12.1$ keV, abundances which range from $0.1 - 0.8$ times the solar value, and unabsorbed bolometric luminosities within R_{2500} which span $4.9 - 56.1 \times 10^{44}$ erg s^{-1}.

Cluster gas and total masses within R_{200} were estimated using the outcomes of spectral and surface brightness fitting, resulting in total cluster masses of $2.7 - 21 \times 10^{14}\ h_{70}^{-1}\ M_\odot$ (Table 2.6) and cluster gas masses of $0.13 - 2.9 \times 10^{14}\ h_{70}^{-1}\ M_\odot$. A weighted average of gas mass fractions gives $f_{gas} = 0.080 \pm 0.003\ h_{70}^{-1}$, resulting in $\Omega_m = 0.32 \pm 0.03$ (68% confidence).

Dynamical masses within R_{200} were calculated via the Jeans Equation using velocity dispersions taken from Borgani et al. 1999 [18] (Table 2.7). Comparisons between X-ray masses and dynamical masses result in a weighted average of $M_{\rm dyn}/M_{\rm X-ray} = 0.96 \pm 0.06$, though a fair amount of scatter is evident ($\sim 30\%$; Figure 2.4). Dynamical masses are noticeably larger in the case of clusters which exhibit significant substructure (MS1006+12 and MS1008-12), a factor which may be responsible for an overestimation of velocity dispersions (Bird 1994 [15]). A histogram of these ratios with fitted normal curve (Figure 2.5) indicates a mean ratio of 1.0 ± 0.02 with a standard deviation of 0.32.

Weak lensing masses within 500 h_{100}^{-1} kpc were obtained for seven of the clusters in our sample from H. Hoekstra (2005, private communication). X-ray masses were calculated within this region and compared to the lensing results (Table 2.8). Weak lensing mass estimates appear systematically larger than the corresponding X-ray mass estimates (Figure 2.6), which is expected due to projections along the line of sight (Cen 1997 [23]; Floor & Evrard [50]; Hoekstra 2003 [76]). A weighted average gives $M_{\rm lens}/M_{\rm X-ray} = 1.10 \pm 0.09$, and the histogram of these ratios with fitted normal curve (Figure 2.7) indicates a mean ratio of 1.2 ± 0.04 with a standard deviation of 0.29.

X-ray scaling laws for this sample were investigated in a manner similar to Allen, Schmidt, & Fabian (2001) [4] and Ettori et al. (2004) [46], taking cosmological factors into account. The best fitting $L_X - T_X$ relationship for our sample results in an intercept of $0.26^{+0.1}_{-0.08}$ and a slope of 2.1 ± 0.2 (Figure 2.8). While this slope is significantly lower than some estimates (Arnaud & Evrard 1999 [9]; Ettori, DeGrandi, & Molendi 2002 [44]; Ettori et al. 2004 [46]), it is consistent with both Allen, Schmidt, & Fabian (2001) [4] and the theoretically expected slope of 2. The Mass-T_X relationship for these clusters has an intercept of $8^{+4}_{-3} \times 10^{13}$ and a slope of 1.5 ± 0.2 (Figure 2.9), which is identical to the expected slope for this relationship (Voit 2004 [116]).

The best fitting scaling laws for our sample (listed above) were combined with equations 3 and 4 in Yee and Ellingson (2003) [125] with the ultimate goal of calibrating relationships between red-sequence optical richness ($B_{gc,red}$) and global cluster parameters (T_X, R_{200}, L_X and M_{200}). For fitting purposes, γ was fixed at a fiducial value of 1.77. While T_X, R_{200}, and M_{200} scale relatively well to $B_{gc,red}$ (Figures 2.10,2.12, and 2.16), the L_X relationship exhibits substantially more scatter (Figure 2.14).

Chapter 3

Optically Selected Clusters at High Redshift: the RCS Sample

3.1 Introduction

The Extended Medium Sensitivity Survey (EMSS; Gioia et al. 1990 [57]) sparked the beginnings of an ongoing search for clusters of galaxies at high redshift. Since then numerous high redshift surveys have been carried out, both optically (e.g. Gilbank et al. 2004 [56]; Donahue et al. 2002 [31]; Postman et al. 1996 [100]), and in the X-ray (e.g. Valtchanov et al. 2004 [114]; Bauer et al. 2002 [13]; Wilkes et al. 2000 [121]). The motivations for such searches are multifaceted, but the most compelling of these are cosmological in nature.

Clusters of galaxies are an important source of information about the underlying cosmology of the universe. They are essentially "closed boxes", meaning that the primordial matter that they were initially composed from has remained trapped in their deep potential wells since they were formed. This makes them ideal objects with which to study galaxy formation and evolution. In addition, clusters are the largest virialized objects in the universe. By virtue of this fact we are able to, through high redshift samples, investigate the growth of large scale structure in the universe. A firm knowledge of the evolution of the cluster mass function would provide a huge contribution to constraining cosmological parameters such as σ_8 (the normalization of the density perturbation spectrum) and w (the dark energy equation of state).

Two ingredients are required to achieve this goal. First, a statistically significant sample of clusters in multiple redshift bins is needed. Secondly, reliable mass estimates of the clusters in that sample must be obtained. Difficulties in reaching the first requirement include the vast amount of telescope time required to carry out such a search in the X-ray, and the propensity for false detections due to projection effects in optical surveys. The primary challenge in reaching the second part of this goal is again the high cost of observing time to achieve either X-ray or dynamical mass estimates.

The Red-sequence Cluster Survey (RCS; Gladders & Yee 2000, 2005 [62, 63]) has attempted to evade such difficulties. RCS is a 1000 deg^2 optical survey which uses the color-magnitude relationship of cluster ellipticals to find galactic overdensities in small slices of redshift space. This technique has been estimated to bring false detection rates down to $\sim 5\%$. The chosen filters (r and z'), optimize this finding algorithm for the redshift range $0.2 < z < 1.4$ and provide photometric redshift information with accuracies of $\sim 10\%$. In addition, optical richness information is immediately available from the survey data and, if sufficiently calibrated, this information could provide a highly efficient way to estimate the masses of cluster candidates.

The first installment of the Red-Sequence Cluster Survey (RCS1; Gladders & Yee 2005 [63]) covers 90 square degrees and was performed at CFHT and CTIO. RCS1 has identified between 3500 and 4000 clusters total in the redshift range $0.2 < z < 1.2$, over 1500 of which are at least as optically rich as Abell class 0 clusters (Gladders & Yee 2005 [63]). Simulations indicate that the survey is complete to Abell Class 1 at a redshift of 1 for blue fractions less than 0.45.

The motivations for this work are to both characterize high redshift optically selected cluster samples, and move forward in attempts to calibrate a robust relationship between optical richness and cluster mass. This paper presents the first detailed analysis of nine Chandra observations of RCS1 clusters with redshifts in the range $0.64 < z < 1.1$ Our analysis investigates the temperatures and gas distributions of six of these clusters, and provides mass estimates for use in the calibration of relationships between optical richness and cluster mass. We also use our results to investigate the X-ray scaling laws of our sample.

3.2 Cluster Sample & Observations

Chandra Advanced CCD Imaging Spectrometer (ACIS) observations of nine RCS clusters were taken during the period 10 April 2002 - 13 April 2005. Eight of these clusters were observed with the ACIS-S CCD array, and one was observed with ACIS-I, with an overall range in individual exposures of $9.9 - 89.0$ kiloseconds. Four of the clusters in this sample were observed on multiple occasions, and for three of these (RCS0439-2904, RCS1326+2903, and RCS2157-0448), we have merged those event files to provide higher overall signal-to-noise. Each of the observations analyzed in this study possesses a focal plane temperature of -120^o C.

Aspect solutions were examined for irregularities and none were found. Background contamination due to charged particle flares was reduced by removing time intervals during which the background rate exceeded the average background rate by more than 20%. The quiescent background was further reduced by using VFAINT mode. The event files were then filtered on standard grades and bad pixels were removed. Table 3.1 provides a list of each of the clusters in our sample, including redshift, obsid, array, and corrected exposure information for each observation.

After the initial cleaning of each data set, 0.29-7.0 keV images, instrument maps, and exposure maps were created using the CIAO tool MERGE_ALL. Data with energies below 0.29 keV and above 7.0 keV were excluded due to uncertainties in the ACIS calibration and background contamination, respectively. Ideally, all data below 0.6 keV would have been excluded to minimize low energy uncertainties, however the combined faintness and high redshifts of our objects require the utilization of lower energy photons as well. Point source detection was performed by running the tools WTRANSFORM and WRECON on the flux images. Figure 3.1 contains smoothed Chandra flux images

Table 3.1. Cluster Sample

Cluster	z	$1''$ $[h_{70}^{-1}$ kpc$]$	obsid	Array	Chandra Exposure [seconds]
RCS0224-0002	0.77	7.42	4987	ACIS-S	88973
RCS0439-2904	0.95	7.91	3577	ACIS-S	49139
			4438	ACIS-S	28753
RCS1107-0523	0.735	7.28	5887	ACIS-S	44592
RCS1326+2903	0.71[a,b]	7.19	3291	ACIS-S	30907
			4362	ACIS-S	32683
RCS1417+5305	1.0[a]	8.01	3239	ACIS-I	62824
RCS1419+5326	0.64	6.88	3240	ACIS-S	9904
RCS1620+2929	0.87	7.71	3241	ACIS-S	34899
RCS2112-6326	1.07	8.133	5885	ACIS-S	68903
RCS2157-0448	0.81[a]	7.55	5353	ACIS-S	36558
			5359	ACIS-S	34701

[a]Photometrically estimated redshift

[b]Most probable redshift. This cluster may be at z=0.93 (see text for explanation)

Table 3.2. Cluster Positions and Detection Significance

Cluster	Optical Position[a] RA	Optical Position[a] Dec	X-ray Position[a] RA	X-ray Position[a] Dec	Counts [σ]	CSMOOTH [σ]
RCS0224-0002	02:24:34.1	-00:02:30.9	02:24:34.195	-00:02:26.92	11.8	3.36
RCS0439-2904	04:39:38.0	-29:04:55.2	04:39:38.0	-29:04:47.67	8.1	3.51
RCS1107-0523	11:07:23.429	-05:23:13.73	11:07:24.049	-05:23:20.47	13.6	3.21
RCS1326+2903[b]	13:26:31	+29:03:12	13:26:30.87	+29:03:28.8	4.3	3.67
RCS1417+5305	14:16:59.8	+53:05:12.2	14:17:02.202	+53:05:20.06	4.7	3.23
RCS1419+5326	14:19:12.1	+53:26:11.0	14:19:12.193	+53:26:10.57	17.3	3.08
RCS1620+2929	16:20:10.0	+29:29:21.5	16:20:10.047	+29:29:20.43	7.0	3.33
RCS2112-6326	21:12:23.06	-63:25:59.48	21:12:28.139	-63:26:33.93	6.4	1.78
RCS2157-0448	21:56:41.202	-04:48:13.30	21:56:41.895	-04:48:04.05	2.0	3.57

[a]All positions are given for equinox J2000.

[b]There is also an RCS cluster at 13:26:29, +29:03:06 (see text for details)

of each of the clusters in our sample.

3.3 Detection Significance and Cluster Positions

Two methods were employed to determine the significance of RCS cluster detections in the X-ray. The first makes use of relatively simple statistics. Counts were extracted from a 500 h_{70}^{-1} kpc radius region around the aimpoint of each observation in the 0.6-7.0 keV band (C), and also in a 500 h_{70}^{-1} kpc region elsewhere on the aimpoint chip to serve as a background (B). Obvious point sources were removed from each region. Detection significance was calculated based on dividing net counts, $N = C - B$, by the standard deviation, $\sigma = \sqrt{C + B}$. Using this method eight cluster signals were detected to greater than 3σ, and all were detected to greater than 2σ (Table 3.2).

The second method of determining detection significance was done with the CIAO tool CSMOOTH. This is a routine which performs adaptive smoothing on counts images and can also produce output significance maps. CSMOOTH estimates the background locally, using the counts in an annulus surrounding the kernel. Using the smoothed images produced from running CSMOOTH on 0.29-7.0 keV counts images, we deter-

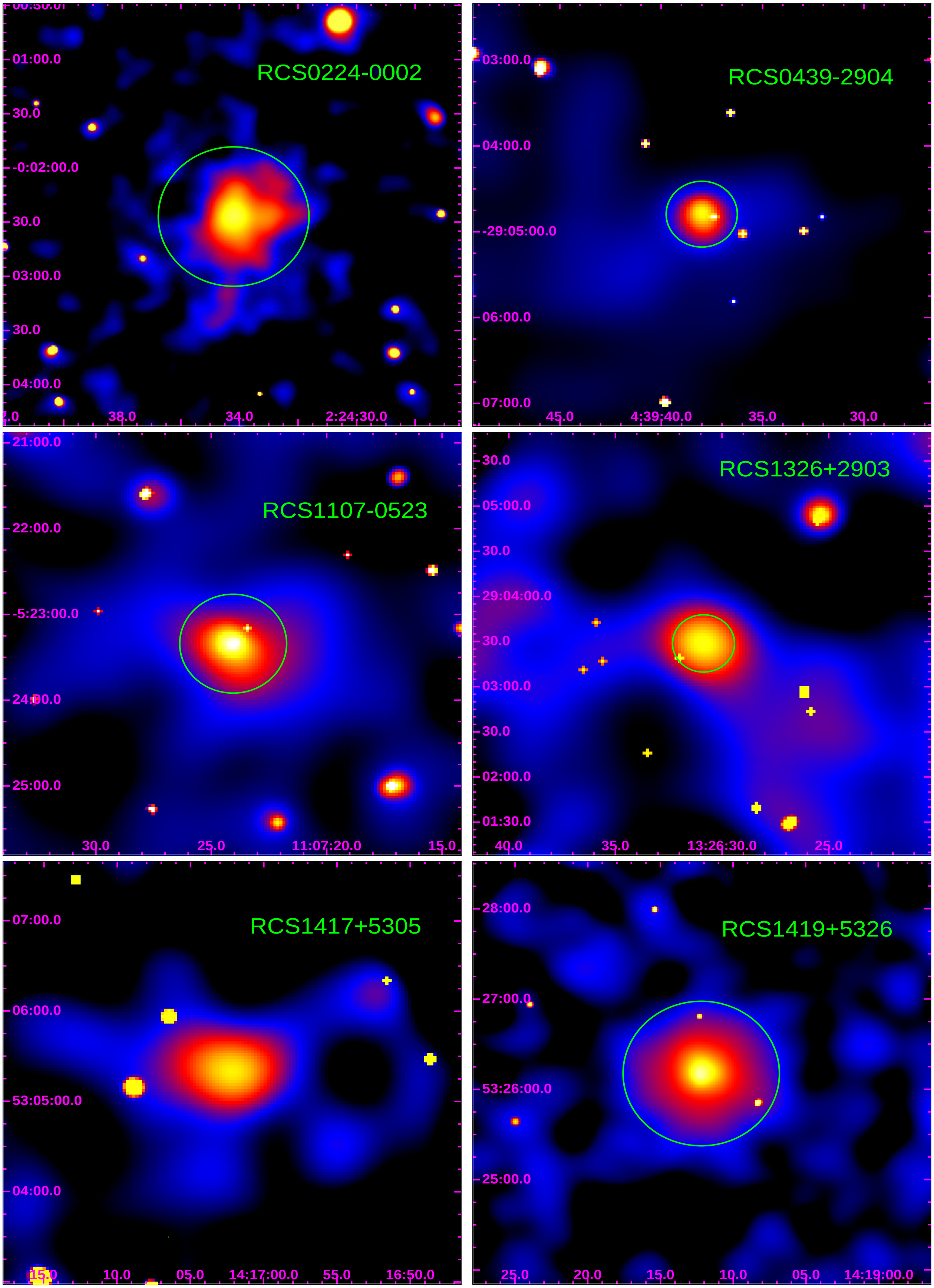
RCS0224-0002
01:00.0
30.0
-0:02:00.0
30.0
03:00.0
30.0
04:00.0
38.0
34.0
2:24:30.0
RCS0439-2904
03:00.0
04:00.0
-29:05:00.0
06:00.0
07:00.0
45.0
4:39:40.0
35.0
30.0
RCS1107-0523
21:00.0
22:00.0
-5:23:00.0
25:00.0
30.0
25.0
11:07:20.0
15.0
RCS1326+2903
30.0
05:00.0
30.0
29:04:00.0
30.0
03:00.0
30.0
02:00.0
01:30.0
40.0
35.0
13:26:30.0
25.0
RCS1417+5305
07:00.0
06:00.0
53:05:00.0
04:00.0
10.0
05.0
14:17:00.0
55.0
16:50.0
RCS1419+5326
28:00.0
27:00.0
53:26:00.0
25:00.0
25.0
20.0
15.0
10.0
05.0
14:19:00.0

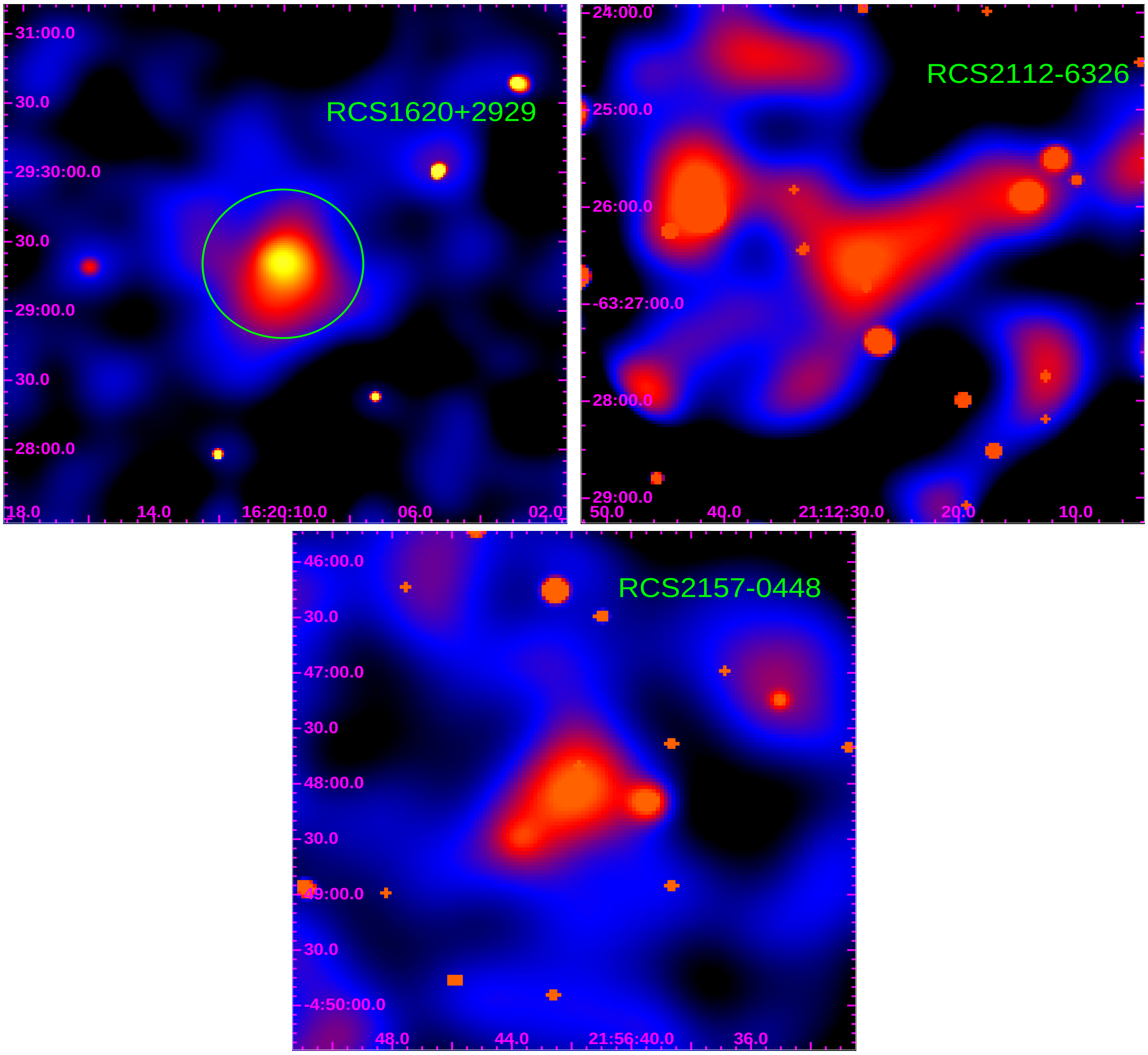

Figure 3.1 Adaptively smoothed X-ray flux images of our sample in the 0.29-7.0 keV band. Circles denote calculated values of R_{2500} for each cluster. The three images which lack circles did not contain enough cluster signal to contrain a β model or a temperature, and thus lack estimates of R_{2500}. In each image, north is up.

mined the location of the X-ray emission peak of each cluster. Significance maps were then used to determine the detection significance at these points. Using this method we again find that eight of the nine clusters in this sample were detected to greater than 3σ at the positions of their X-ray peaks.

In the case of RCS1326+2903, two RCS 13h clusters lie in the field of view. The original observation was designed to observe a $z = 0.93$ cluster at an RA, Dec of 13:26:29, +29:03:06 (J2000). Our astrometry indicates, however, that we are most likely detecting the emission of a lower redshift RCS cluster ($z = 0.71$) at an optical position of 13:26:31, +29:03:12. Because of the uncertainty surrounding this detection, we have carried both possibilities throughout much of our analysis. All other clusters (with the exception of the marginal detection of RCS2112-6326) were found within $10''$ of their optical positions. Table 2.2 lists each cluster, its optical position, its X-ray position, and the detection significances derived from each method described above.

3.4 Surface Brightness

A radial surface brightness profile was computed over the range 0.29-7.0 keV in circular annuli for each cluster. These profiles were then fit with β models (Equation 2.1).

Three of the clusters did not posess enough signal to constrain a β model. Due to a bug in exposure map construction in the MERGE_ALL tool, surface brightness normalizations for the two merged observations (RCS0439-2904 and RCS1326+2903) may run slightly high. Error bars for these parameters have been adjusted using correction factors obtained from comparing the average background value of the remaining observations to that of the merged observations. The parameters of the best fitting models of the six clusters for which surface brightness fitting was possible are shown in table 3.3, and images of these fits are given in Figure 3.2.

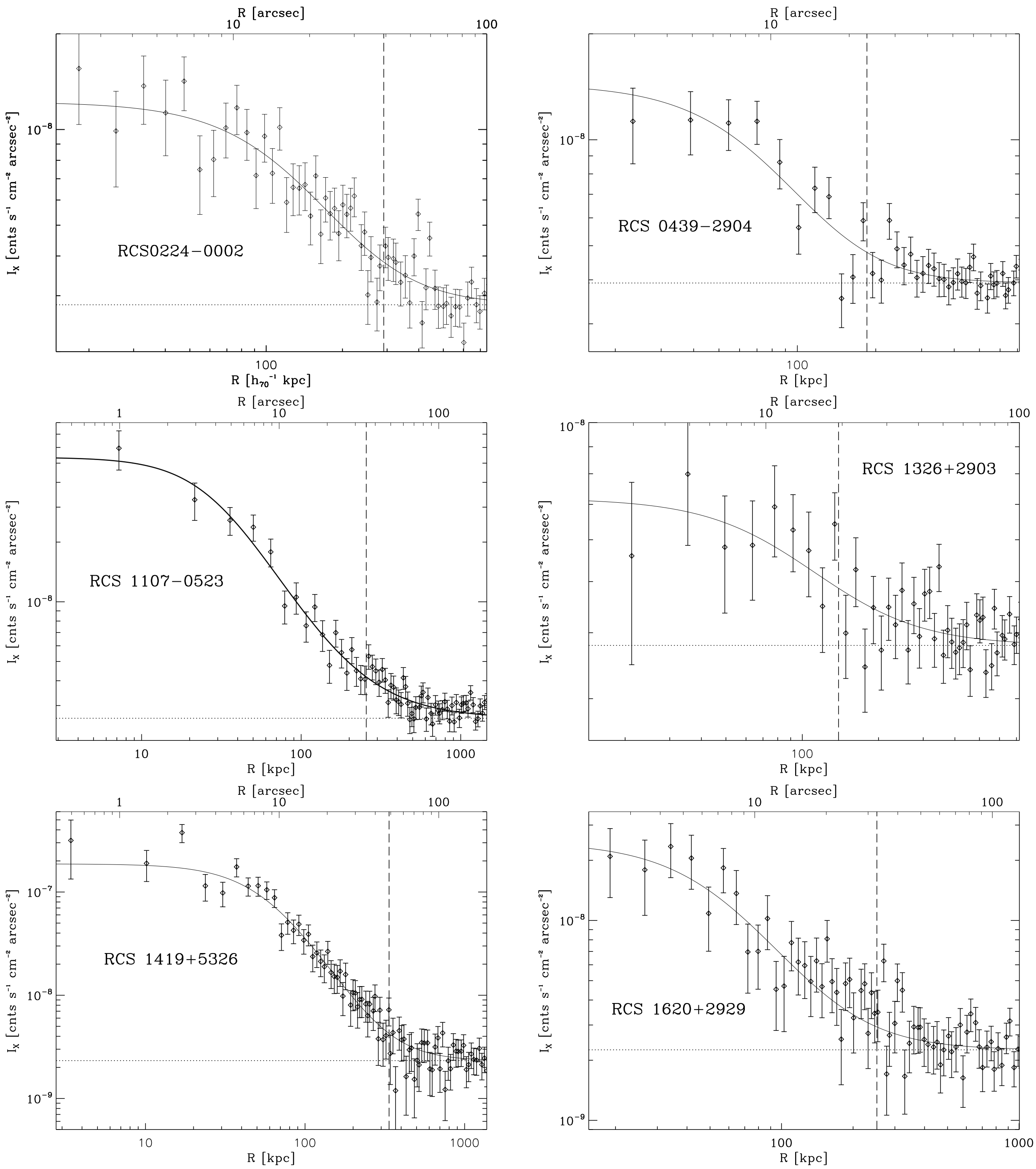

Figure 3.2 Radial surface brighnesses for the 0.29-7.0 keV band accumulated in annular bins for six clusters in our sample. A solid line traces the best fitting β model of each cluster. Dotted lines represent best fit background values, while the vertical dashed line denotes R_{2500} for each cluster.

Table 3.3. β-Model Fits

Cluster	R_c $[h_{70}^{-1}$ kpc$]$	β	I_0 [a]	I_B [a]	χ^2/DOF
RCS0224-0002	143^{+29}_{-24}	$0.6^{+0.1}_{-0.1}$	9^{+2}_{-1}	$2.8^{+0.2}_{-0.2}$	151.5/101
RCS0439-2904	82^{+16}_{-14}	$0.6^{+0.1}_{-0.1}$	10^{+2}_{-5}	$3.9^{+0.1}_{-1.5}$	55.6/54
RCS1107-0523	29^{+9}_{-5}	$0.43^{+0.04}_{-0.03}$	51^{+10}_{-5}	$2.6^{+0.1}_{-0.2}$	84.4/88
RCS1326+2903	105^{+21}_{-17}	$0.51^{+0.1}_{-0.09}$	$3.8^{+0.2}_{-1.6}$	$3.4^{+0.7}_{-1.6}$	38.6/45
RCS1419+5326	62^{+12}_{-10}	$0.61^{+0.07}_{-0.05}$	185^{+37}_{-31}	$2.3^{+0.1}_{-0.2}$	132.4/153
RCS1620+2929	58^{+12}_{-10}	$0.56^{+0.09}_{-0.07}$	22^{+4}_{-4}	$2.25^{+0.07}_{-0.08}$	144/152

[a] Surface brightness I in units of 10^{-9} photons sec^{-1} cm^{-2} arcsec^{-2}

3.5 Spectral Analysis

3.5.1 Integrated Spectral Fits and R_{2500}

Spectra were extracted from each cleaned event file in a circular region with a 300 h_{70}^{-1} kpc radius. These spectra were then analyzed with XSPEC (Arnaud 1996 [8]), using weighted response matrices (RMFs) and effective area files (ARFs) generated with the CIAO tool ACISSPEC and the latest version of the Chandra calibration database (CALDB 3.0.1). 100 pixel radius circular backgrounds were extracted from the aim point chip as far away from the aimpoint as possible.

Spectra were fitted with single temperature spectral models, inclusive of foreground absorption. Each spectrum was fit with the absorbing column frozen at its measured value (Dickey & Lockman 1990 [28]). Due to the low signal-to-noise of our observations, metal abundances were also fixed at a value of 0.3 solar (Edge & Stewart 1991 [35]). Data with energies below 0.29 keV and above 7.0 keV were excluded from the fits.

Three of the clusters did not posess enough counts to constrain a spectral fit. The results of the six successful fits, combined with best fitting β model parameters from Section 3.4, were then used to estimate the value of R_{2500} for each cluster

Table 3.4. Single Temperature Spectral Fits for R < R_{2500}

Cluster	R_{2500} [h_{70}^{-1} kpc]	kT [keV]	N_H [10^{20} cm^{-2}]	χ^2/DOF
RCS0224-0002	291^{+160}_{-70}	4^{+4}_{-1}	2.91	28.8/51
RCS0439-2904	185^{+302}_{-46}	$2.1^{+5.7}_{-0.8}$	2.63	28.7/75
RCS1107-0523	256^{+155}_{-53}	4^{+4}_{-1}	4.24	12.7/47
RCS1326+2903	139^{+233}_{-45}	$1.3^{+3}_{-0.5}$	1.16	16.7/53
($z = 0.93$)	114^{+223}_{-43}	$1.5^{+3}_{-0.5}$	1.16	16.6/53
RCS1419+5326	336^{+188}_{-67}	4^{+4}_{-2}	1.18	18.9/45
RCS1620+2929	252^{+516}_{-71}	3^{+14}_{-2}	2.72	11.5/33

$$\frac{r_\Delta}{r_c} = \sqrt{\left[\frac{3\beta T}{G\mu m_p (4/3)\pi\rho_c(1+z)^3 r_c^2\Delta}\right] - 1} \tag{3.1}$$

(Ettori 2000 [43]; Ettori et al. 2004 [46]), where $\rho_c = 3H_0^2E_z^2/8\pi G$ and $E_z = H_z/H_0 = \left[\Omega_m(1+z)^3 + \Omega_\Lambda\right]^{1/2}$ for a flat cosmology. Δ is the overdensity (i.e. in determining R_{2500}, $\Delta = 2500$).

After the initial estimation of R_{2500}, additional spectra were extracted from within that radius, and spectral fitting was performed again. If the R_{2500} spectrum could not provide improved constraints on cluster temperature, 2-10 keV luminosities were calculated within R_{2500} from this spectrum with the temperature fixed at its best constrained value. These 2-10 keV luminosities were converted to bolometric luminosities by finding appropriate multiplicative constants using the cluster temperatures and PIMMS. For the three clusters for which spectral fitting was impossible (RCS1417+5305, RCS2112-6326, and RCS2157-0448), count rates were used to determine an upper limit on their luminosities.

The results of this procedure, including values of R_{2500}, and X-ray temperatures are shown in Table 3.4, along with 90% confidence ranges.

Table 3.5. Mass Estimates for R < R_{200}

Cluster	R_{200} [h_{70}^{-1} kpc]	n_0 [10^{-1} cm^{-3}]	M_{gas} [10^{14} h_{70}^{-1} $M_\odot$]	M_{tot} [10^{14} h_{70}^{-1} $M_\odot$]	f_{gas} [h_{70}^{-1}]
RCS0224-0002	1136^{+189}_{-81}	$0.0167^{+0.0005}_{-0.0005}$	$0.12^{+0.02}_{-0.02}$	$4.0^{+0.6}_{-0.6}$	$0.030^{+0.007}_{-0.007}$
RCS0439-2904	712^{+364}_{-56}	$0.026^{+0.001}_{-0.001}$	$0.04^{+0.01}_{-0.01}$	$1.7^{+0.4}_{-0.4}$	$0.024^{+0.008}_{-0.008}$
RCS1107-0523	909^{+201}_{-70}	$0.075^{+0.002}_{-0.002}$	$0.12^{+0.01}_{-0.01}$	$2.0^{+0.3}_{-0.4}$	$0.06^{+0.01}_{-0.01}$
RCS1326+2903	592^{+252}_{-47}	$0.0136^{+0.0005}_{-0.0005}$	$0.03^{+0.009}_{-0.009}$	$0.6^{+0.1}_{-0.2}$	$0.05^{+0.02}_{-0.02}$
($z = 0.93$)	541^{+216}_{-39}	$0.0134^{+0.0005}_{-0.0005}$	$0.03^{+0.009}_{-0.009}$	$0.7^{+0.1}_{-0.1}$	$0.04^{+0.01}_{-0.01}$
RCS1419+5326	1206^{+248}_{-76}	$0.107^{+0.003}_{-0.003}$	$0.20^{+0.03}_{-0.03}$	$4.1^{+0.7}_{-0.6}$	$0.05^{+0.01}_{-0.01}$
RCS1620+2929	913^{+660}_{-90}	$0.040^{+0.001}_{-0.001}$	$0.07^{+0.01}_{-0.01}$	4^{+1}_{-1}	$0.020^{+0.006}_{-0.006}$

3.6 Mass estimates

Using Equations 2.5 and 2.3, along with Equation 3.1, the results of spectral fitting, and best fitting β models, gas masses and total masses were calculated out to R_{200} for the clusters in this sample, and can be found in Table 3.5.

The gas mass fractions of this sample are systematically lower than the expected universal gas fraction (Evrard 1997 [48]). This result is at least somewhat expected given the low temperatures of the clusters (Dell'Antonio et al. 1995 [26]; Sanderson et al. 2003 [106]), and it is also seen in high redshift clusters by the XMM-Newton Ω project (Sadat et al. 2005 [105]). For the objects in our sample that have slightly higher temperatures than poor clusters or groups (RCS 0224-0002 and RCS1419+5326), possible explanations are that the gas in these objects has not yet completely virialized or that some mechanism has injected excess energy into the gas (i.e. galaxy formation, AGN, radio jets), thereby raising its entropy at high z.

3.7 X-ray Scaling Laws

3.7.1 The $L_X - T_X$ Relationship

In the absence of significant preheating and/or cooling, theory predicts that cluster luminosities should scale as $L_{bol} \propto T^2$. However observational studies have resulted in relationships which fall closer to $L_{bol} \propto T^3$ (White, Jones & Forman 1997 [119]; Allen & Fabian 1998 [3]; Markevitch 1998 [87]; Arnaud & Evrard 1999 [9]). There has also been some interest in whether the Lx-Tx relationship evolves with redshift (Ettori et al. 2004 [46]). Departures from theoretically expected self similar scaling laws indicate the effects of non-gravitational processes, such as galaxy formation (Voit 2004 [116]).

The results of the RCS spectral fits, along with the CNOC spectral information from Chapter 2, were used to investigate the Lx-Tx relationship and its evolution. As in Chapter 2, we have adopted a form

$$\left(\frac{L_{2500}}{10^{44}\ \mathrm{erg\ s^{-1}\ E_z}}\right) = C_1\,(\mathrm{kT_{2500}})^{C_2} \tag{3.2}$$

where $E(z) = H(z)/H_0 = \left[\Omega_m(1+z)^3 + \Omega_\Lambda\right]^{1/2}$ for a flat cosmology.

Using the combined data from 20 CNOC and RCS clusters ($0.17 < z < 0.95$), we find the best fitting relationship to be consistent with low redshift Lx-Tx parameterizations ($C_2 = 2.2 \pm 0.2$). If we separate the CNOC ($0.17 < z < 0.55$) from the RCS clusters ($0.64 < z < 0.95$) however, a negative evolutionary trend is indicated, though the data are uncertain enough that both fits remain statistically consistent with no evolution. The scatter in luminosity for these relationships is 0.35 and 0.37 in log space for the total sample and RCS clusters respectively. These are comparable to the scatter of Ettori et al. 2004 [46], who quote a value of $\sigma_L = 0.35$.

Table 3.6 lists the best fitting parameters for each data subset, while Figure 3.3 is a plot of the Lx-Tx data with models overlayed.

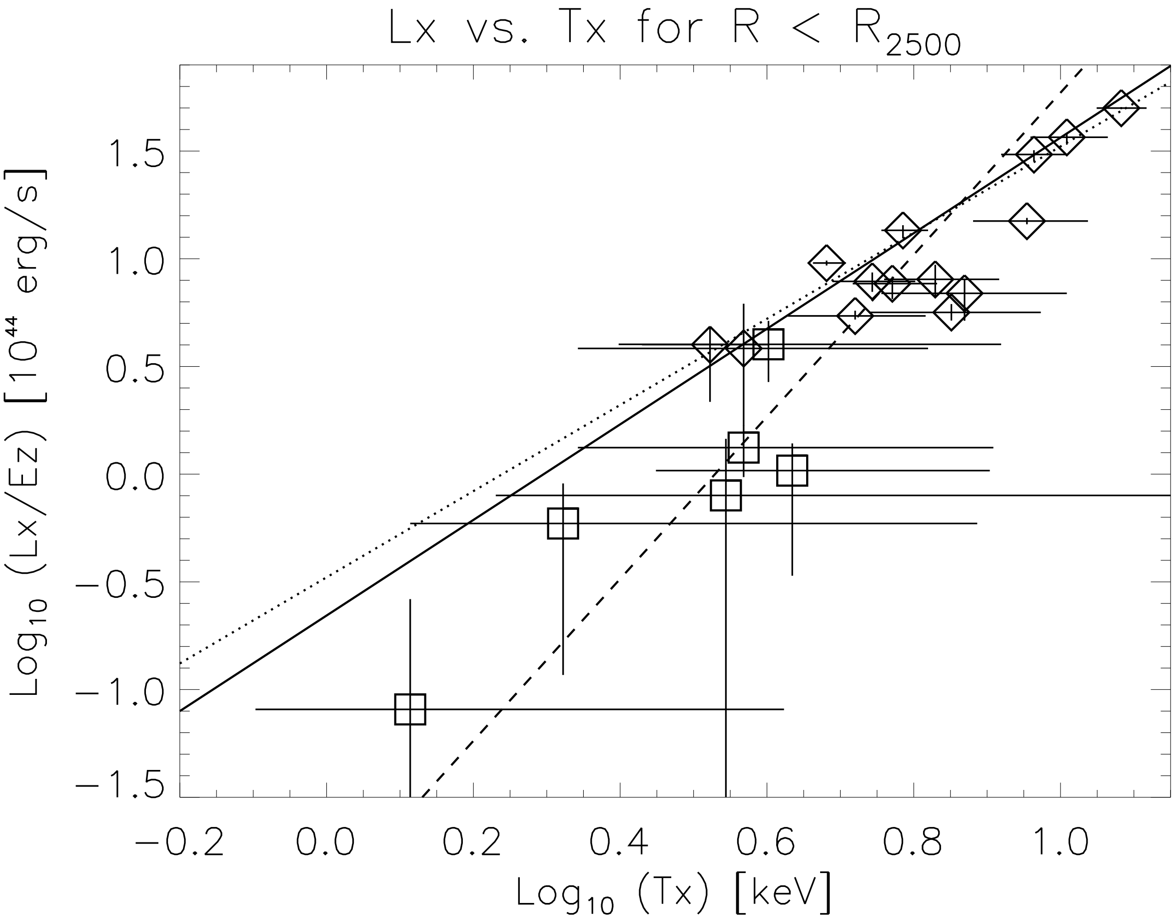

Figure 3.3 X-ray temperatures are plotted against cosmologically corrected unabsorbed bolometric luminosities within R_{2500}. Diamonds designate medium redshift CNOC clusters ($z_{\rm avg} = 0.32$), and squares represent high-z RCS clusters ($z_{\rm avg} = 0.78$). The solid line indicates the best fitting relationship, with a slope of 2.2 ± 0.2 and reduced χ^2 of 1.15. The dotted line denotes the best fit to the data with the powerlaw slope fixed at a value of 2 ± 2, and the dashed line traces the best fitting relationship for only the RCS clusters, and has a slope of 3.8. Error bars indicate 90% confidence limits.

Table 3.6. Best-fit Lx-Tx Parameters

Sample	C_1	C_2	χ^2 (reduced)
CNOC	$0.26^{+0.1}_{-0.08}$	2.1 ± 0.2	1.51
RCS[a]	$0.01^{+0.4}_{-0.01}$	4 ± 2	0.45
	$0.09^{+0.09}_{-0.04}$	2.1	
TOTAL	$0.22^{+0.1}_{-0.07}$	2.2 ± 0.2	1.15
	$0.33^{+0.05}_{-0.04}$	2	

[a]68% confidence

3.7.2 The Mass$-T_X$ Relationship

A linear least-squares fit was also performed between cluster temperatures and mass estimates for these two samples. This relationship takes the form:

$$(E_z M_{tot}) = C_1 \,(\mathrm{kT})^{C_2} \tag{3.3}$$

(Ettori et al. 2004 [46]).

The best fitting values for the combined sample were $C_1 = 8^{+4}_{-3} \times 10^{1}3$ and $C_2 = 1.5 \pm 0.2$, a slope which is consistent with expected values. The scatter in mass (in log space) for these relationships is 0.11 for the total sample and 0.14 for the RCS clusters, which are lower than but comparable to the scatter found by Ettori et al. 2004 [46] ($\sigma_Y = 0.15$). Table 3.7 lists the best fitting parameters for each data subset, while Figure 3.4 is a plot of the Mass-Tx data with models overlayed.

3.8 Optical Richness

Optical richness is effectively a measurement of galaxy overdensity within a given aperture, normalized for the evolving galaxy luminosity function and the expected spatial distribution of galaxies in the cluster. More specifically, B_{gc} (Yee & Lopez-Cruz

Table 3.7. Best-fit Mass-Tx Parameters

Sample	C_1 $[10^{13}]$	C_2	χ^2 (reduced)
CNOC	8^{+4}_{-3}	1.5 ± 0.2	1.58
RCS[a]	$4.5^{+1}_{-0.3}$	1.8 ± 0.8	0.44
TOTAL	8^{+4}_{-3}	1.5 ± 0.2	1.1

[a]68% confidence

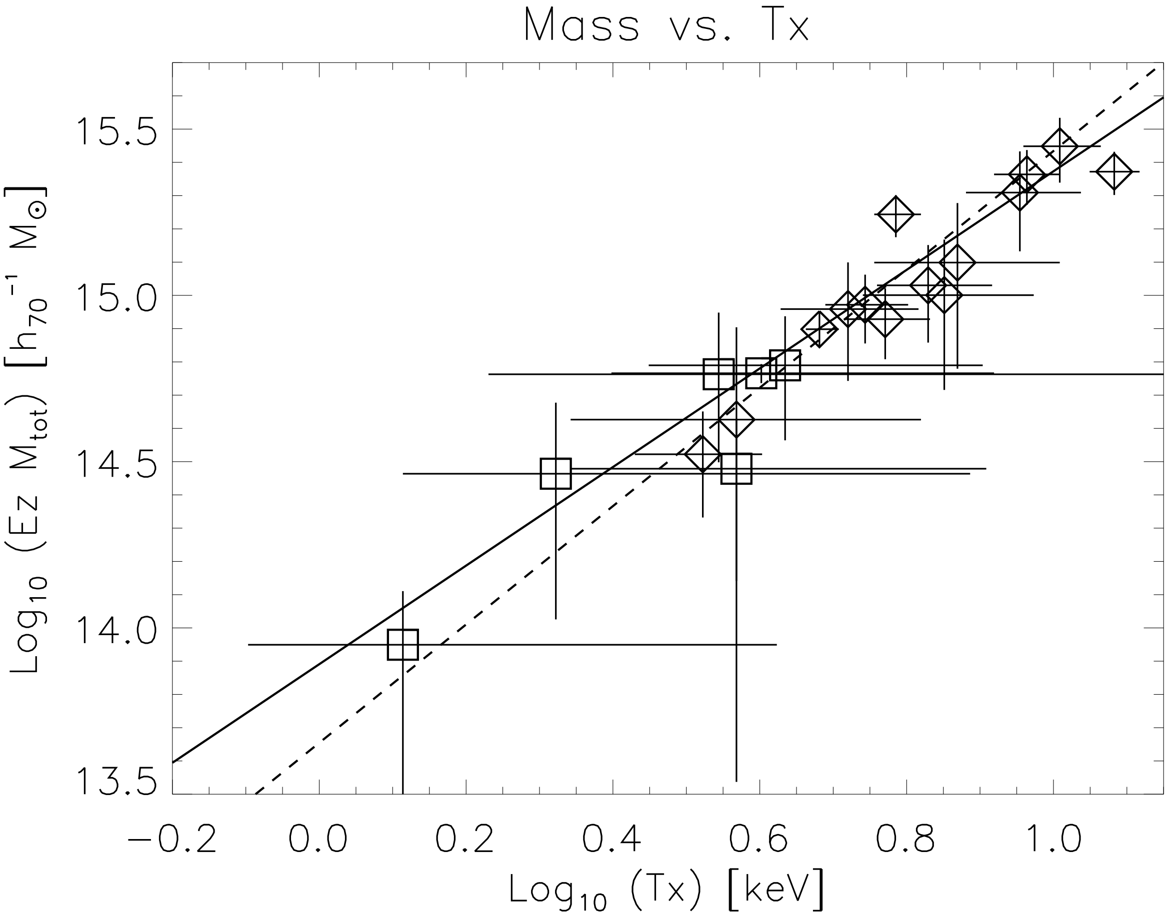

Figure 3.4 X-ray temperatures are plotted against corrected mass estimates from Section 3.6. Diamonds designate medium redshift CNOC clusters ($z_{\rm avg} = 0.32$), and squares represent high-z RCS clusters ($z_{\rm avg} = 0.78$). The solid line indicates the best fitting relationship, with a slope of 1.5 ± 0.2 and reduced χ^2 of 0.55. The dashed line traces the best fitting relationship for only the RCS clusters. Error bars indicate 90% confidence limits.

(1999) [124]), represents the galaxy-cluster spatial covariance amplitude (as described in Section 1.3.4.4).

Large uncertainties exist in the evolution of cluster galaxies at redshifts of $z > 0.5$, These uncertainties can be minimized by employing a red-sequence optical richness, $B_{gc,red}$, which is calculated using only the more slowly evolving red galaxies in a cluster. This is the optical richness parameter which will be used throughout this work. Values of $B_{gc,red}$ for this sample are given in Table 3.8 (H.K.C. Yee 2005, private communication).

It has been shown that B_{gc} correlates well with the X-ray parameters of relaxed clusters (Yee & Ellingson 2003 [125]), and in Section 2.9 we have derived relationships for correlations of X-ray properties with $B_{gc,red}$. These relationships were calibrated for X-ray selected clusters at moderate redshift, and therefore may not accurately describe our current sample. Here we compare and attempt to recalibrate these correlations for optically selected clusters at high redshift.

As in Section 2.9, our current data are not sufficient to simultaneously constrain the intercept and powerlaw slope of these relationships. Therefore we once again take $\gamma = 1.77$, and adopt the simple form

$$\mathrm{X} = \mathrm{C_1} \times \mathrm{B_{gc,red}}^{\mathrm{C_2}} \tag{3.4}$$

where X represents the particular property being fit. For T_X, $\mathrm{M_{200}}$, $\mathrm{R_{200}}$, and L_X/E_z, units of keV, $\mathrm{M_\odot}$, Mpc, and 10^{44}erg s^{-1} were used, respectively. RCS0439-2904 was removed from fitting procedures due to spectroscopic indications (D. Gilbank 2005, private communication) that it does not consist of a single virialized mass but 2-3 closely spaced groups of galaxies in projection along the line of sight, which has the effect of artificially driving up its measured value of $\mathrm{B_{gc,red}}$.

The data, with the results of these fits overlaid, are shown in Figures 3.5, 3.7, 3.9, and 3.11. Histograms indicating the scatter in predicted cluster properties are shown

Table 3.8. Cluster Richness and Luminosity

Cluster	L_x[a] $[10^{44}$ erg s$^{-1}]$	Bgc_{red} [Mpc$^{1.77}$]
RCS0224-0002	$1.6^{+0.2}_{-0.4}$	802 ± 184
RCS0439-2904	$1.0^{+0.2}_{-0.3}$	2231 ± 654
RCS1107-0523	$2.0^{+0.2}_{-0.2}$	933 ± 297
RCS1326+2903	$0.13^{+0.2}_{-0.2}$	435 ± 164
($z = 0.93$)	$0.3^{+0.2}_{-0.2}$	1600 ± 354
RCS1417+5305	< 0.24[b]	1879 ± 464
RCS1419+5326	$5.7^{+0.6}_{-0.7}$	1273 ± 221
RCS1620+2929	$1.3^{+0.4}_{-0.5}$	729 ± 187
RCS2112-6326	< 0.38[b]	1011 ± 400
RCS2157-0448	< 0.23[b]	481 ± 166

[a]Unabsorbed bolometric X-ray luminosity within R_{2500}

[b]Upper limit within 300 h_{70}^{-1} kpc, assuming a temperature of 5 keV

Table 3.9. Fitting Parameters

Relationship	C_1	C_2
$T_X - B_{gc,red}$	$2.3^{+0.3}_{-0.3} \times 10^{-3}$	1.13
$\mathrm{R}_{200} - \mathrm{B}_{\mathrm{gc,red}}$	$3.5^{+0.2}_{-0.2} \times 10^{-2}$	0.56
$E_z{}^{-1} L_X - B_{gc,red}$	$2.4^{+0.7}_{-0.5} \times 10^{-7}$	2.49
$E_z \mathrm{M}_{200} - B_{gc,red}$	$6^{+1}_{-1} \times 10^{9}$	1.69

in Figures 3.6, 3.8, 3.10, and 3.12. Best fitting parameters are given in Table 3.9.

Clear trends are seen in the $T_X - \mathrm{B}_{\mathrm{gc,red}}$ and Mass-$\mathrm{B}_{\mathrm{gc,red}}$ relationships, however there is significant scatter in both (45% and 86%, respectively). $\mathrm{B}_{\mathrm{gc,red}}$ is not well correlated to R_{200}, and is particularly poorly related to X-ray luminosity. This result seems to indicate that (in the absence of errors due to projection) $\mathrm{B}_{\mathrm{gc,red}}$ traces total mass rather than gas mass, since X-ray luminosity strongly depends upon gas density. RCS0439-2904, RCS2112-6326, and RCS1417+5305 are substantially less luminous than their richnesses would indicate, suggesting that superpositions of structure along the line of sight remain a sizeable concern in optically selected cluster samples.

3.8.1 The Redshift Evolution of $\mathrm{B}_{\mathrm{gc,red}}$ as a Mass Indicator

To investigate the redshift dependence of optical richness as a mass indicator, we have taken the combined CNOC and RCS samples for which we have temperature information (excluding RCS0439-2904) and split them into four redshift bins from $0.1 < z < 0.9$ with a binsize of 0.2. We expect cluster mass to scale as both $T^{3/2}$ and $\mathrm{B}^{1.69}_{\mathrm{gc,red}}$, therefore a ratio of these two quantities plotted vs. redshift should be constant if there is no systematic trend with redshift in the estimation of $\mathrm{B}_{\mathrm{gc,red}}$. Figure 3.13 shows that there is in fact a propensity for $\mathrm{B}_{\mathrm{gc,red}}$ to overestimate cluster mass at high redshift, and that the magnitude of this effect increases with redshift, reaching a factor of ~ 1.4 by $z \sim 0.8$.

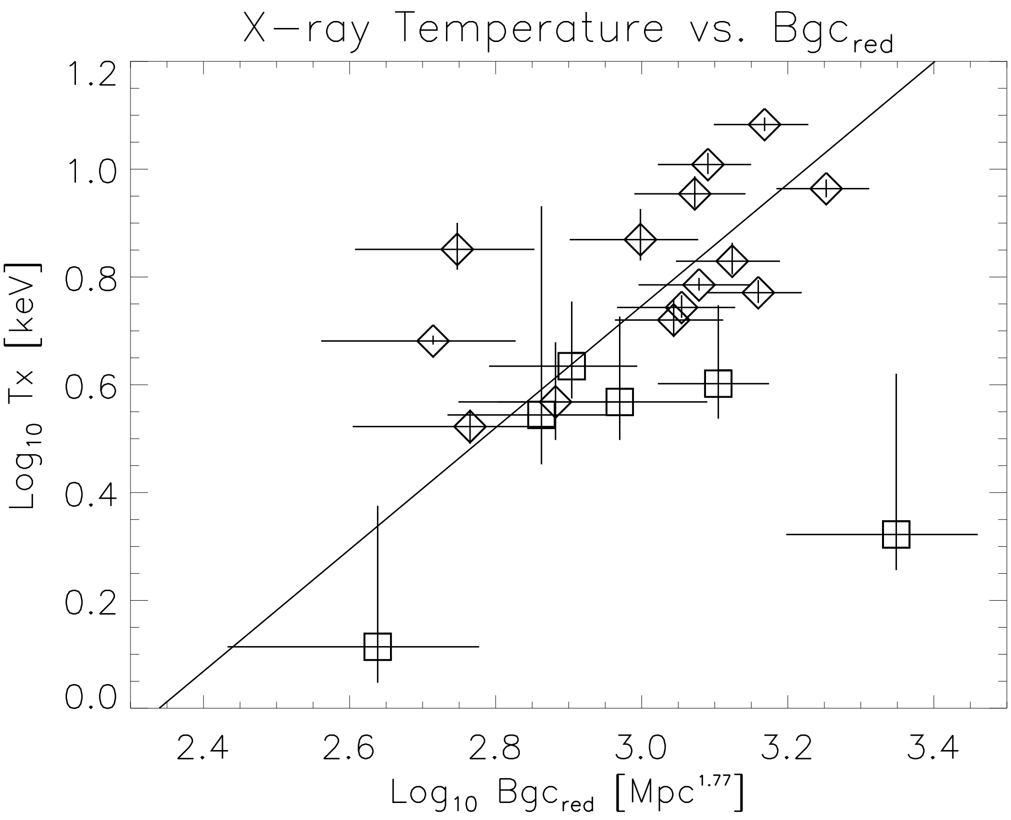

Figure 3.5 A log-log plot of T_X vs. $B_{gc,red}$ for the combined CNOC and RCS samples. Error bars represent 68% confidence intervals. CNOC clusters are shown as diamonds, and squares designate the RCS sample. The solid line indicates the best fitting relationship between these two parameters given $\gamma = 1.77$ (Section 3.8). The most obvious outlying point represents RCS0439-2904, which is known to consist of several (2-3) closely spaced groups of galaxies in projection along the line of sight (D. Gilbank 2005, private communication).

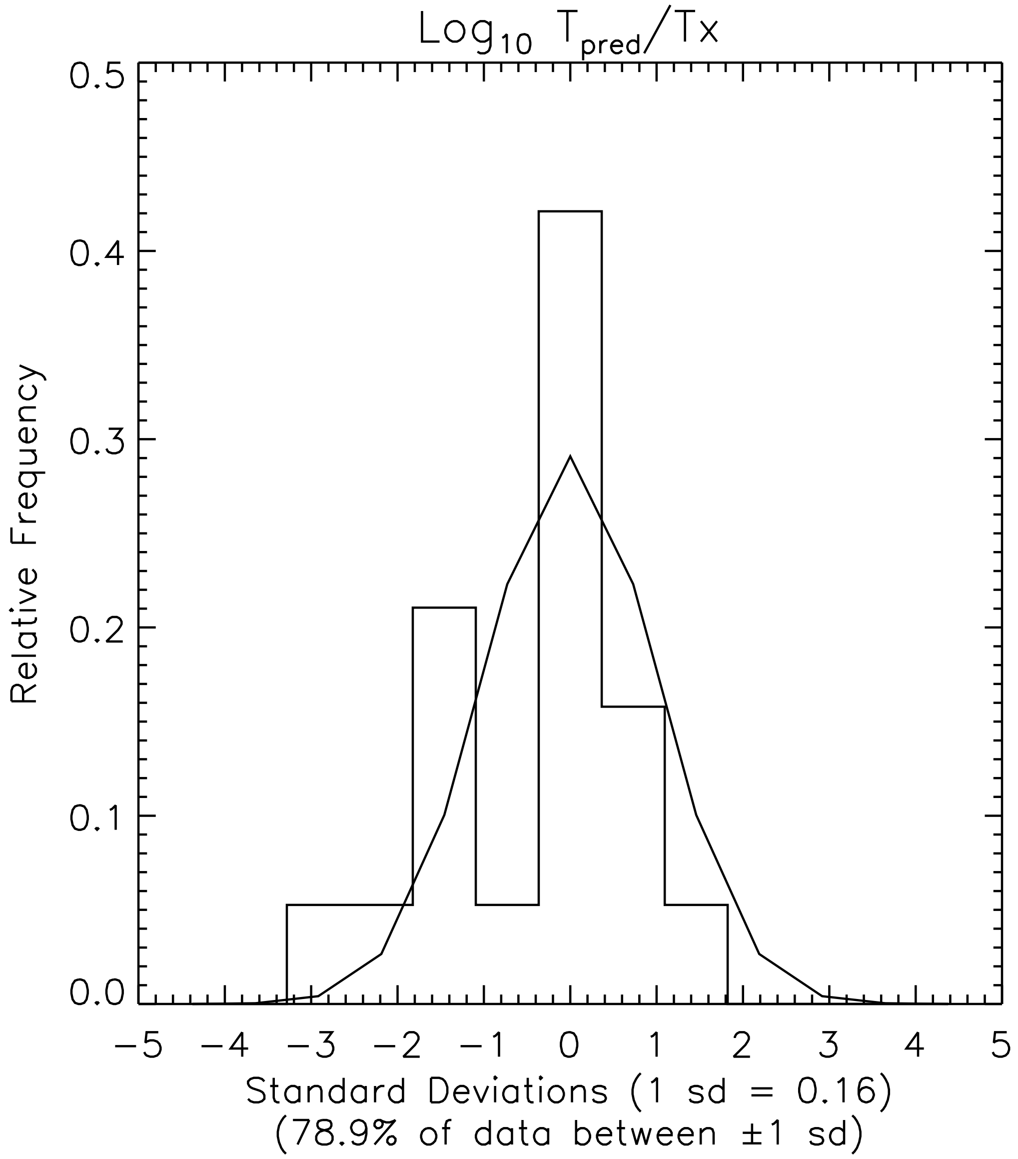

Figure 3.6 Relative frequency histogram of the log of the ratio between B_{gc} predicted temperature and measured temperature, with a normal curve overlaid. X-axis units are in standard deviations. One standard deviation represents a change in ratio of 0.45, with zero indicating a mean ratio of 1.0.

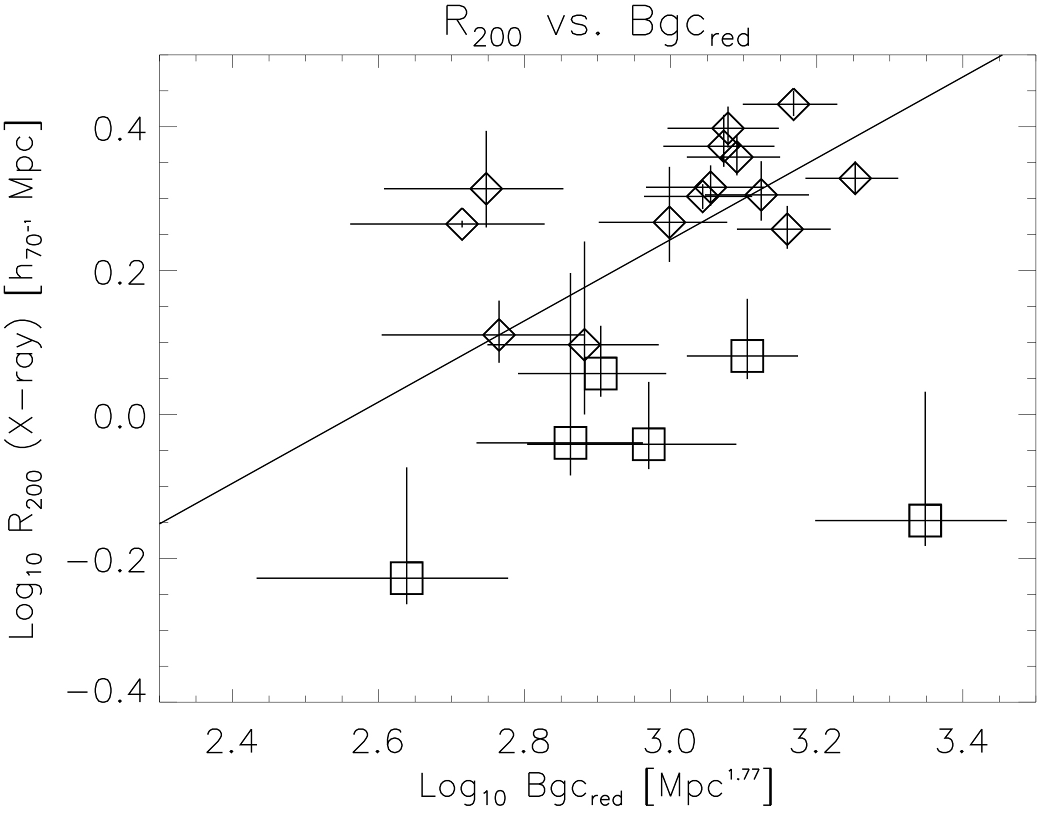

Figure 3.7 A log-log plot of R_{200} vs. $B_{gc,red}$ for the combined CNOC and RCS samples. Error bars represent 68% confidence intervals. CNOC clusters are shown as diamonds, and squares designate the RCS sample. The solid line indicates the best fitting relationship between these two parameters given $\gamma = 1.77$ (Section 3.8). The most obvious outlying point represents RCS0439-2904, which is known to consist of several (2-3) closely spaced groups of galaxies in projection along the line of sight (D. Gilbank 2005, private communication).

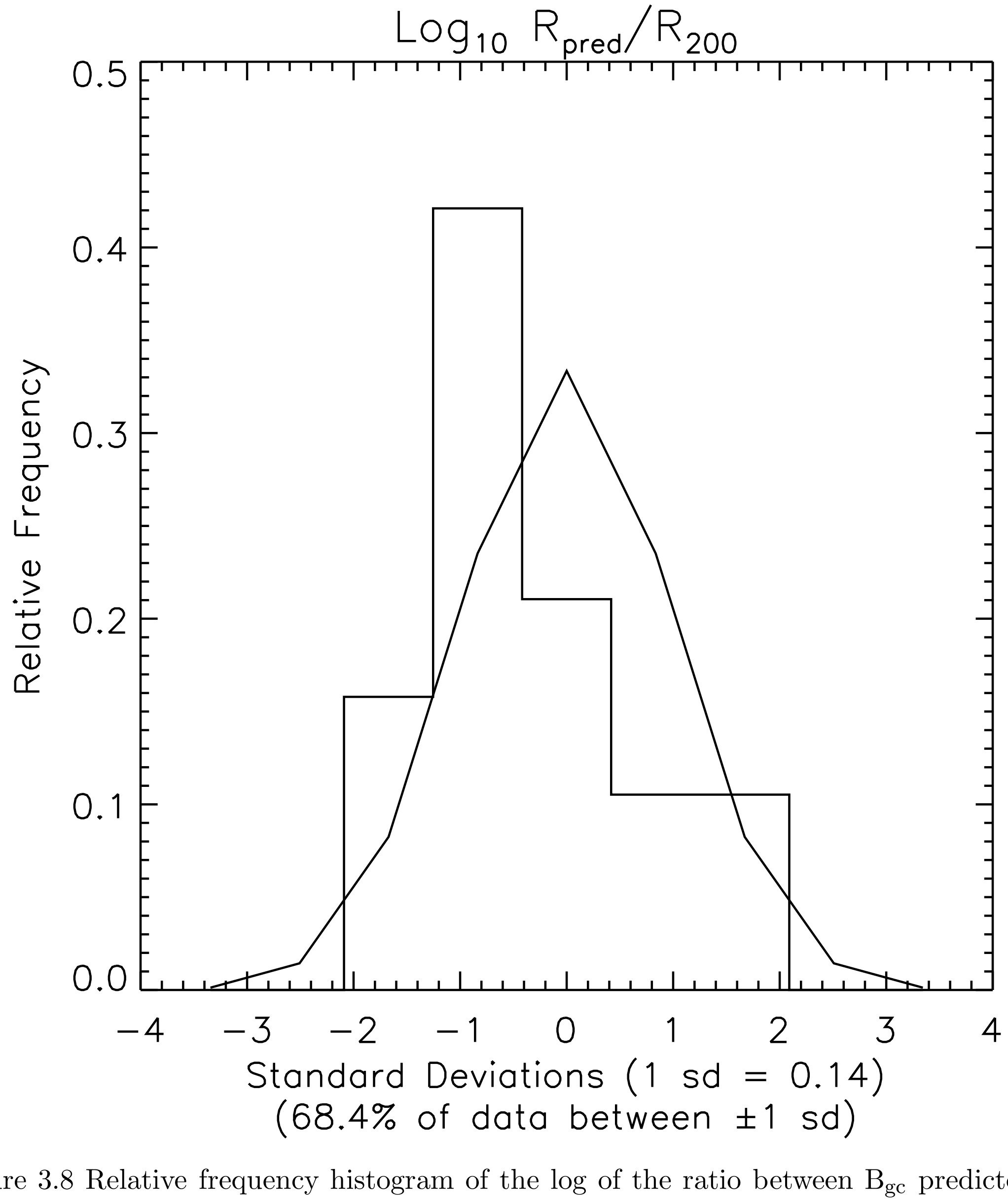

Figure 3.8 Relative frequency histogram of the log of the ratio between B_{gc} predicted R_{200} and X-ray predicted R_{200}, with a normal curve overlaid. X-axis units are in standard deviations. One standard deviation represents a change in ratio of 0.38, with zero indicating a mean ratio of 1.06.

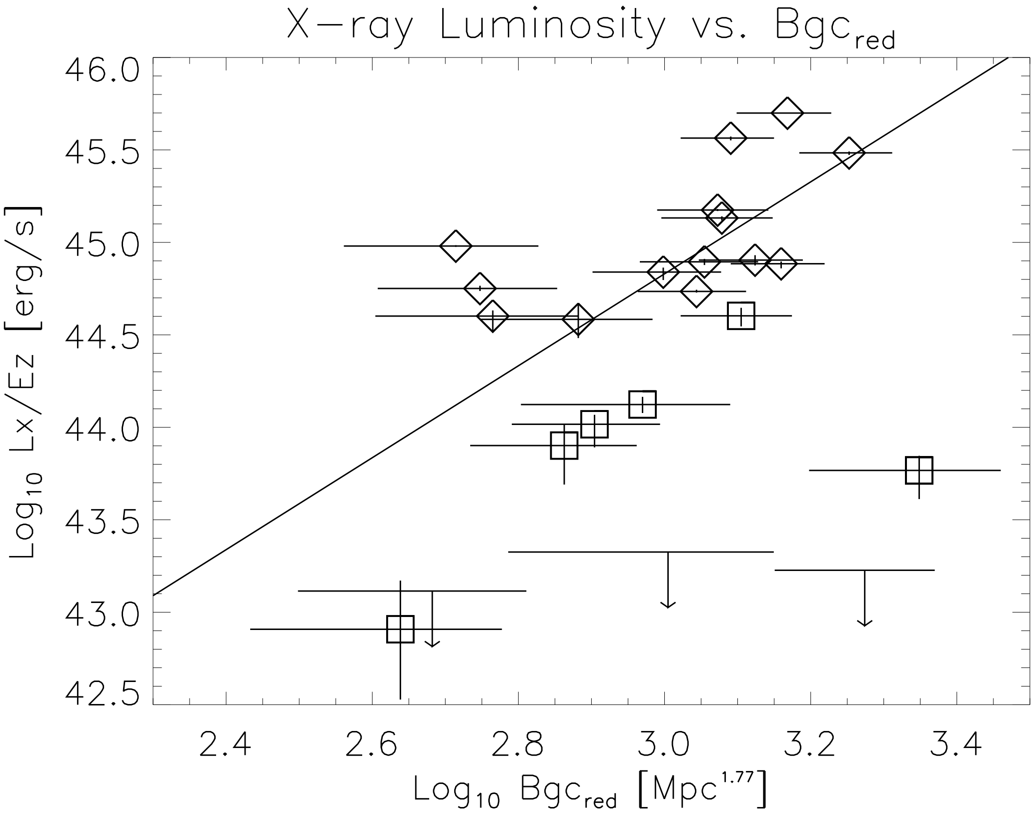

Figure 3.9 A log-log plot of L_X vs. $B_{gc,red}$ for the combined CNOC/RCS sample. CNOC clusters are shown as diamonds, and squares designate the RCS sample. Error bars represent 68% confidence intervals. The solid line indicates the best fitting relationship between these two parameters given $\gamma = 1.77$ (Section 3.8) and $L_X \sim T_X{}^{2.2}$ (Section 3.7.1). The square symbol farthest to the right represents RCS0439-2904, which is known to consist of several (2-3) closely spaced groups of galaxies in projection along the line of sight (D. Gilbank 2005, private communication). The lines with arrows designate an upper limit to the luminosities of (left to right) RCS2157-0448, RCS2112-6326, and RCS1417+5305.

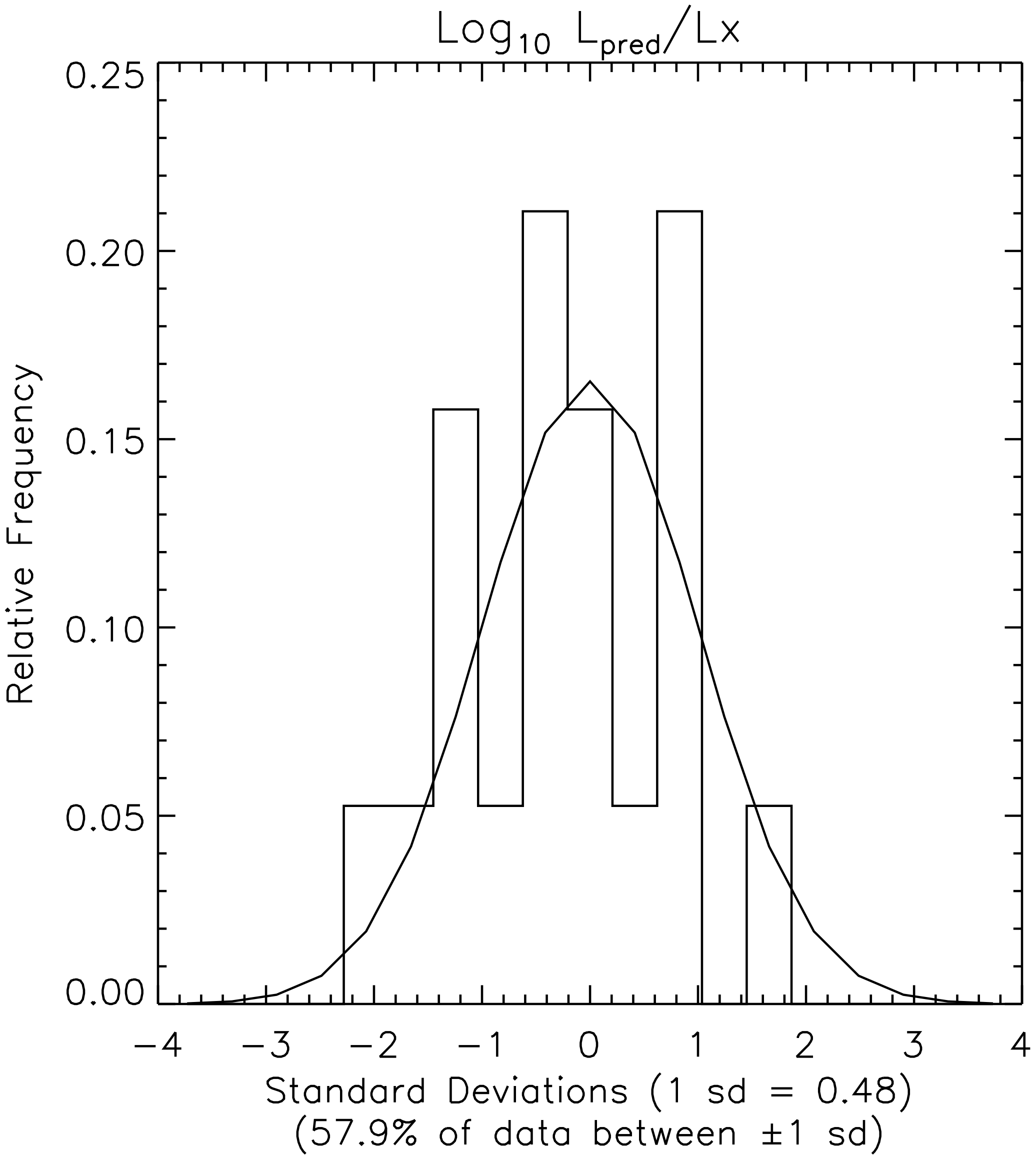

Figure 3.10 Relative frequency histogram of the log of the ratio between B_{gc} predicted L_X and measured L_X, with a normal curve overlaid. X-axis units are in standard deviations. One standard deviation represents a factor of 3 difference between predicted and measured L_X, with zero indicating a mean ratio of 1.14.

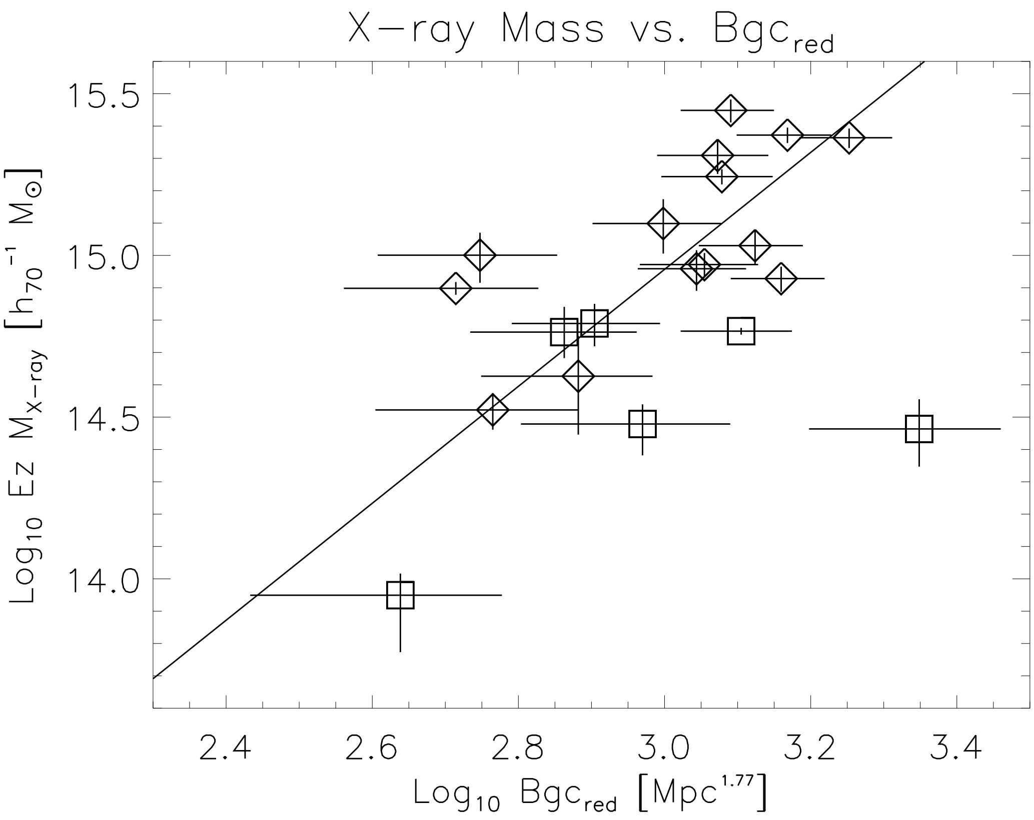

Figure 3.11 A log-log plot of X-ray mass estimates vs. $B_{gc,red}$ for the combined CNOC/RCS sample. Error bars represent 68% confidence intervals. CNOC clusters are shown as diamonds, and squares designate the RCS sample. The solid line indicates the best fitting relationship between these two parameters given $\gamma = 1.77$ (Section 3.8) and Mass$\sim T_X{}^{1.5}$ (Section 3.7.2). The most obvious outlying point represents RCS0439-2904, which is known to consist of several (2-3) closely spaced groups of galaxies in projection along the line of sight (D. Gilbank 2005, private communication).

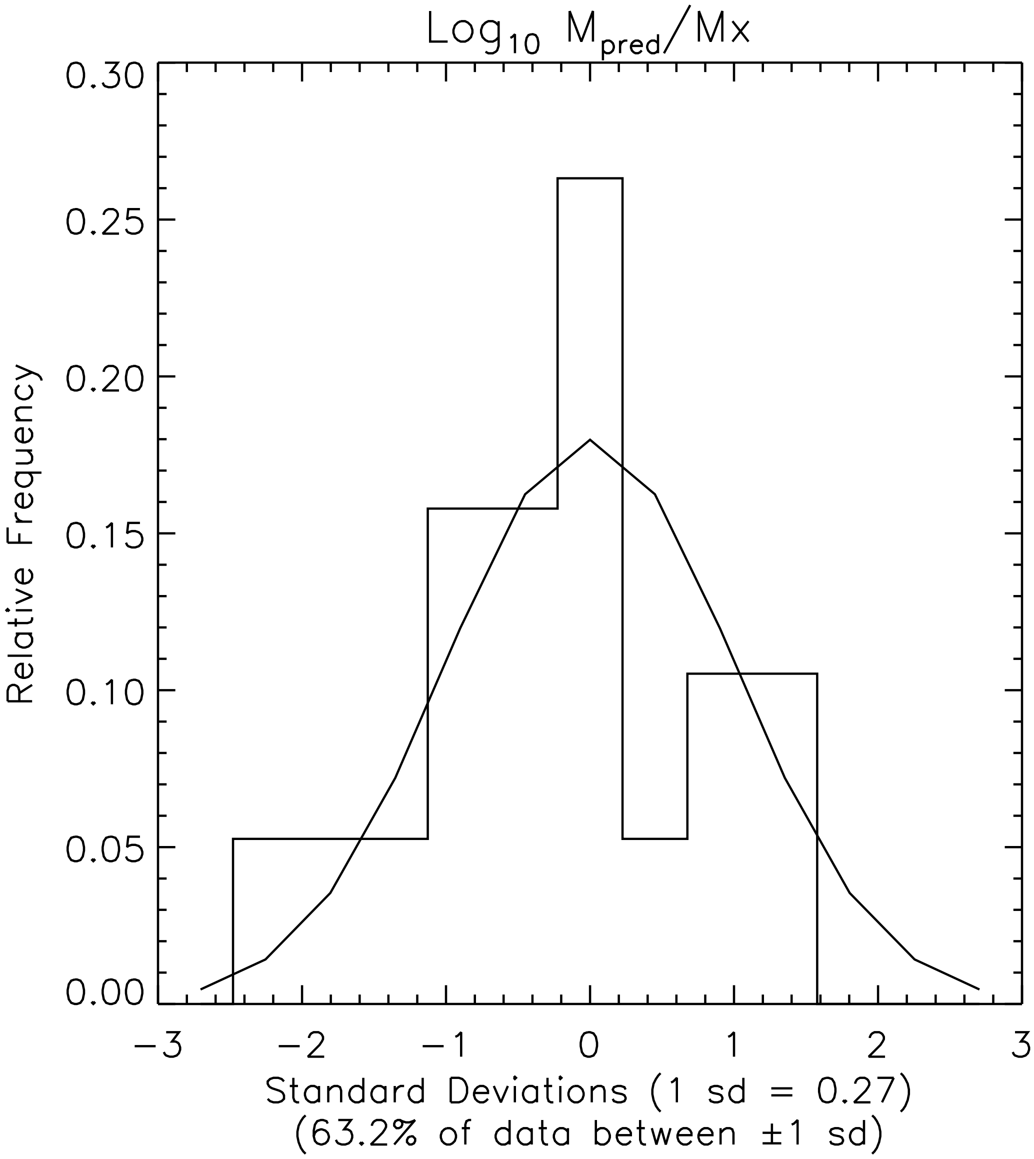

Figure 3.12 Relative frequency histogram of the log of the ratio between B_{gc} predicted mass and X-ray mass estimates, with a normal curve overlaid. X-axis units are in standard deviations. One standard deviation represents a change in ratio of 0.86, with zero indicating a mean ratio of 1.0.

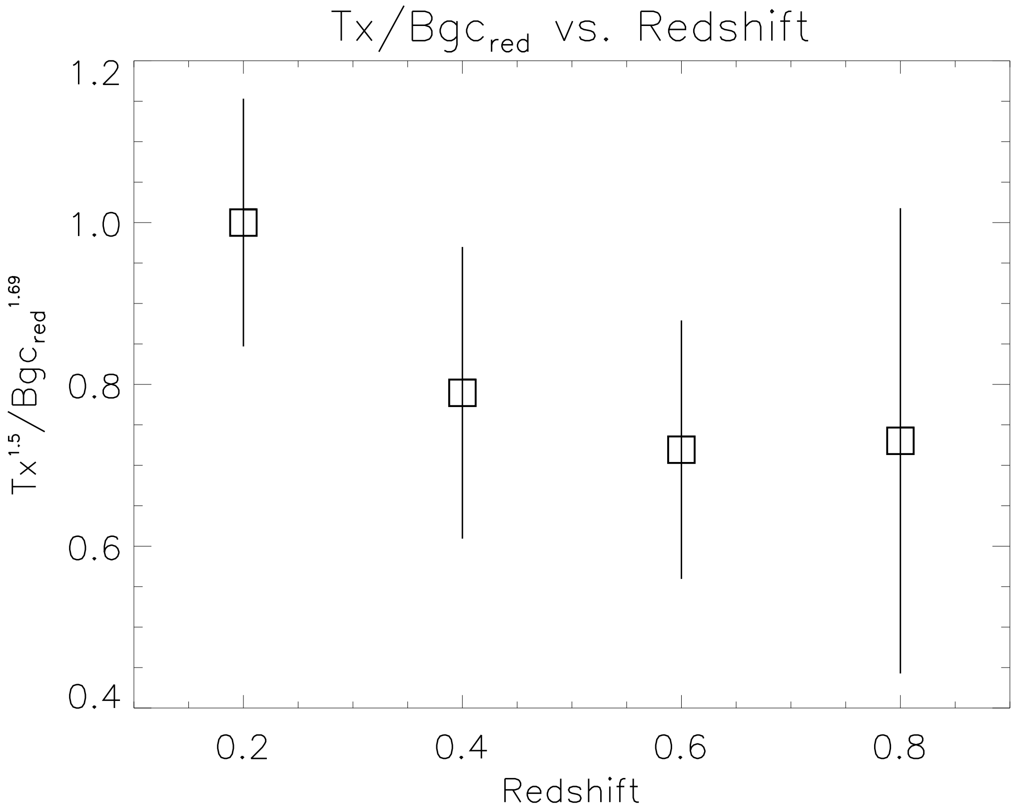

Figure 3.13 A total of 19 CNOC/RCS clusters were divided into 4 redshift bins spanning the range $0.1 < z < 0.9$. For each bin, the weighted average quantity $T_X^{1.5}/\mathrm{B}_{\mathrm{gc,red}}^{1.69}$ is plotted vs. the central redshift of each bin. The value of the first bin was normalized to 1. A clear trend is seen in this quantity with redshift, indicating that optical richness is prone to the overestimation of cluster mass at high redshift, and that the magnitude of this effect increases with redshift, reaching a factor of ~ 1.4 by $z \sim 0.8$.

Most likely this effect is due to the fact that dark matter density profiles are more concentrated in clusters which have formed at high redshifts, reflecting the high density of the universe at the epoch of their formation (Hiotelis 2003 [75]; Del Popolo 2001 [99]). If light follows mass, the distribution of galaxies would also have a higher central concentration in such objects, leading to systematically higher optical richness measurements. In theory this effect could be observationally corrected for, however, based on the large errors in Figure 3.13, it is clear that additional data are required to robustly calibrate relationships between optical richness and mass over a broad range in redshift.

3.9 Summary and Discussion

We have performed the first in-depth X-ray investigation of nine high redshift ($0.64 < z < 1.1$) optically selected clusters of galaxies from the Red-sequence Cluster Survey (RCS). Each of these clusters was detected by Chandra at a (photon counts) significance of greater than 2σ, however three of the clusters in our sample (RCS1417+5305, RCS2112-6326, and RCS2157-0448) did not posess enough signal to support further analysis.

Surface brightness profiles were extracted for the six remaining clusters (RCS0224-0002, RCS0439-2904, RCS1107-0523, RCS1326+2903, RCS1419+5326 and RCS1620+2929) in $1-2''$ annular bins (Figure 2.2), and fit with single β models. We note that values of β for this sample seem to run systematically low ($\beta < 0.61$), possibly implying that the gas in these clusters is less centrally concentrated than lower redshift X-ray selected samples. This finding, however, is inconclusive due to a degeneracy between R_{core} and β, and would require longer observations (i.e. higher S/N) to break the degeneracy. We note that the low gas fractions of this sample provide additional support for this idea.

The six higher signal clusters were also spectrally analyzed in XSPEC, beginning with an extraction region of 300 kpc radius. The results of single temperature spectral fits, combined with the outcomes of surface brightness fitting (above) were then used to determine R_{2500}. Spectra were re-extracted from regions of that radius for further temperature fitting and R_{2500} luminosity estimates. The temperatures of these clusters are not, in general, particularly well constrained (90% errors of 0.5-14 keV), but they also appear systematically lower than those of X-ray selected samples ($T_X(\mathrm{RCS}) = 1.3 - 4.3$ keV).

Using the results of both spectral fitting and surface brightness modeling, X-ray masses were calculated out to R_{200} for six clusters in our sample. The most noticeable outcome of this procedure is that the gas mass fractions of RCS clusters are considerably lower than expected. This result is not surprising for clusters with temperatures below ~ 4 keV (Dell'Antonio et al. 1995 [26]; Sanderson et al. 2003 [106]), and it is also supported by the findings of other high redshift cluster studies (Sadat et al. 2005 [105]). For clusters in our sample that have fitted temperatures of 4 keV or higher (RCS 0224-0002 and RCS1419+5326), we infer that either the gas in these objects has not yet completely virialized, or that some mechanism (i.e. galaxy formation, AGN, radio jets) is responsible for raising the entropy of the gas.

X-ray scaling laws were investigated for these clusters and compared to those of the medium redshift ($0.1709 < z < 0.5466$) CNOC sample (Section 2.8). In both $L_X - T_X$ and Mass-T_X relationships RCS clusters are best fit with steeper slopes than those of the CNOC sample, however both slopes are consistent (within 68% confidence) with the theoretically expected values of 2 and 1.5, respectively. Steeper slopes in these relationships indicate the effects of non-gravitational processes, most likely due to galaxy formation (Voit 2004 [116]). The best fitting $L_X - T_X$ relationship for the combined CNOC-RCS sample has an intercept of $0.22^{+0.1}_{-0.07}$ and a slope of 2.2 ± 0.2. The best fitting Mass-T_X relationship for the combined sample of 20 clusters has an intercept of $8^{+4}_{-3} \times 10^{13}$ and a slope of 1.5 ± 0.2.

Using the best fitting scaling laws for the combined CNOC-RCS sample, and equations 3 and 4 in Yee & Ellingson (2003) [125], the relationships between red-sequence optical richness ($B_{gc,red}$) and global cluster properties (T_X, R_{200}, L_X and M_{200}) were investigated. For fitting purposes, γ was fixed at a fiducial value of 1.77. RCS0439-2904 was removed from the fitting procedure based on optical spectroscopy which indicates that it is not a single cluster but rather a superposition of smaller groups in very close proximity along the line of sight (D. Gilbank 2005, private communication). For the remaining five RCS clusters we find that $B_{gc,red}$ is a reasonable estimator of T_X and M_{200}, but is not as well correlated to R_{200} and is a particularly poor estimator of X-ray luminosity. This may be due to $B_{gc,red}$ being a sufficient tracer of total mass, but not gas mass, since X-ray luminosity strongly depends upon gas density. This explanation is in keeping with the low gas mass fractions that we find for this sample.

Significant redshift evolution is detected in the mass predictions of $B_{gc,red}$, culminating in overestimation of cluster mass by a factor of ~ 1.4 at a redshift of $z \sim 0.8$ (Figure 3.13). This could be due to high redshift clusters having more centrally concentrated dark matter density profiles that subsequently drive up optical richness measurements. A robust calibration of this effect could place optical richness firmly in our arsenal of reliable mass estimators, however this will require both a larger sample and (in the case of the RCS clusters) deeper X-ray observations.

Chapter 4

X-ray Analysis of the High Redshift Lensing Cluster RCS0224-0002

4.1 Introduction

Clusters of galaxies which exhibit gravitational lensing have been actively sought since their discovery in the mid-1980s (Soucail et al. 1988 [40]; Lynds & Petrosian 1988 [86]). This interest is due to the numerous scientific opportunities that these objects provide. Because they magnify sources which lie at very high redshifts, they allow us to investigate the early universe in great detail (e.g., Ebbels et al. 1996 [33]; Franx et al. 1997 [52]). Gravitational lensing can also be used as an independent probe of the mass distribution of clusters (e.g., Kneib et al. 1993 [81]; Tyson, Kochanski, & dell'Antonio 1998 [113]). In addition, clusters with multiple lensed sources contain information on the underlying cosmology of the universe (Golse, Kneib, & Soucail 2001 [65]). Until recently the cumulative sample of strong lensing clusters was relatively small and mainly restricted to objects at redshifts of $z < 0.5$ (Wu et al. 1998 [123]; Williams, Navarro, & Bartelmann 1999 [122]).

The Red-sequence Cluster Survey (RCS; Gladders & Yee 2000, 2005 [62, 63]) has recently discovered a sizeable number of strong lensing clusters at high redshift (Gladders et al. 2003 [61]). The incidence of strong lensing found in the RCS sample is significantly higher than that predicted by current cosmological theory. Gladders et al. (2003) [61] investigates this phenomenon in detail and provides possible explanations for it, which include the effects of substructure, ellipticity, concentrated mass profiles, and projection.

This work presents the first opportunity to examine these possibilities in detail in the X-ray band. One of the most striking objects discovered via the RCS survey is RCS0224-0002 at $z = 0.773$ (Gladders, Yee, & Ellinson 2002 [64]). This cluster possesses a rich array of lensing arcs that originate from two to four background sources, one of which lies at a (spectrally confirmed) redshift of $z = 4.88$

RCS0224-0002 was recently observed with the Chandra X-ray Observatory for 89 kiloseconds, the deepest X-ray follow-up observation of an RCS cluster to date. Here we present our analysis of this observation. From the data we derive a spatially resolved surface brightness profile, cluster temperature, and mass. In addition, we compare high resolution X-ray flux and hardness images of the cluster core with observations in the optical and radio. We discuss implications of our results which may be pertinent to the high incidence of lensing found in the RCS sample. A point source analysis of this field is also presented.

4.2 Observations and Data Reduction

RCS0224-0002 was observed by the Chandra X-ray Observatory on 9 December 2004 for 89,204 seconds. The aimpoint of the observation was located on the S3 chip of the Advanced CCD Imaging Spectrometer (ACIS) CCD array. Upon obtaining the data, aspect solutions were examined for irregularities and none were detected. Charged particle background contamination was reduced by excising time intervals during which the background count rate exceeded the average background rate by more than 20%. Bad pixels were removed from the resulting event files, and they were also filtered on standard grades. After cleaning, the available exposure time was 88,951 seconds.

0.29-7.0 keV images, instrument maps and exposure maps were created using the CIAO tools DMCOPY and MERGE_ALL, binning the data by a factor of 2. Data with energies above 7.0 keV and below 0.29 keV were excluded due to background contamination and uncertainties in the ACIS calibration, respectively. Data between 0.29 keV and 0.6 keV were included despite questionable low energy calibration for the purpose of increasing the overall signal to noise of the observation.

Flux images were created by dividing the image by the exposure map, and initial point source detection was performed by running the tools WTRANSFORM and WRECON on the 0.29-7.0 keV image. An adaptively smoothed flux image was created with CSMOOTH. This smoothed image was used to determine the X-ray centroid of the cluster, which lies at an RA, Dec of 02:24:34.195, -00:02:29.92 (J2000). Figure 4.1 shows an HST image of RCS0224-0002 with adaptively smoothed X-ray flux contours overlayed.

4.3 Spectral Analysis

Using the centroid position indicated in Section 4.2, a spectrum was extracted from a point source removed event file in a circular region with a 300 h_{70}^{-1} kpc ($\sim R_{2500}$) radius (Chapter 3). This spectrum was then analyzed in XSPEC (Arnaud 1996 [8]), using a weighted response matrix (RMF) and effective area file (ARF) generated with the CIAO tool ACISSPEC and the most recent version of the Chandra calibration database (CALDB 3.0.1). A 100 pixel radius circular background was extracted from the aimpoint chip as far away from the cluster as possible. The spectrum was then grouped to include at least 20 counts per bin.

The spectrum was fit with a single temperature spectral model including foreground absorption. The absorbing column was fixed at its measured value of $2.91 \times 10^{20} \mathrm{cm}^{-2}$ (Dickey & Lockman 1990 [28]), and the metal abundance was fixed at 0.3 solar. Data with energies below 0.29 keV and above 7.0 keV were excluded from the fit. The best fit temperature of the cluster was $T_x = 4.3^{+3.7}_{-1.5}$ keV. Figure 4.2 is a plot of the spectrum of RCS0224-0002 with the best fitting model overlaid on the data.

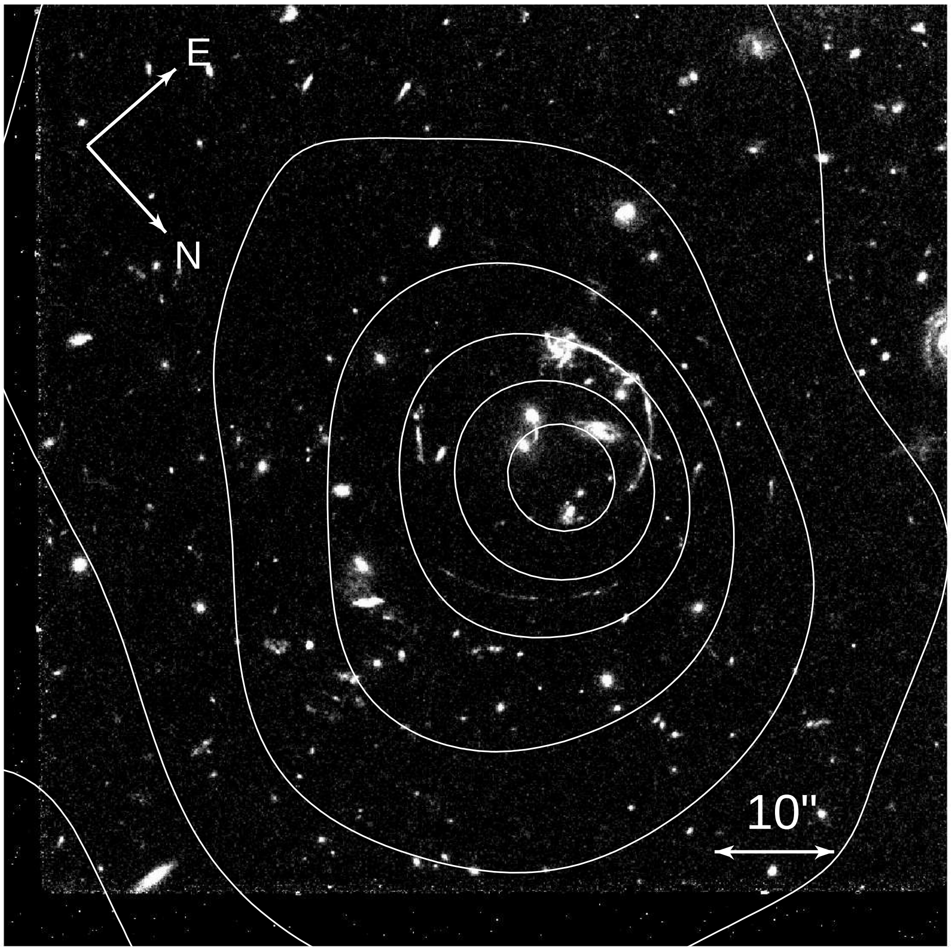

Figure 4.1 logarithmic X-ray contours are overlaid on an 1100s HST image of RCS0224-0002 taken with the F606W filter. X-ray countours were created from an adaptively smoothed Chandra 0.29-7.0 keV flux image, and have values between 1.25 and 0.3 $\times 10^{-8}$ counts sec^{-1} cm^{-2} arcsec^{-2}. Note that the location of the X-ray centroid is not in line with the center of the gravitational lensing arcs.

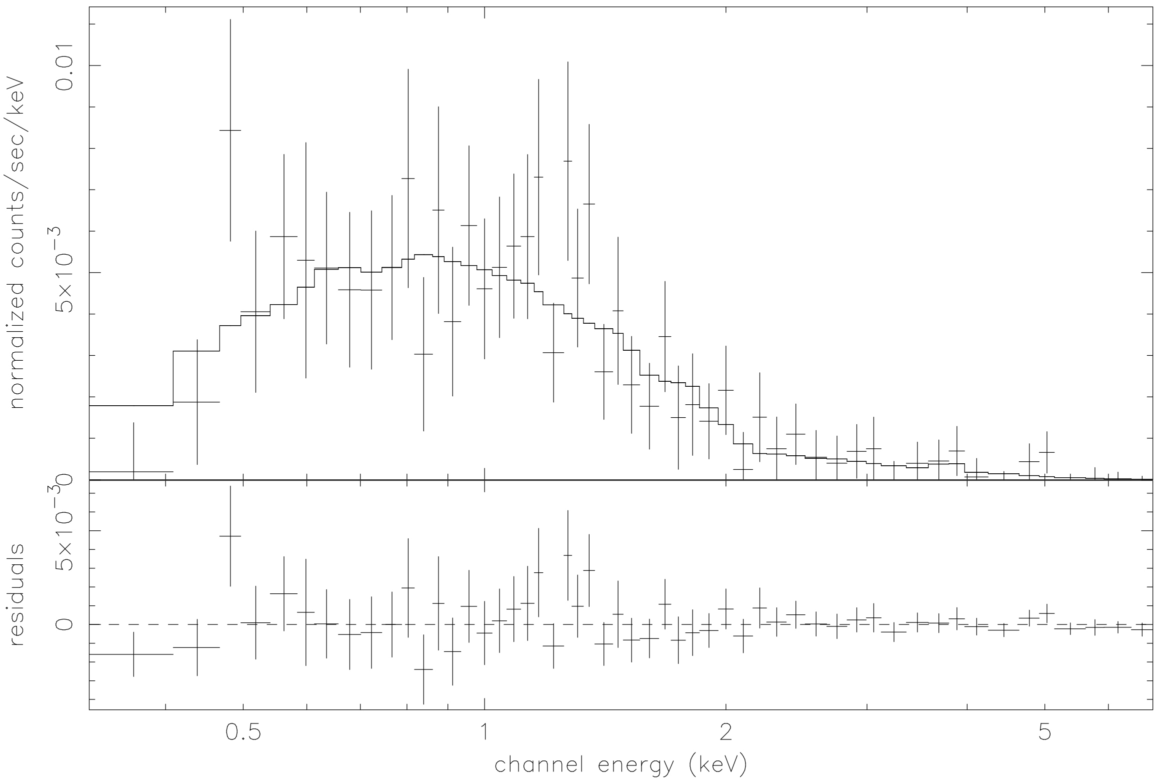

Figure 4.2 XSPEC plot showing a spectrum fit with a single temperature spectral model. This fit resulted in an ambient cluster temperature of $4.31^{+3.7}_{-1.5}$ keV. The spectrum was extracted from a circle centered on the emission peak with a radius of 300 kpc ($\sim$ R$_{2500}$), and was grouped to include 20 counts per bin.

4.4 Surface Brightness

A radial surface brightness profile was computed over the range 0.29-7.0 keV in circular annuli using data which were binned by a factor of 2. This profile was then fit with a β model (Equation 2.1).

The best fitting β model of this cluster is described by $r_c = 19.3^{+3.8}_{-3.2}$ arcseconds (143^{+28}_{-24} kpc), $\beta = 0.62^{+0.12}_{-0.10}$, $I_0 = 9.4^{+1.9}_{-1.4} \times 10^{-9}$ counts sec^{-1} cm^{-2} arcsec^{-2}, and $I_B = 2.8 \pm 0.2 \times 10^{-9}$ counts sec^{-1} cm^{-2} arcsec^{-2}. The reduced χ^2 of the fit was 1.56 for 101 degrees of freedom.

There is an excess of emission within the central $\sim 3''$ of the cluster which was not well fit by a single β model, so a double β model fit was also performed on the data. A double β model takes the form The results of this fit were as follows: $r_1 = 23.7^{+4.7}_{-3.9}$ arcsec, $\beta_1 = 0.71^{+0.14}_{-0.12}$, $I_1 = 8.5^{+1.6}_{-1.4} \times 10^{-9}$ counts sec^{-1} cm^{-2} arcsec^{-2}, $r_2 = 26.6^{+5.3}_{-4.4}$ arcsec, $\beta_2 = 63.6^{+12.7}_{-10.6}$, $I_2 = 19.5^{+3.9}_{-3.3} \times 10^{-9}$ counts sec^{-1} cm^{-2} arcsec^{-2}, and $I_B = 2.9 \pm 0.2 \times 10^{-9}$ counts sec^{-1} cm^{-2} arcsec^{-2}. This fit had a reduced χ^2 of 1.58 for 101 degrees of freedom. A plot of the surface brightness profile of RCS0224-0002 is shown in Figure 4.3 with both the single and double β model fits overplotted.

4.5 Overdensity

Using the results of the β model fits, along with the outcome of previous spectral fitting (Section 4.3), R$_{200}$ was determined to be $1.14^{+0.5}_{-0.2}$ Mpc (68% errors) via the relationship

$$\frac{r_\Delta}{r_c} = \sqrt{\left[\frac{3\beta T}{G\mu m_p (4/3)\pi \rho_c (1+z)^3 r_c^2 \Delta}\right] - 1} \tag{4.1}$$

(Ettori 2000 [43]; Ettori et al. 2004 [46]), where $\rho_c = 3H_0^2 E_z^2/8\pi G$ and $E_z = H_z/H_0 = \left[\Omega_m(1+z)^3 + \Omega_\Lambda\right]^{1/2}$ for a flat cosmology.

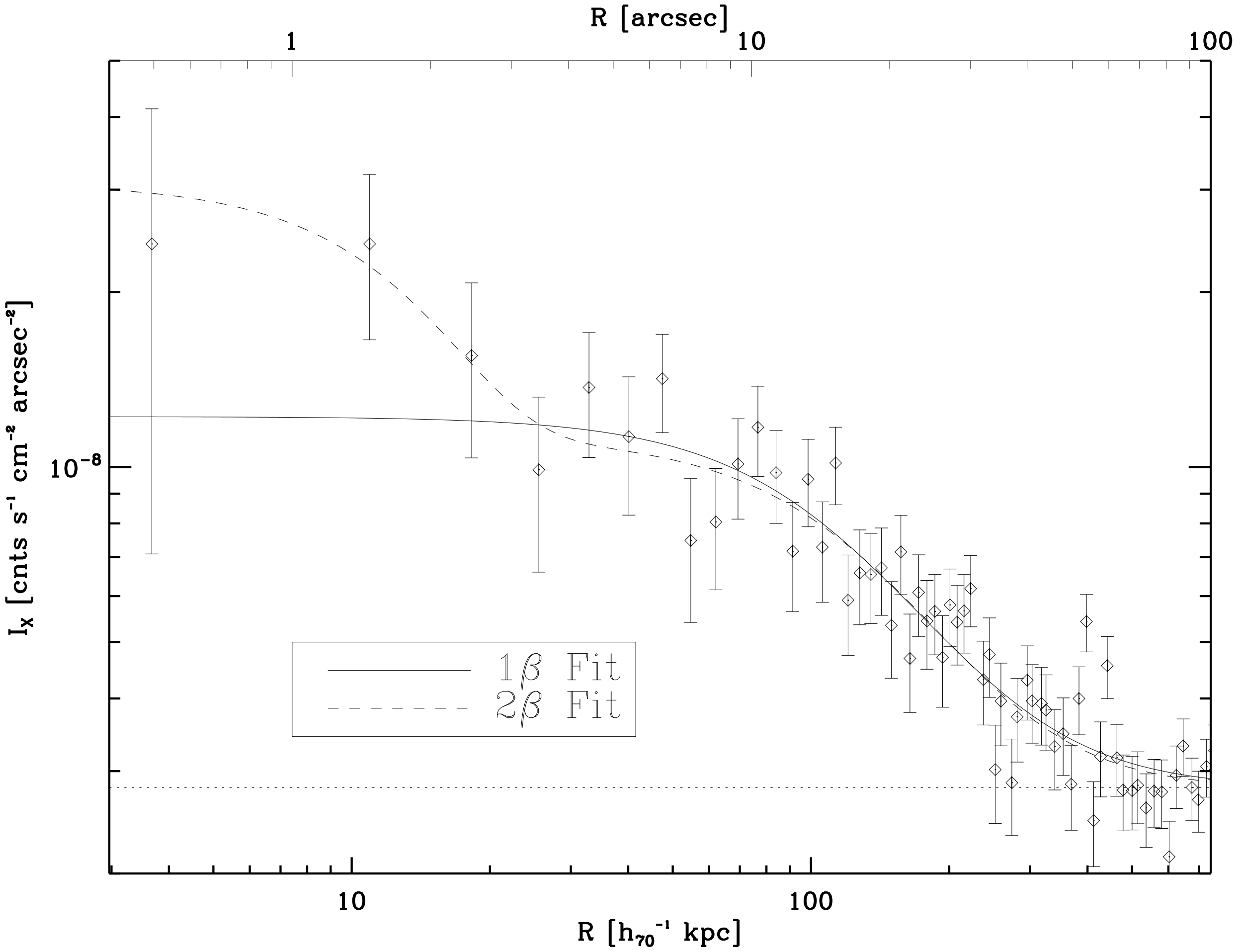

Figure 4.3 Radial surface brightness for the 0.29-7.0 keV band accumulated in 1″ annuular bins. A solid line traces the best fitting single β model fit and the dashed line illustrates the fit obtained by fitting this data with a double β model. The dotted line represents the best fitting background value. Note the excess emission in the inner 10-20 kpc of the cluster.

4.6 Hardness Ratio

Images, instrument maps and exposure maps were created for both a soft X-ray band (0.5-2.0 keV) and a hard band (2.0-8.0 keV) by the method described in Section 4.2. These files were then used to create flux images in the two bands. Radial surface brightness profiles for the two bands were created from the flux images and used to calculate a hardness profile for the cluster expressed by the value $\frac{\mathrm{I_S}-\mathrm{I_H}}{\mathrm{I_{tot}}}$. This profile is presented in Figure 4.4, and indicates that all photons in the central $2''$ of the cluster are soft band photons.

Using the smoothing scale produced in the analysis of the entire energy band, smoothed flux images were created in each of the two bands. The hard band image was subtracted from the soft band image, and the result of that calculation was divided by the smoothed flux image of the entire energy band. Contours of the resulting hardness ratio image are overlayed on a VLA 1.4 GHz radio image in Figure 4.5.

Soft emission is peaked in two places, one corresponding to the peak of the X-ray emission, and the other corresponding to a radio galaxy to the southwest of the X-ray centroid (Figure 4.5). This galaxy is believed to be the cluster cD galaxy (Gladders 2005, private communication).

4.7 Mass Determinations

4.7.1 Density and Cooling Time

The gas mass density distribution of a cluster of galaxies whose surface brightness profile is well described by a β model can be shown to follow:

$$n_{\mathrm{gas}}(r) = n_0 \left(1 + \frac{r^2}{r_c^2}\right)^{-3\beta/2} \tag{4.2}$$

where n_0 is the cluster central density.

This relationship is dependent upon the assumptions of hydrostatic equilibrium,

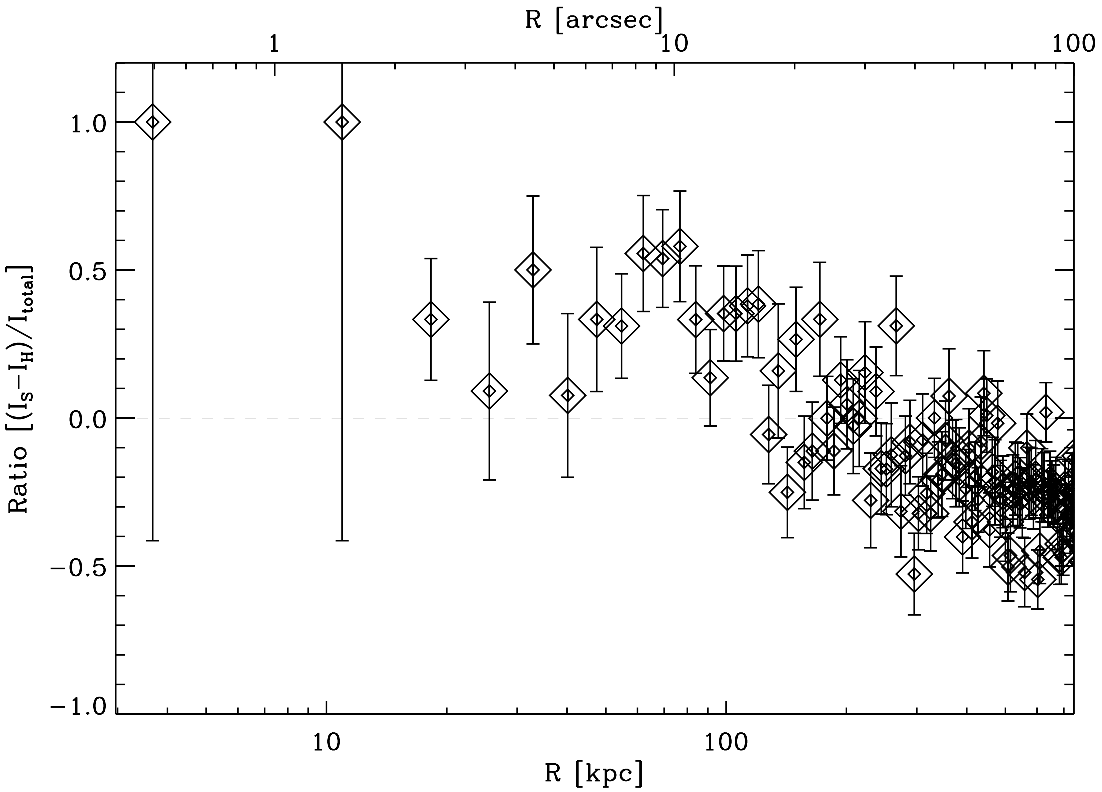

Figure 4.4 This profile was constructed by dividing surface brightness profiles created from flux images in hard (2.0-8.0 keV) and soft (0.5-2.0 keV) X-ray bands, corresponding to $\frac{I_S - I_H}{I_{tot}}$. While soft emission dominates the inner $\sim$ 100 kpc of the cluster, it is particularly noticeable in the very center, corresponding to a small peak in surface brightness in that region (Figure 2.3)

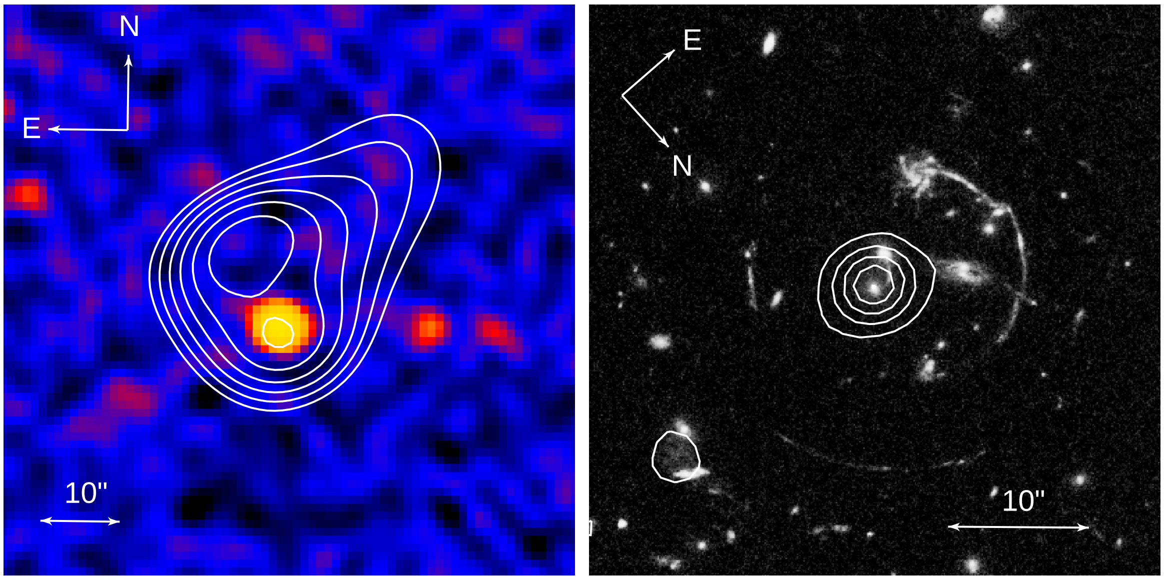

Figure 4.5 **Left panel** - A hardness map was constructed for RCS 0224-0002 by dividing flux images in the hard (2.0-8.0 keV) and soft (0.5-2.0 keV) bands in the manner $\frac{I_S - I_H}{I_{tot}}$. Linearly spaced contours were created from the hardness map and are overlaid on a 1.4 GHz VLA flux image of RCS0224-0002. Two soft emission peaks are evident, one of which coincides with the X-ray centroid. The second peak corresponds to a 1.4 GHz radio source. **Right Panel** - HST image of RCS0224-0002 (Figure 2.1) with radio contours overlaid. 1.4 GHz VLA contours from the flux image shown in the left panel clearly indicate the galaxy which is responsible for the radio emission and corresponding soft X-ray flux.

spherical symmetry, and gas isothermality. The central density in this equation can be determined by an expression relating the observable cluster X-ray luminosity to gas density. This calculation requires the experimental determination of both gas temperature and emission measure, which can be performed in XSPEC.

With the results of spectral analysis (Section 4.3) and the larger β model component (Section 4.4), the central density of RCS0224-0002 is calculated to be $1.50 \pm 0.05 \times 10^{-3}$ cm^{-3}. Using the best fitting surface brightness parameters for just the inner luminosity peak (Section 4.4), a central gas density of $7.3 \pm 0.2 \times 10^{-3}$ cm^{-3} is obtained for that region.

Recall that the characteristic time that it takes a plasma to cool isobarically through an increment of temperature δT can be written

$$\delta t_{cool} = \frac{3}{2} \frac{k}{n\ \Lambda(T)}\ \delta T \tag{4.3}$$

where n is the electron density, Λ(T) is the total emissivity of the plasma (the cooling function), and k is Boltzmann's constant. In the case of isobaric cooling, 3/2 is replaced by 5/2.

Using this formula combined with the cooling function appropriate to a 0.3 solar abundance plasma, the cooling time of RCS0224-0002 is 9.9×10^9 years when estimated from a single β model component. The cooling time calculated from the double β model is 2.7×10^9 years. Estimating the age of a flat universe with the equation

$$\tau = \frac{2}{3\mathrm{H}_0\sqrt{1-\Omega_\mathrm{m}}} \sinh^{-1}\left(\sqrt{\frac{\Omega_\mathrm{m}-1}{(1+\mathrm{z})^3}}\right) \tag{4.4}$$

(Thomas & Kantowski 2004 [111]), at $z = 0.773$ the age of the universe is 6.8×10^9 years.

Therefore the age of the universe exceeds the cooling time of the innermost region of RCS0224-0002. This, combined with the luminosity excess in the central few arcseconds, as well as the existence of a soft X-ray peak at the same location, indicates that this cluster may contain a proto-cooling core. Using the global cluster temperature and the density and β profile of the central emission peak, we calculate a cooling radius of 18 kpc, which corresponds well to the region of excess emission in the surface brightness profile. The observation does not contain enough source photons to obtain spatially resolved temperature information for this cluster, therefore longer exposures will be required to completely characterize the central emission.

At least one other study has detected a high redshift cluster with the signatures of a small cooling core. Grego et al. 2004 [67] in their analysis of a Chandra observation of MS1137.5+6625 (at $z = 0.783$) detect a small central surface brightness excess, and an excess of soft emission in the core of this cluster. They also calculate a central cooling time that is shorter than the age of the universe at that epoch.

4.7.2 Mass Estimates and Comparisons

Using the results of the spectral fit (Section 4.3) and β model fits (Section 4.4), along with Equations 4.2 and 2.3 gas mass and total mass were calculated out to R_{200} for RCS0224-0002, resulting in $M_{tot} = 4.6^{+0.6}_{-0.7} \times 10^{14}$ $M_\odot$ and $M_{gas} = 0.11 \pm 0.02 \times 10^{14}$ $M_\odot$. The resulting gas mass fraction, $f_g = 0.024^{+0.005}_{-0.006}$ h_{70}^{-1}, is a factor of three lower than accepted universal values (Evrard 1997 [48]). This is a phenomenon that is also seen in groups, poor clusters, and other high redshift clusters (Dell'Antonio et al. 1995 [26]; Sanderson et al. 2003 [106]; Sadat et al. 2005 [105]), as well as additional RCS clusters (Chapter 3).

Using a velocity dispersion measurement of 668^{+66}_{-74} km s^{-1} (H. Hoekstra, private communication), a dynamical mass can also be calculated for RCS0224-0002 via Equation 2.8. For this mass estimate we assume that the cluster is isotropic, that $\sigma(\mathrm{r}) = \sigma$, and we employ an NFW model of the form

$$\nu(r) = \rho_0 (r/a)^{-\gamma} \left[1 + r/a\right]^{\gamma - 3} \tag{4.5}$$

using the best fitting values of a and γ for isotropicity (0.224 and 0.75, respectively) from Van der Marel et al. (2000) [27] for the medium redshift Canadian Network for Observational Cosmology (CNOC) sample (Yee, Ellingson & Carlberg 1996 [126]).

Under these assumptions, the virial mass of RCS0224-0002 is $3.3^{+0.6}_{-0.7} \times 10^{14}$ $M_{\odot}$, which is consistent with the X-ray derived mass within the given errors.

4.8 Point Sources

4.8.1 X-ray Source Population

Studies of the AGN population in clusters of galaxies are an important probe of galaxy evolution in these environments (Martini et al. 2002 [88]). While AGN can be difficult to detect at optical wavelengths due to obscuration, they are much more easily seen in the X-ray, where they comprise the dominant contribution to the hard X-ray point source population. In this section we perform an X-ray point source analysis of the Chandra observation of RCS0224-0002.

Using the hard and soft band images and exposure maps referred to in Section 4.6, point sources in these bands were identified using the CIAO tools WTRANSFORM and WRECON. Only sources with a detection significance above 3σ were retained for further analysis.

Using PIMMS, assuming an absorbed powerlaw spectrum with a hydrogen column density fixed at the galactic value and a powerlaw index of 1.6, X-ray fluxes were calculated for each source after correcting for exposure variations across the chips. Log$N$-log$S$ information was then calculated for each energy band, inclusive of all sources within R_{200} (1.14 Mpc). These data were then compared to the log$N$-log$S$ background values of Moretti et al. (2003) [93]. The results of these comparisons with 1σ error bars (Gehrels

1986 [55]) are shown in Figure 4.6. While the data are generally consistent with the measured X-ray background, there appears to be a very slight excess of low-flux soft energy sources within R_{200}.

A list of point sources within R_{200} is given in both Table 4.1 and Table 4.2 for the 0.5-2.0 keV and 2.0-8.0 keV bands, respectively. These tables include both flux and luminosity information (also achieved with PIMMS, assuming a redshift of $z = 0.773$) for each source. Of the eleven point sources which are detected in both the soft and hard bands, all but two of the bolometric luminosities (calculated separately for each band) are consistent to within 3σ, indicating that a powerlaw index of 1.6 is a sufficient approximation for the majority of the point sources in this sample.

To compare the distribution of sources in the RCS0224-0002 field to those reported in Ruderman & Ebeling (2005) [104], radial histograms containing the number of sources per square megaparsec (assuming a redshift of $z = 0.773$) were created from data in each energy band (Figure 4.7). These plots indicate a significant excess of point sources within R_{200}, particularly in the $0.6 - 0.8$ R_{200} bins. The Ruderman & Ebeling (2005) [104] study was conducted in the 0.5-2.0 keV energy band, and our soft band data are roughly consistent with their result that there is a pronounced central peak followed by a depleted region and then a broader secondary excess at approximately the virial radius.

We have also undertaken a simple calculation to determine whether the amount of energy injected into the intracluster medium by AGN could be responsible for the low gas mass fraction that we detect in this cluster. The X-ray luminosities of all 2-8 keV point sources within R_{200} were converted to bolometric luminosities using the relationships of Elvis et al. 1994 [41] (i.e. for a broad-line AGN hard X-ray luminosity function, $L_{bol} = 35\ L_X$). The combined luminosities of all point sources within R_{200} were then converted to an estimate of total contributed energy by assuming a duration of activity of 10^8 years. To calculate the energy of the gas component of RCS 0224-

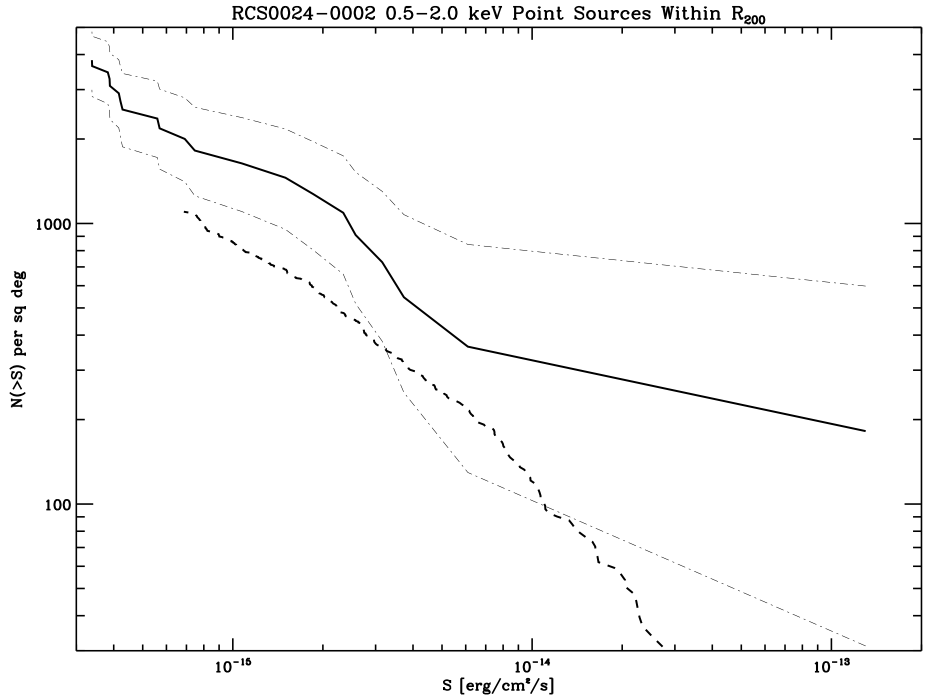

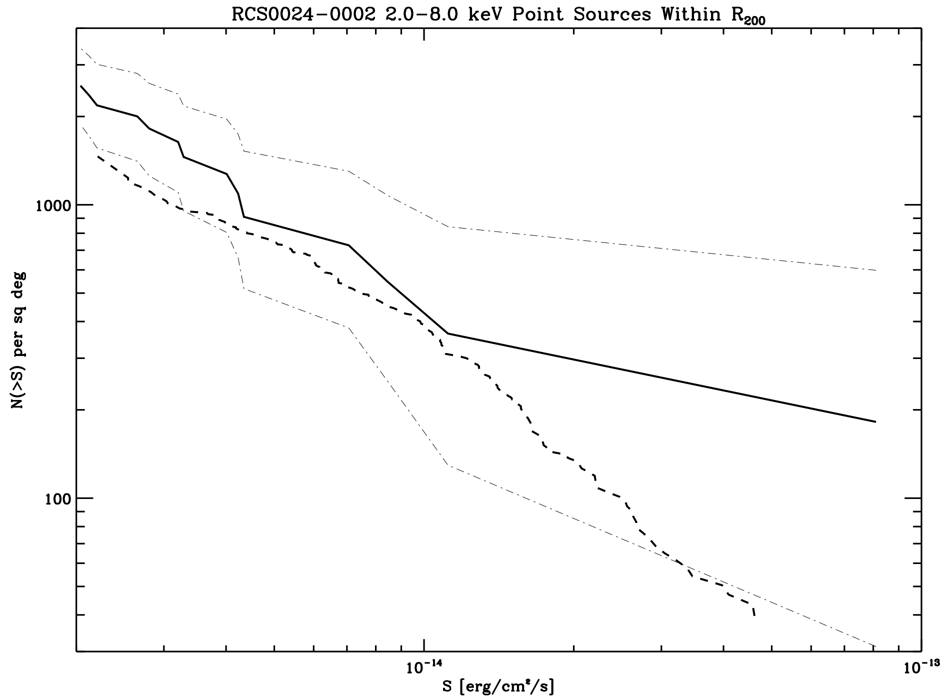

Figure 4.6 LogN-LogS plot of point sources within R_{200} (1.14 Mpc) in soft (0.5-2.0 keV) and hard (2-10 keV) X-ray bands. The dashed lines represent the X-ray background in these energy bands (Moretti et al. 2003 [93]). The solid line in each plot indicates the LogN-LogS distribution of detected sources. Dot dash lines indicate 1σ confidence intervals. A slight excess of low flux point sources can be seen in the soft energy band.

Table 4.1. 0.5-2.0 keV Point Sources for R $<$ R_{200}

Number[a]	RA [J2000]	Dec [J2000]	Flux[b]	L_x[c] [10^{42} erg s^{-1}]	σ	Distance [Mpc]	1.4 GHz
1	02:24:34.407	-00:02:25.99	4.3 ± 1.5	0.75 ± 0.26	4.0	0.030	···
2	02:24:37.294	-00:02:50.05	5.6 ± 1.7	0.98 ± 0.298	5.3	0.397	yes
3	02:24:38.204	-00:03:28.67	3.4 ± 1.3	0.59 ± 0.23	3.4	0.655	yes
4 (2)	02:24:39.024	-00:01:37.76	23.4 ± 3.4	4.11 ± 0.59	20.6	0.664	···
5	02:24:28.659	-00:03:18.18	10.7 ± 2.3	1.88 ± 0.399	10.1	0.732	···
6 (3)	02:24:33.307	-00:04:05.04	5.7 ± 1.7	1.00 ± 0.29	5.6	0.748	yes[d]
7 (4)	02:24:27.158	-00:02:25.45	3.9 ± 1.5	0.68 ± 0.26	3.5	0.790	yes
8 (5)	02:24:28.721	-00:03:42.48	31.6 ± 3.9	5.55 ± 0.68	27.5	0.838	···
9 (6?)	02:24:27.309	-00:01:32.66	4.2 ± 1.4	0.73 ± 0.25	4.0	0.874	yes
10 (7)	02:24:40.371	-00:03:40.74	60.998 ± 5.3	10.72 ± 0.94	54.8	0.899	yes
11 (9)	02:24:33.988	-00:04:25.99	25.7 ± 3.5	4.52 ± 0.61	24.6	0.900	···
12 (10)	02:24:42.033	-00:02:43.51	14.989 ± 2.6	2.63 ± 0.46	14.3	0.901	···
13 (11)	02:24:30.602	-00:00:38.80	1301.65 ± 24.3	228.78 ± 4.27	860.0	0.907	yes
14	02:24:26.121	-00:01:54.64	6.9 ± 1.8	1.21 ± 0.32	6.4	0.939	···
15	02:24:39.696	-00:00:45.58	3.4 ± 1.3	0.5955 ± 0.23	3.3	0.988	yes
16 (12)	02:24:28.124	-00:04:03.93	4.2 ± 1.4	0.74 ± 0.25	4.1	1.001	yes
17 (13)	02:24:40.173	-00:04:09.31	37.3 ± 4.2	6.56 ± 0.73	34.8	1.031	···
18 (14)	02:24:42.381	-00:03:32.12	3.8 ± 1.4	0.67 ± 0.24	3.8	1.054	···
19	02:24:25.150	-00:03:11.24	3.9 ± 1.4	0.68 ± 0.25	3.7	1.071	···
20	02:24:29.556	-00:00:20.42	18.5 ± 2.9	3.26 ± 0.52	16.3	1.084	···
21	02:24:43.016	-00:03:26.62	7.5 ± 1.9	1.31 ± 0.33	7.4	1.100	···

[a] 0.5-2.0 keV (2.0-8.0 keV)

[b] Unabsorbed 0.5-2.0 keV flux in units of $10^{-}16$ erg cm^{-2} s^{-1}

[c] Unabsorbed bolometric X-ray luminosity obtained using 0.5-2.0 keV count rates and PIMMS, assuming z=0.773 and a powerlaw index of 1.6

[d] SCUBA submillimeter source [117]

Table 4.2. 2.0-8.0 keV Point Sources for R $<$ R_{200}

Number[a]	RA [J2000]	Dec [J2000]	Flux[b]	L_x[c] [10^{42} erg s^{-1}]	σ	Distance [Mpc]	1.4 GHz
1	02:24:36.402	-00:02:02.77	28.0 ± 8.7	2.83 ± 0.87	4.5	0.312	yes
2 (4)	02:24:39.024	-00:01:37.30	32.0 ± 8.958	3.24 ± 0.90	5.6	0.666	···
3 (6)	02:24:33.330	-00:04:04.68	42.3 ± 10.1	4.27 ± 1.02	7.5	0.745	yes[d]
4 (7)	02:24:27.141	-00:02:25.23	84.6 ± 15.0	8.54 ± 1.52	13.1	0.792	yes
5 (9)	02:24:28.742	-00:03:42.17	26.5 ± 8.2	2.68 ± 0.83	4.6	0.835	···
6 (10?)	02:24:27.472	-00:01:27.60	20.4 ± 7.2	2.06 ± 0.73	3.7	0.876	···
7 (11)	02:24:40.381	-00:03:40.73	111.7 ± 15.9	11.28 ± 1.61	19.3	0.899	yes
8	02:24:40.943	-00:01:24.56	21.2 ± 7.4	2.14 ± 0.75	3.8	0.900	···
9 (12)	02:24:34.014	-00:04:26.24	32.9 ± 8.9	3.32 ± 0.897	6.2	0.902	···
10 (13)	02:24:42.042	-00:02:43.29	43.4 ± 10.1	4.39 ± 1.02	7.7	0.902	···
11 (14)	02:24:30.602	-00:00:38.87	810.4 ± 42.1	81.83 ± 4.25	107.6	0.906	yes
12 (17)	02:24:28.115	-00:04:03.44	22.0 ± 7.6	2.22 ± 0.76	3.8	0.999	yes
13 (18)	02:24:40.170	-00:04:09.34	70.6 ± 12.8	7.13 ± 1.29	12.3	1.031	···
14 (19)	02:24:42.357	-00:03:31.70	40.1 ± 9.998	4.05 ± 1.01	6.5	1.050	···

[a] 2.0-8.0 keV (0.5-2.0 keV)

[b] Unabsorbed 2.0-8.0 keV flux in units of $10^{-}16$ erg cm^{-2} s^{-1}

[c] Unabsorbed bolometric X-ray luminosity obtained using 2.0-8.0 keV count rates and PIMMS, assuming z=0.773 and a powerlaw index of 1.6

[d] SCUBA submillimeter source [117]

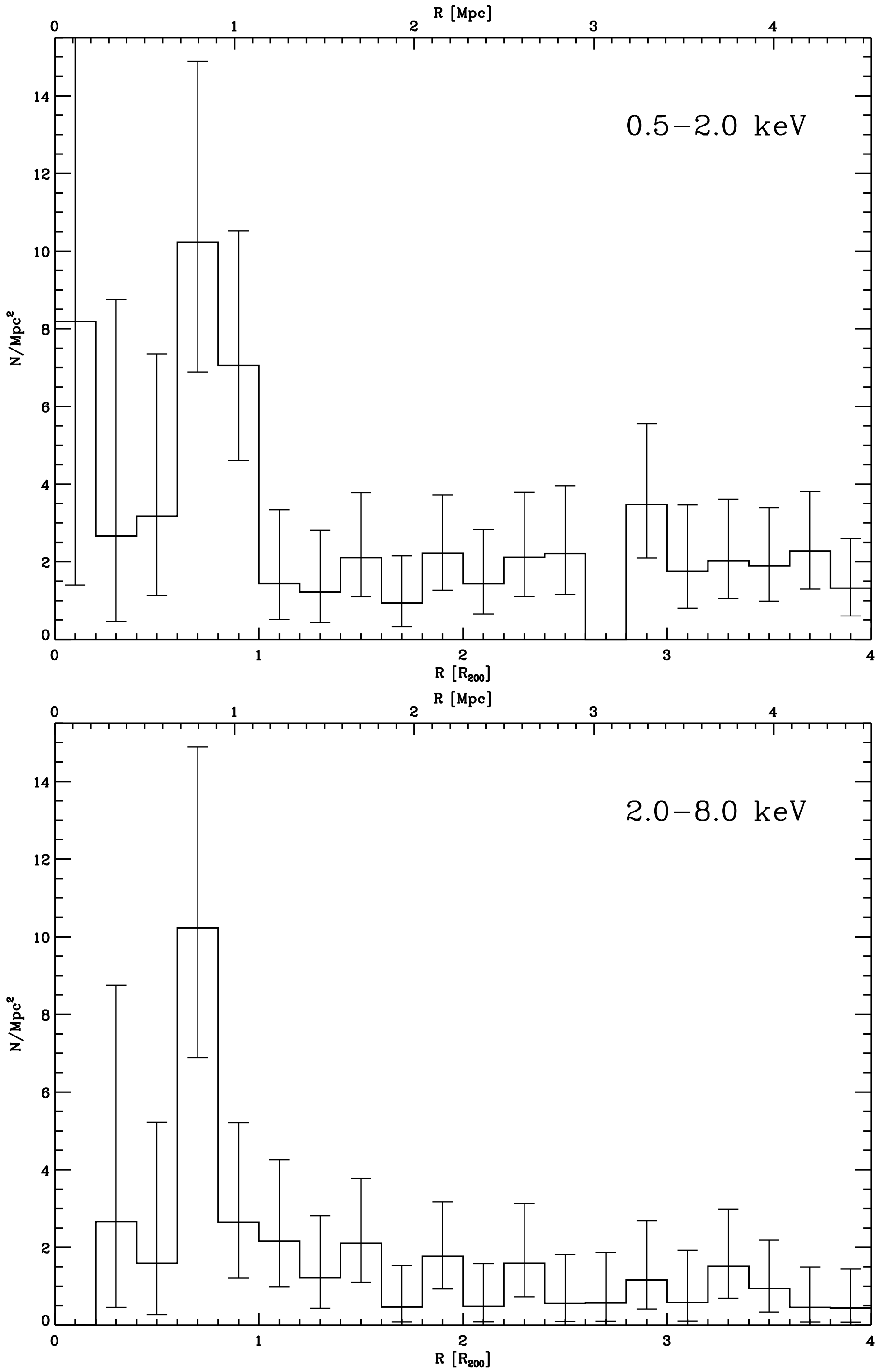

Figure 4.7 Histograms of point source density vs. radius were constructed from data in soft (0.5-2.0 keV) and hard (2-10 keV) energy bands, and are shown here with 1σ error bars. The soft band shows evidence of a central peak, and both energy bands indicate an excess of point sources just inside of R_{200}. Each of these plots are consistent with the findings of Ruderman & Ebeling 2005 [104].

0002, we simply multiplied the gas mass within R_{200} by its ambient temperature. In this way we estimate that AGN contributions to cluster energy could make up > 10% of the energy in the gas within R_{200}, assuming that all detected point sources lie in the cluster. If we use an average value of 1 source per Mpc^2 as a background estimate (Figure 4.7), the energy contribution is reduced by 0.7%. This added energy could raise the entropy of the system, and in that way contribute to the observed low gas mass fraction of the cluster.

4.8.2 Multi-wavelength Comparisons

RCS0224-0002 was observed with the National Radio Astronomy Observatory's (NRAO) Very Large Array (VLA) at 1.4 GHz for a total of 15 hours over three days. Though the data are currently in an initial stage of analysis, basic calibrations have been performed, and a calibrated FITS image of the data has been provided (T.M.A. Webb, private communication). Without more extensive radio analysis, it is difficult to provide quantitative results with regard to the 1.4 GHz characteristics of point sources in the RCS0224-0002 field, however a qualitative estimate of the coincidence of X-ray point sources with 1.4 GHz sources can be performed on the current data. Figure 4.8 consists of the 1.4 GHz radio image of RCS0224-0002 with 0.2-5.0 and 2.0-8.0 X-ray point source regions overlaid. Obvious correlations are noted in Tables 4.1 and 4.2, and can be seen in Figure 4.8.

RCS0224-0002 was also observed at both 450μm and 850μm with the Submillimeter Common-User Bolometer Array (SCUBA) (Holland et al. 1998 [77]) in 2001 and 2002. The results of these observations are reported in Webb et al. (2005) [117], and have resulted in five submillimeter source detections in the RCS0224-0002 field. Only one of the five sources is coincident with an X-ray detected point source, smm-RCS0224.2 (source 6 in Table 4.1 and source 3 in Table 4.2).

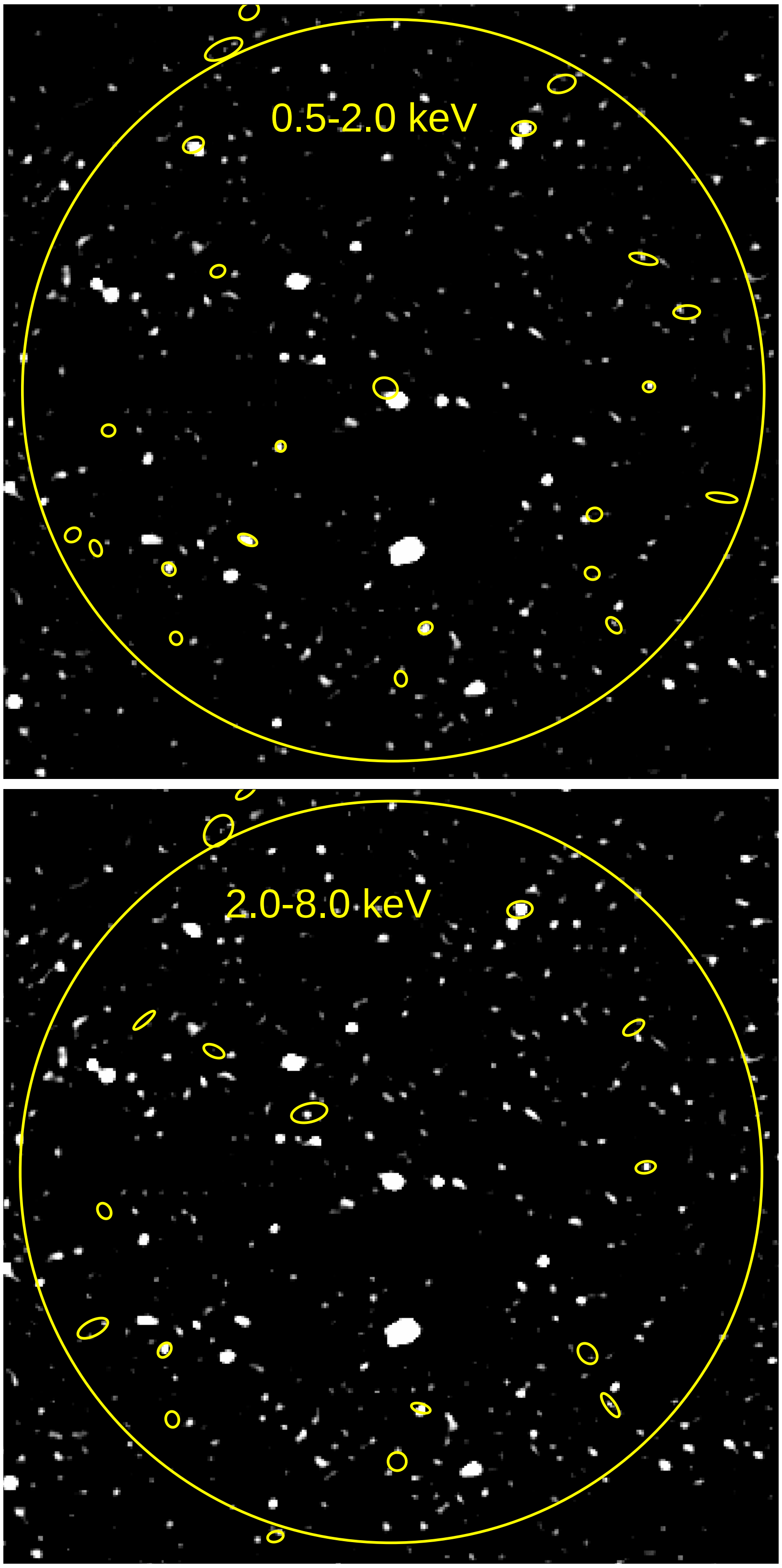

Figure 4.8 X-ray point source region files produced by running WAVDETECT on 0.5-2.0 keV and 2.0-10.0 keV flux images are overlaid on a 1.4 GHz VLA image of RCS0224-0002. The large circles have a 1.14 Mpc (R_{200}) radius. Within that region, nine of 21 soft band X-ray point sources are found to be coincident with radio emission, and six of 14 detected in the hard X-ray band. North is up in both images.

4.9 Summary and Discussion

This chapter describes the results of the most in depth X-ray analysis of an optically selected high redshift RCS cluster to date, the 89 ks Chandra observation of the lensing cluster RCS0224-0002 at $z = 0.773$. Imaging analysis reveals that the peak of X-ray emission lies $4''$ away from the center of the lensing arcs, probably due to slightly offset mass concentrations along the line of sight.

Single temperature spectral fitting of the X-ray emission within a 300 kpc (R_{2500}) radius indicates that this cluster has an ambient temperature of $4.3^{+3.7}_{-1.5}$ keV. The surface brightness profile of RCS0224-0002 exhibits a small (10-20 kpc) central peak of emission which can be modeled via the inclusion of a second β component. The best fitting double β model has an outer core radius of 143^{+28}_{-24} kpc and β value of $0.62^{+0.12}_{-0.1}$. Using the results of both temperature and surface brightness fitting, R_{200} is determined to be $1.14^{+0.5}_{-0.2}$ Mpc for this cluster.

Hardness ratio profiles and maps were created from soft (0.5-2.0 keV) and hard band (2.0-8.0 keV) flux images. A peak in soft X-ray emission is seen to coincide with the central peak in surface brightness. A second soft emission peak is coincident with a 1.4 GHz VLA radio source, and is centered on one of the galaxies in the HST image (Figure 2.5). To date, no spectroscopic follow up has been done on this galaxy, though it is believed to be the cluster cD (Gladders 2005, private communication).

Using the results of both spectral and surface brightness fitting, we have calculated a central density for RCS0224-0002 of 0.0073 ± 0.002 cm^{-3}, which results in a central cooling time of 2.7×10^9 years and a cooling radius of 18 kpc. Without spatially resolved temperature information we are unable to confirm the presence of a cool component in the center of RCS0224-0002, however the central surface brightness excess and corresponding soft peak of emission support the idea that RCS0224-0002 contains a small proto-cooling core. Similar evidence has been detected in another $z \sim 0.8$ cluster, MS1137.5+6625 (Grego et al. 2004 [67]). These two clusters are the highest redshift systems in which central cooling has yet been detected (albeit indirectly), and their existence provides evidence that quiescent clusters can be formed at very high redshift and remain undisturbed for significant durations.

Mass estimates of RCS0224-0002 result in a total mass of $4.6^{+0.6}_{-0.7} \times 10^{14}$ M$_\odot$ and a gas mass of $1.1 \pm 0.2 \times 10^{13}$ M$_\odot$. This estimate of total gravitating mass is consitent within 68% errors with dynamical mass estimates of $3.3^{+0.6}_{-0.7} \times 10^{14}$ M$_\odot$. The consistency of these mass estimates is an indication that RCS0224-0002 is a relaxed system.

An investigation of the point souce population in the field of RCS0224-0002 indicates that a general overdensity of point sources does not exist within R$_{200}$ of the cluster center. This may be due in part to a selection effect which makes it more difficult to detect point sources close to the cluster center due to the surface brightness of the cluster. Radial distributions of these sources exhibit a significant peak at ~ 0.7 R$_{200}$ in both the hard and soft bands, possibly indicating that the cluster potential is influencing AGN activity at that radius. Spectral information on cluster member galaxies is needed, however, to test that hypothesis. The radial profile of soft X-ray sources is consistent with the results of Ruderman & Ebeling (2005) [104]. X-ray point sources within the field of RCS0224-0002 have been compared to preliminary 1.4 GHz VLA flux information, and coincident sources are listed in Tables 2.1 and 2.2.

The gas mass fraction of this cluster, $f_g = 0.024^{+0.005}_{-0.006}\ h_{70}^{-1}$, is a factor of three lower than accepted values (Evrard 1997 [48]). This is a phenomenon that is also seen in groups, poor clusters, and other high redshift clusters (Dell'Antonio et al. 1995 [26]; Sanderson et al. 2003 [106]; Sadat et al. 2005 [105]). While the AGN component of RCS0224-0002 may provide a significant contribution to the entropy of this system ($\sim 10\%$), it is likely that other non-gravitational processes (i.e. galaxy formation) are also involved.

In this analysis we have collected ample evidence that RCS0224-0002 is in a state of relaxation, indicating that substructure within the cluster is unlikely to be the cause of enhanced gravitational lensing. The size of the cool core is also too small to account for a boost in the lensing cross section. This suggests that the strong lensing exhibited by this cluster is probably a result of superpositions of mass along the line of sight, an idea which is corroborated by our finding that the X-ray centroid is slightly displaced ($\sim 4''$ or ~ 30 kpc) from the center of the lensing arcs. This interpretation is further supported by reports on the lensing analysis of this cluster (Hoekstra 2005, private communication) which indicate that an additional massive structure is required to accurately model the system of arcs. In light of this finding we propose that the high incidence of strong lensing seen in the RCS sample is partially due to the proclivity of this survey to detect closely spaced superpositions of structure along the line of sight.

Chapter 5

Multiwavelength Mass Comparisons of High Redshift Clusters

5.1 Introduction

Clusters of galaxies have the potential for being extraordinary cosmological probes. They are the largest systems in the universe, and as such can provide important constraints on the growth of large scale structure (e.g. Eke et al. 1998 [37]; Bahcall, Fan & Cen 1997 [11]). To achieve such constraints however, a large cluster sample is required which spans a wide range of redshifts, and is replete with mass estimates. While the first piece of this requirement is swiftly being met through both planned and executed cluster surveys (e.g. RCS; Gladders & Yee 2005 [63]; XMM-LSS; Valtchanov et al. 2004 [114]; ChaMP; Wilkes et al. 2000 [121]), there is some uncertainty as to the most reliable and efficient method of mass estimation.

The X-ray temperatures of clusters, which directly reflect the depth of cluster potentials, are robust estimators of cluster mass. Furthermore, the X-ray luminosity of clusters is a measure of the gas density within this potential. For these reasons X-ray observations of clusters of galaxies are perhaps the most ideal route by which to achieve information about their large scale properties. X-ray observations are an expensive use of resources however, and become even more expensive at high redshift. For that reason alone it would be beneficial to have the ability to accurately estimate cluster masses via alternate methods. Two potentially inexpensive options are the Sunyaev-Zeldovich (SZ) effect (Sunyaev & Zeldovich 1970 [110]) and optical richness measurements.

SZ observations detect distortions in the cosmic microwave background (CMB) due to Compton scattering from hot intracluster electrons, therefore they are also direct probes of the gas distribution in clusters. Unlike X-ray observations, however, the magnitude of the SZ signal is largely unaffected by redshift. This, in principle, allows mass-limited (rather than distance-limited) cluster surveys to be carried out in the SZ (e.g., Carlstrom et al. 2002 [21]). One of the challenges facing SZ mass estimations is the systematic uncertainty which is introduced by assuming the spatial distribution of the intracluster medium (ICM) (Benson et al. 2004 [14]).

Optical richness (e.g. Abell 1958 [1]; Yee & Lopez-Cruz 1999 [124]) is a parameter which describes the magnitude of galactic overdensities in clusters. Assuming that galaxy overdensity reflects the underlying dark matter density profile of a cluster, this quantity should correlate with total cluster mass. Difficulties inherent in this method include uncertainties in the evolution of the cluster luminosity function and a need to correct this parameter for the redshift evolution of dark matter density profiles.

For either of these approaches to provide reliable estimates of cluster mass, they must first be calibrated by and compared to alternative mass measurements. In this paper we compare independent SZ, X-ray, and optical richness mass estimations for a sample of five high redshift optically selected clusters from the Red-sequence Cluster Survey (RCS; Gladders & Yee 2005 [63]).

5.2 Follow-up Observations of RCS Clusters

5.2.1 OVRO and BIMA Observations

Using the 30 GHz receivers mounted on the OVRO 10 m telescopes and the BIMA 6.1 m telescopes, K. Dawson and the BIMA group observed five galaxy clusters discovered by the Red-Sequence Cluster Survey (RCS) (Gladders & Yee 2000, 2005 [62, 63]). Four of these clusters are found to have multiple strong lensing arcs in R band observa-

Table 5.1. Field Positions and Observation Times

Fields	z	R.A. [J2000]	Dec. [J2000]	Telescope(s)	Time [Hrs]
RCS0224-0002	0.773	$02^{\mathrm{h}}\,24^{\mathrm{m}}\,34.1^{\mathrm{s}}$	$-00^\circ\,02'\,31''$	OVRO, BIMA	63.8
RCS1324+2845	0.96	$13^{\mathrm{h}}\,24^{\mathrm{m}}\,28.3^{\mathrm{s}}$	$+28^\circ\,44'\,57''$	OVRO	20.8
RCS1326+2903	0.71[a]	$13^{\mathrm{h}}\,26^{\mathrm{m}}\,31.1^{\mathrm{s}}$	$+29^\circ\,03'\,20''$	OVRO, BIMA	43.8
RCS1419+5326	0.64	$14^{\mathrm{h}}\,19^{\mathrm{m}}\,12.1^{\mathrm{s}}$	$+53^\circ\,26'\,13''$	OVRO	9.2
RCS1620+2929	0.87	$16^{\mathrm{h}}\,20^{\mathrm{m}}\,09.9^{\mathrm{s}}$	$+29^\circ\,29'\,21''$	OVRO	7.6

[a]Most probable redshift. This cluster may be at z=0.93 (see text for explanation)

tions (Gladders et al. 2003 [61]). The coordinates of each cluster along with redshift and total integration time are found in Table 5.1 (K. Dawson 2005, private communication). The redshift, z, is taken from RCS catalogues. In the case of RCS1326+2903, two RCS 13h clusters lie in the field of view, one at an RA, Dec of 13:26:29, +29:03:06 (J2000) and the other at 13:26:31, +29:03:12. It is uncertain which of these clusters the signal originates from, therefore both possibilities are carried throughout the analysis. Of the five clusters observed, only RCS0224 and RCS1326 show significant detections ($> 4\sigma$) in the image plane in an analysis of the interferometry data.

5.2.2 Chandra Observations

Chandra Advanced CCD Imaging Spectrometer (ACIS) observations of nine RCS clusters were taken during the period 10 April 2002 - 13 April 2005. Four of these clusters overlap with the RCS cluster sample that was observed with OVRO and/or BIMA (RCS0224-0002, RCS1326+2903, RCS1419+5326, and RCS1620+2929). All four of these clusters were observed with the ACIS-S CCD array, with an overall range in individual exposures of $9.9 - 89.0$ kiloseconds (Table 2.2). RCS1326+2903 was observed on two occasions, and the resulting event files were merged to provide higher overall signal-to-noise. Astrometry indicates that the X-ray centroid of RCS1326+2903 lies closer to the expected position of the low-z RCS cluster in this field, however both

Table 5.2. Chandra Observations

Cluster	z	X-ray Centroid Position R.A. [J2000]	Dec. [J2000]	Total Exposure [s]
RCS0224-0002	0.773	$02^{\mathrm{h}}\,24^{\mathrm{m}}\,34.2^{\mathrm{s}}$	$-00^\circ\,02'\,26.9''$	88973
RCS1326+2903	0.71[a]	$13^{\mathrm{h}}\,26^{\mathrm{m}}\,30.9^{\mathrm{s}}$	$+29^\circ\,03'\,28.8''$	63590
RCS1419+5326	0.64	$14^{\mathrm{h}}\,19^{\mathrm{m}}\,12.2^{\mathrm{s}}$	$+53^\circ\,26'\,10.6''$	9904
RCS1620+2929	0.87	$16^{\mathrm{h}}\,20^{\mathrm{m}}\,10.0^{\mathrm{s}}$	$+29^\circ\,29'\,20.4''$	34899

[a]Most probable redshift. This cluster may be at z=0.93 (see text for explanation)

possibilities are propagated throughout the analysis. A detailed discussion of data reduction techniques and analysis procedures can be found in Chapter 3. Table 5.2 lists each cluster, its redshift, the X-ray determined position of the cluster center, and its net Chandra exposure.

5.3 SZ Analysis

5.3.1 Point Sources

Radio point sources can bias estimates of the SZ decrement associated with a galaxy cluster. In order to account for possible contaminants in the cluster analysis, the BIMA group identified all sources within a radius of 200″ of the cluster center as catalogued in the NVSS survey (Condon et al. 1998 [24]). Point sources which lie close to the center of the observed field may lead to an underestimation of the observed flux, however the off-center point source in the field of RCS1326+2903 may result in a small overestimate of the mass of this cluster. If this is the case, the overestimate should only be of the order of a few percent (K. Dawson 2005, private communication). The positions of radio sources in the RCS fields are shown in Table 5.3. Also listed are the fluxes from the NVSS survey at 1.4 GHz and the best fit 30 GHz fluxes determined from the OVRO and BIMA visibility data (K. Dawson 2005, private communication).

Table 5.3. Radio Point Sources in the RCS Fields

Field	Δ R.A. [arcsec]	Δ Dec. [arcsec]	NVSS Flux [mJy]	30.0 GHz Flux [μJy]
RCS1324+2845	-24.2	10.2	5.1 ± 0.5	39 ± 70
RCS1326+2903	10.0	20.0	2.8 ± 0.5	582 ± 67
RCS1419+5326	108.1	-176.3	122.3 ± 3.7	15670 ± 895
RCS1620+2929	-111.6	-122.2	3.8 ± 0.5	356 ± 478
RCS1620+2929	165.7	20.9	5.2 ± 0.4	918 ± 604

5.3.2 SZ Analysis

The visibility data from the 30 GHz observations were fit to β model profiles. The spherical isothermal β model density is described by

$$n_e(r) = n_{e0}\left(1 + \frac{r^2}{r_c^2}\right)^{-3\beta/2} \tag{5.1}$$

where the core radius r_c and β are shape parameters, and n_{e0} is the central electron number density. With this model, the SZE temperature decrement is

$$\Delta T(r) = \Delta T_0\left(1 + \frac{\theta^2}{\theta_c^2}\right)^{1/2-3\beta/2} \tag{5.2}$$

where $\theta = r/D_A$, D_A is the angular diameter distance, and ΔT_0 is the temperature decrement at zero projected radius. The central electron density, n_{e0}, can be derived from eq. 5.1 and eq. 5.2.

$$n_{e0} = \frac{-\Delta T_0}{T_{CMB}}\frac{m_e c^2}{2k_B\sigma_T T_e}\left[D_A\int_{-\infty}^{\infty}\left(1 + \frac{\theta^2}{\theta_c^2}\right)^{-3\beta/2} d\theta\right]^{-1} \tag{5.3}$$

A probability distribution function of cluster parameters based on observational data was obtained through a likelihood analysis employing Markov chains (Bonamente et al. 2004 [17]). The analysis was then used to estimate the central decrement (ΔT_0) and the core radius (θ_c) of each RCS cluster. The optical cluster center reported by

Table 5.4. Results from Markov Analysis

Field	$-\Delta T_0$ [μK]	θ_c [arcsec]
RCS0224-0002	693^{+288}_{-185}	$11.6^{+7.7}_{-4.4}$
$(-9.7'', -5.1'')$	703^{+293}_{-187}	$11.9^{+7.3}_{-4.6}$
RCS1324+2845	-271^{+171}_{-203}	$11.9^{+9.0}_{-5.7}$
RCS1326+2903	306^{+159}_{-150}	$15.5^{+7.2}_{-7.0}$
$(5.5'', -14.7'')$	364^{+173}_{-147}	$14.2^{+7.4}_{-6.2}$
RCS1419+5326	147^{+327}_{-321}	$11.8^{+9.0}_{-5.7}$
RCS1620+2929	128^{+273}_{-226}	$11.4^{+8.7}_{-5.6}$

the RCS group is assumed to be the central position for each cluster. In the analysis of RCS clusters, β is fixed at a reasonable value of 0.66 (Henry et al. 1993 [71]). An analysis with the SZ data alone produces only weak constraints on estimates of the core radius and β so there is negligible information lost in setting $\beta = 0.66$. Results from the analysis can be found in Table 5.4 (K. Dawson 2005, private communication).

Note that for RCS0224 and RCS1326, a separate analysis was performed in which the central position of the cluster was allowed to vary. The best fit position for RCS0224 was found to be offset from the optical cluster center by $\Delta x = -9.7'', \Delta y = -5.1''$ and the best fit position for RCS1326 was offset from the optical center by $\Delta x = 5.5'', \Delta y = -14.7''$. These offsets are well within the uncertainties of the cluster center derived from optical images, and are also small compared to the size of the synthesized beam $(1 - 2')$, therefore they are not significant. In all other cases the central decrement was held fixed at the position reported by the RCS group.

5.4 Mass Estimates from Multiple Wavelengths

5.4.1 Optical Richness and Mass

The CNOC1 (Yee, Ellingson & Carlberg 1996 [126]) survey is a multi-object spectroscopy survey of galaxy clusters in the redshift range $0.17 < z < 0.55$. 15 clusters used in the survey were selected from the Einstein Medium Sensitivity Survey (EMSS; Gioia et al. 1990 [57]). One additional cluster was taken from the Abell catalog (Abell 1958 [1]). The sample has been used to investigate the correlation between optical richness and other cluster properties (Yee & Ellingson 2003 [125]; Chapter 2). An analysis of galaxy clusters in the CNOC1 cluster redshift survey shows a strong correlation between optical richness and X-ray temperature at $< z >\sim 0.2 - 0.6$. For X-ray temperature, T_X, the correlation is found to be

$$T_X = 2.4 \pm 0.3 \ {B_{gc,red}}^{1.13} \tag{5.4}$$

where $B_{gc,red}$ is the optical richness parameter, defined as the galaxy-cluster center correlation amplitude (Longair & Seldner 1979 [84]) and calculated using only red-sequence cluster galaxies. Similar correlations are found between optical richness and virial mass, and optical richness and the characteristic radius, R_{200}, but with larger scatter. These relationships have been modeled as

$$E_z M_{200} = 8 \pm 2 \times 10^9 \ {B_{gc,red}}^{1.69} \tag{5.5}$$

where $E(z) = H(z)/H_0 = \left[\Omega_m(1+z)^3 + \Omega_\Lambda\right]^{1/2}$ for a flat cosmology, and $E_z M_{200}$ is in units of h_{70}^{-1} M$_\odot$. A corresponding estimate for R_{200}, in units of h_{70}^{-1} Mpc, is found to be

$$R_{200} = 3.8^{+0.3}_{-0.2} \times 10^{-}2 \ {B_{gc,red}}^{0.56} \tag{5.6}$$

We use the optical richness for the RCS clusters to estimate the cluster parameters of virial mass, characteristic radius, and X-ray temperature. The optical richness, mass, and X-ray temperature estimated from optical richness are found in Table 5.5 for the RCS clusters observed with OVRO and BIMA.

Table 5.5. Mass Estimates and Cluster Parameters from Optical Richness ($\mathrm{Bgc_{red}}$)

Cluster	$\mathrm{Bgc_{red}}$ [$\mathrm{Mpc^{1.77}}$]	M_{200} [10^{14} $\mathrm{M_\odot}$]	T_X [keV]	R_{200} [Mpc]
RCS0224-0002	802 ± 184	5 ± 2	5 ± 1	1.7 ± 0.2
RCS1324+2845	1632 ± 360	14 ± 6	10 ± 3	$2.5^{+0.4}_{-0.3}$
RCS1326+2903	435 ± 164	1.7 ± 1	2 ± 1	1.2 ± 0.3
($z = 0.93$)	1600 ± 354	14^{+6}_{-5}	10 ± 3	$2.5^{+0.4}_{-0.3}$
RCS1419+5326	1273 ± 221	11 ± 4	8 ± 2	2.2 ± 0.3
RCS1620+2929	729 ± 187	4 ± 2	4 ± 1	1.6 ± 0.3

5.4.2 SZ Masses

If one assumes hydrostatic equilibrium, negligible nonthermal processes, spherical symmetry, and isothermal gas, the total mass of a cluster inside a radius r can be inferred from the modeled cluster properties:

$$M(r) = \frac{3k_B T_e \beta}{G\mu m_p} \frac{r^3}{r_c^2 + r^2} \tag{5.7}$$

where μm_p is the mean molecular weight of the gas. Given an electron temperature derived from X-ray observations, one can combine cluster parameters such as those quoted in Table 5.4 with eq. 5.7 and eq. 5.3 to estimate gas mass fraction as a function of radius. In an analysis of eighteen clusters observed with the OVRO and BIMA arrays, Grego et al. (2001) [66] find a mean gas mass fraction of $f_g = 0.081^{+0.009}_{-0.011}\ h^{-1}_{100}$ at a fiducial radius $\mathrm{R_{500}}$.

The analysis of the RCS clusters was worked backward from the gas mass analysis as in Joy et al. (2001) [78]. For each cluster, the relative likelihood function is determined over a range of values for the parameter ΔT_0 (Reese et al. 2002 [101]). In order to simplify the analysis, θ_c is held fixed at $12''$ and β is held fixed at 0.66 (Henry et al. 1993 [71]). To test the assumption that the constraint on this shape parameter would not systematically bias the results, the estimates for mass and electron temperature

Table 5.6. SZ Results for Cluster Mass and Electron Temperatures Using R_{200} ($\mathrm{Bgc_{red}}$)

Field	T_e [keV]	Virial Mass [10^{14} $M_\odot$]	Gas Mass [10^{13} $M_\odot$]
RCS0224-0002	$6.6^{+0.7}_{-0.8}$	$5.0^{+0.5}_{-0.6}$	$3.6^{+0.4}_{-0.4}$
RCS1324+2845[a]	< 2.1	< 2.5	< 2.0
RCS1326+2903	5^{+1}_{-1}	$2.5^{+0.5}_{-0.7}$	$1.9^{+0.4}_{-0.5}$
($z = 0.93$)	5^{+1}_{-1}	6^{+1}_{-2}	$4.5^{+0.9}_{-1}$
RCS1419+5326[a]	3.9 (< 7.7)	3.8 (< 7.5)	2.9 (< 5.7)
RCS1620+2929[a]	3.3 (< 6.3)	2.4 (< 4.6)	1.9 (< 3.7)

[a]95% confidence limits

were compared for different values of θ_c ranging from 5″ to 18″ for each cluster. The estimates of mass and electron temperature were consistent over the entire range of θ_c indicating that the assumption $\theta_c = 12''$ is sufficient for this analysis.

A gas mass fraction of $f_g = 0.081\ h_{100}^{-1}$ (Grego et al. 2001 [66]) is assumed, in order to derive estimates for cluster properties. From each value of ΔT_0 in the grid, a value for electron temperature (T_e), virial mass (M_v), and gas mass (M_g) is computed with an associated probability. For the clusters RCS0224 and RCS1326, 68% confidence intervals are given. For the clusters RCS1324, RCS1419, and RCS1620, the 68% confidence intervals would include the null detection. In the case of these three clusters, 95% upper limits are reported. Masses are calculated inside a radius of R_{200} from the cluster center using the value for R_{200} reported in Table 2.5. The resulting likelihood function is then used to describe the best fit parameters for T_e, M_v and M_g. Results are found in Table 5.6 for the case of $\theta_c = 12''$, $\beta = 0.66$, and $f_g = 0.081\ h_{100}^{-1}$.

5.4.3 X-ray Mass Estimates

The gas mass density distribution of a cluster of galaxies whose surface brightness profile is well described by a β model can be shown to take the form of Equation 5.1. This

Table 5.7. X-ray Mass Estimate Input Parameters

Cluster	kT [keV]	R_{core} [arcsec]	β	I_0 [a]
RCS0224-0002	$4.31^{+1}_{-0.6}$	24^{+2}_{-1}	$0.71^{+0.05}_{-0.04}$	$8.5^{+0.6}_{-0.5}$
RCS1326+2903	$1.3^{+1}_{-0.2}$	$13.6^{+1}_{-0.8}$	$0.51^{+0.04}_{-0.03}$	$3.80^{+0.07}_{-0.6}$
($z = 0.93$)	$1.5^{+1}_{-0.2}$	$13.6^{+1}_{-0.8}$	$0.51^{+0.04}_{-0.03}$	$3.80^{+0.07}_{-0.6}$
RCS1419+5326	$4.0^{+2}_{-0.6}$	$8.9^{+0.7}_{-0.6}$	$0.61^{+0.03}_{-0.02}$	185^{+14}_{-11}
RCS1620+2929	$3.5^{+5}_{-0.7}$	$7.6^{+0.6}_{-0.5}$	$0.56^{+0.03}_{-0.03}$	22^{+2}_{-1}

[a]Surface brightness I in units of 10^{-9} photons sec^{-1} cm^{-2} arcsec^{-2}

relationship is dependent upon the assumptions of hydrostatic equilibrium, spherical symmetry, and gas isothermality. Central gas densities (n_0) can be determined from cluster X-ray luminosities. This calculation requires the experimental determination of both gas temperature and emission measure, which is performed with the spectral fitting package XSPEC (Arnaud 1996 [8]).

Using the results of spectral fitting and β model fitting performed in Chapter 3, along with Equation 5.1, and the equation of hydrostatic equilibrium (Equation 2.3) gas mass and total mass were calculated out to R_{200}, assuming T(r)=T. Parameters used in the mass calculations can be seen in Table 5.7, and the resulting mass estimates are given in Table 5.8.

Table 5.8. X-ray Mass Estimates for R < R_{200} ($\mathrm{Bgc_{red}}$)

Cluster	n_0 [10^{-1} cm^{-3}]	M_{gas} [10^{13} h_{70}^{-1} $M_\odot$]	M_{tot} [10^{14} h_{70}^{-1} $M_\odot$]	f_{gas} [h_{70}^{-1}]
RCS0224-0002	$0.0150^{+0.0005}_{-0.0005}$	$1.7^{+0.3}_{-0.3}$	$6.8^{+0.9}_{-1}$	$0.025^{+0.006}_{-0.006}$
RCS1326+2903	$0.0136^{+0.0005}_{-0.0005}$	$1.0^{+0.2}_{-0.1}$	$1.3^{+0.3}_{-0.3}$	$0.08^{+0.02}_{-0.02}$
($z = 0.93$)	$0.0133^{+0.0005}_{-0.0005}$	$3.3^{+0.6}_{-0.6}$	$3.1^{+0.7}_{-0.7}$	$0.11^{+0.03}_{-0.03}$
RCS1419+5326	$0.107^{+0.003}_{-0.003}$	$4.1^{+0.7}_{-0.6}$	7^{+1}_{-1}	$0.06^{+0.01}_{-0.01}$
RCS1620+2929	$0.040^{+0.001}_{-0.001}$	$1.4^{+0.3}_{-0.2}$	6^{+2}_{-2}	$0.023^{+0.009}_{-0.008}$

5.5 Mass Comparisons

Mass estimates from the three methods (optical richness, SZ, and X-ray) were compared, using the most likely redshift of RCS1326+2903 ($z = 0.71$) for weighted average calculations. Results of these comprisons are listed in Table 5.9. In general there is at best marginal agreement between the three methods, with $\mathrm{B_{gc,red}}$ predicting the highest masses, followed by X-ray, and then SZ. There is also a discrepancy between the gas masses predicted by SZ and X-ray analysis, with SZ estimates being higher than those of the X-ray by a factor of 1.6.

Because SZ total mass goes as $f_g^{-1/2}$, and SZ gas mass goes as $f_g^{1/2}$, we find that discrepancies between X-ray and SZ masses are highly dependent upon the particular gas mass fraction used by the SZ analysis. We have used these simple relationships to estimate the agreement between SZ and X-ray masses if their gas mass fractions were coincident, and find that there is much better agreement. Estimates of how the mass ratios would change if the X-ray value for f_g were used are given in Table 5.10.

5.6 Summary and Discussion

SZ mass limits are systematically lower than what was expected given the optical richness of these clusters listed in Table 2.5, with mass discrepancies ranging

Table 5.9. Mass Comparisons

Cluster	$M_{SZ}/M_{Bgc_{red}}$	$M_{X-ray}/M_{Bgc_{red}}$	M_{SZ}/M_{X-ray}	$M_g(SZ)/M_g(X\text{-ray})$
RCS0224-0002	$1.1^{+0.5}_{-0.5}$	$1.5^{+0.7}_{-0.7}$	$0.7^{+0.1}_{-0.1}$	$2.1^{+0.4}_{-0.4}$
RCS1324+2845	$0.2_{-0.2}$	...	...	...
RCS1326+2903	$1.5^{+0.9}_{-1}$	$0.8^{+0.5}_{-0.5}$	$1.9^{+0.6}_{-0.7}$	$1.9^{+0.6}_{-0.5}$
($z = 0.93$)	$0.4^{+0.2}_{-0.2}$	$0.2^{+0.1}_{-0.1}$	$1.9^{+0.5}_{-0.8}$	$1.4^{+0.4}_{-0.4}$
RCS1419+5326	$0.4^{+0.2}_{-0.4}$	$0.7^{+0.3}_{-0.2}$	$0.5^{+0.2}_{-0.5}$	$0.7^{+0.3}_{-0.7}$
RCS1620+2929	$0.6^{+0.4}_{-0.7}$	$1.6^{+1}_{-0.9}$	$0.4^{+0.2}_{-0.4}$	$1.4^{+0.6}_{-1.4}$
Weighted mean[a]	0.83 ± 0.08	0.8 ± 0.2	0.7 ± 0.1	1.6 ± 0.3

[a]Calculated using the $z = 0.71$ RCS1326+2903 mass estimates

Table 5.10. f_g Corrected Mass Comparisons

Cluster	$M_{SZ}/M_{Bgc_{red}}$	M_{SZ}/M_{X-ray}	$M_g(SZ)/M_g(X\text{-ray})$
RCS0224-0002	$2.1^{+0.9}_{-0.9}$	$1.6^{+0.3}_{-0.3}$	$0.98^{+0.2}_{-0.2}$
RCS1326+2903	2^{+1}_{-1}	$2.3^{+0.7}_{-0.8}$	$1.6^{+0.5}_{-0.4}$
($z = 0.93$)	$0.4^{+0.2}_{-0.2}$	$2.0^{+0.6}_{-0.8}$	$1.3^{+0.4}_{-0.4}$
RCS1419+5326	$0.5^{+0.5}_{-0.5}$	$0.8^{+0.7}_{-0.8}$	$0.5^{+0.5}_{-0.5}$
RCS1620+2929	1^{+1}_{-1}	$0.9^{+0.9}_{-0.9}$	$0.6^{+0.6}_{-0.6}$
Weighted mean[a]	1.0 ± 0.4	1.5 ± 0.2	1.0 ± 0.2

[a]Calculated using the $z = 0.71$ RCS1326+2903 mass estimates

from $10 - 80\%$. Optical richness and SZ temperature estimates are more consistent, agreeing within errors in all clusters except for RCS1324+2845 and the case in which RCS1326+2903 is at $z = 0.93$. It remains clear however, that there are significant inconsistencies between the $B_{gc,red}$ estimates of cluster properties and independent SZ estimates of cluster properties. We also note that, at least for this sample, strong gravitational lensing does not portend a strong SZ signal.

X-ray derived masses are less systematically inconsistent with optical richness predictions, providing higher masses in the case of two clusters (RCS0224-0002 and RCS1620+2929) and lower masses for the other two clusters (RCS1326+2903 and RCS1419+5326). Overall mass discrepancies range from $20 - 60\%$, however all masses do agree within confidence limits (except for the case in which RCS1326+2903 is at $z = 0.93$, which is highly unlikely given the position of the peak of X-ray emission). While in every case $B_{gc,red}$ predicted temperatures are higher than fitted X-ray temperatures, all values agree within 68% confidence limits.

Given the results of Chapter 3 (in particular Figure 3.13), we expect optical richness to overestimate both the masses and temperatures of high redshift clusters. This effect should be particularly evident in this case, where we have used calibrations from the medium redshift CNOC sample to provide mass estimations which are independent of our (X-ray) knowledge of this sample. The evidence that SZ masses are also significantly lower than $B_{gc,red}$ estimated masses lends credence to our conviction that redshift trends in the mass estimations of optical richness must be corrected for before this parameter can function as a reliable estimator of cluster properties.

SZ and X-ray mass estimates are relatively inconsistent, with X-ray masses appearing systematically higher in most cases. This discrepancy is likely due to an overestimation of gas mass fractions in the SZ analysis. If lower gas mass fractions had been used, SZ derived gas masses would be lower and SZ derived total masses would be higher, resulting in significantly better agreement in both cases with X-ray derived values. In addition, the correlation between optical richness and cluster mass used in this analysis has been normalized from an X-ray selected sample of galaxy clusters. This could contribute to optical richness predictions being, overall, more consistent with X-ray results.

Our X-ray analysis indicates that the gas mass fractions of these clusters are significantly lower than is expected for a universal baryon fraction (Evrard 1997 [48]). This characteristic is also seen in groups, poor clusters, and other high redshift samples (Dell'Antonio et al. 1995 [26]; Sanderson et al. 2003 [106]; Sadat et al. 2005 [105]). Because of these combined results, and evidence that SZ and X-ray masses are better aligned when there is agreement between gas mass fractions, we conclude that assuming a constant gas mass fraction in the SZ analysis of cluster mass is ill-advised. In addition, these findings indicate that to function as an accurate predictor of cluster mass, SZ results need to be calibrated via additional methods of mass estimation.

Chapter 6

Summary and Conclusions

For this thesis, we have obtained X-ray temperatures, masses, and luminosities for a sample of 20 clusters of galaxies observed with the Chandra X-ray Observatory, spanning a redshift range of $0.17 < z < 1.07$. We have used these data, in combination with additional data gained through both the literature and scientific collaborations, to compare independent methods of mass estimation, examine correlations between cluster properties and optical richness, and characterize the properties of high redshift optically selected clusters. The notable results from this research are summarized below.

6.1 Cluster Mass Estimators

In chapters 2 and 5 we compare our X-ray derived masses to the findings of a number of alternate mass estimation techniques, including dynamical, weak lensing, and SZ methods. Our main results can be summarized as follows:

- X-ray and dynamical masses show very good agreement, however there is a significant amount of scatter in mass ratios ($\sim 30\%$), due primarily to substructure and non-gravitational processes (Bird 1994 [15]).

- Weak lensing mass estimates are systematically higher than X-ray masses by 10-20%, possibly caused by additional mass concentrations along the line of sight. This effect is well documented in the literature and is almost certainly due to superpositions along the line of sight (Cen 1997 [23]; Floor & Evrard [50]; Hoekstra 2003 [76]).

- X-ray and SZ masses are well aligned when there is agreement between gas mass fractions. In concert with indications that high redshift clusters are prone to exhibiting low gas mass fractions, this indicates that to function as a reliable tracer of cluster mass, SZ results must first be calibrated by the results of alternate mass estimation methods.

6.2 Cluster Properties and Optical Richness

In chapters 2 and 3 we attempt to calibrate red-sequence optical richness ($B_{gc,red}$) as an estimator of global cluster properties. In chapter 5 we use our medium redshift ($0.17 < z < 0.55$) calibrations to predict the temperatures and masses of high redshift ($z > 0.6$) optically selected clusters, and then compare these predictions to X-ray and SZ derived values. We present the results of these investigations below:

- At medium redshift, $B_{gc,red}$ correlates well with X-ray temperature. There is significantly more scatter in $B_{gc,red}$-Mass and $B_{gc,red}$-R_{200}, though overall one does see a trend. L_X and $B_{gc,red}$ are poorly correlated even at these redshifts.

- After adding high redshift clusters to the calibration sample, one still sees a fair relationship between $B_{gc,red}$ and T_X. It is apparent, however, that optical richness begins to overestimate the temperatures of high-z clusters, indicating the redshift-dependent nature of these discrepancies.

- $B_{gc,red}$ consistently over estimates both R_{200} and L_X for high redshift clusters. In the case of X-ray luminosity, it is a particularly poor estimator, confirming that galactic overdensity is more closely correlated to dark matter density than to intracluster gas density. This idea is supported by indications that $B_{gc,red}$

measurements are affected by the higher concentration of dark matter density profiles at high redshift.

- Optical richness measurements predict masses which are systematically higher than both X-ray and SZ mass estimates by $\sim 20\%$. The overestimation of cluster mass by optical richness is an increasing function of redshift which reaches a factor of ~ 1.4 by a redshift of $z \sim 0.8$. Contributions to this effect include uncertainties in the evolution of the cluster luminosity function, and changes in dark matter density profiles with redshift (Hiotelis 2003 [75]; Del Popolo 2001 [99]). Calibration of these effects would contribute greatly to the establishment of optical richness as a robust mass estimator, allowing an efficient means of determining the evolution of the cluster mass function and placing precise constraints on cosmological models.

6.3 Characteristics of High Redshift Optically Selected Clusters

The Red-sequence Cluster Survey has produced the largest high redshift cluster catalogue to date. This work presents the results of the very first X-ray follow up observations of these objects. Through it we have laid the groundwork for the calibration of future large area optical and SZ surveys. Once calibrated, these surveys will place important constraints on theoretically crucial cosmological parameters, through exploration of the evolution of the most massive virialized structures in the universe.

The X-ray properties of high redshift optically selected clusters are investigated in chapters 3 and 4. One of the main themes we have seen is that RCS clusters have systematically lower temperatures, masses, and luminosities than X-ray selected samples. This is not entirely surprising, given the similar results of other recent optical cluster surveys (PDCS, Postman et al. 1996 [100]; ROXS, Donahue et al. 2002 [31]). Factors which may contribute to this discrepancy, along with some of the characteristic properties of our high redshift sample are given below:

- X-ray surveys select based on luminosity, and X-ray luminosity is an increasing function of both mass and temperature, therefore X-ray surveys are more likely to pick out high mass, high gas density systems. This selection effect should not be a problem for cosmological applications, however it curtails our ability to study the entire spectrum of the cluster distribution.

- Though the red-sequence technique has minimized contamination due to galaxy projections along the line of sight, this effect remains a problem both in systems that contain closely spaced groups of galaxies and in filamentary structures. This is evidenced by the three clusters in our sample which were only marginally detected in the X-ray and RCS0439-2904 which is a known superposition of 2-3 closely spaced structures.

- The $L_X - T_X$ and Mass$-T_X$ relationships of RCS clusters are best fit with steeper slopes than are expected based on theory (Voit 2004 [116]). This indicates negative redshift evolution in these relationships, suggesting that systems at higher redshift have lower virialized masses and X-ray luminosities than expected for their given temperatures, probably owing to the influence of galaxy formation on these systems (Voit 2004 [116]). This result was also found by Ettori et al. 2004 [46]. Our current data is not robust enough to accurately constrain a model for this evolution.

- RCS clusters have lower than expected gas mass fractions, implying that they are high entropy systems. This property is seen in groups, poor clusters, and other high redshift objects (Dell'Antonio et al. 1995 [26]; Sanderson et al. 2003 [106]; Sadat et al. 2005 [105]). Two likely sources of energy injection for these high redshift systems are galaxy formation and AGN heating.

- AGN contributions to the energy of RCS0224-0002 could make up $\sim 10\%$ of the energy in the gas within R_{200}. This added energy raises the entropy of the system and is a contributing factor to the observed low gas mass fraction of the cluster, along with probable additional contributions from galaxy formation.

- From our detailed analysis of RCS0224-0002, we have collected ample evidence that the cluster is in a state of dynamical relaxation, indicating that substructure within the cluster is unlikely to be the cause of enhanced gravitational lensing. We conclude that the boosted lensing cross section of this cluster is a result of superposition. Due to the propensity for the RCS survey to detect closely spaced structures along the line of sight, it is likely that this selection effect is partially responsible for the high incidence of strong gravitational lensing found in the RCS sample.

- RCS0224-0002 shows evidence of a proto-cooling core. Identical results for an object at similar redshift ($z \sim 0.8$) were found by Grego et al. 2004 [67]. These two objects are arguably the only clusters with cooling cores to have been discovered at these redshifts, however their existence indicates that clusters are beginning to become more quiescent at redshifts of $z \sim 1$. This finding suggests that the RCS survey is discovering both objects which are still in the process of formation and also clusters which have formed at early times (and have since remained relatively undisturbed), suggesting that optical selection is indeed well suited for collecting a broad subset of the cluster distribution.

6.4 Future Prospects

The findings of this study indicate a number of possibilities for follow-up work in the area of high redshift clusters. One is parameterization of the overestimation of mass by optical richness as a functions of redshift, which will be necessary before

$B_{gc,red}$ can become a reliable estimator of cluster masses at high-z. Another important investigation will be to determine AGN contributions to cluster entropy for the entirety of the X-ray observed RCS sample, which could either confirm or rule out AGN energy injection as a major contributor to the low gas fractions of these objects. Finally, the observation of more RCS clusters in the X-ray, along with procuring longer observations of the clusters in our current sample, is necessary for placing stronger constraints on the relationships investigated here and providing a more thorough understanding of these fascinating objects.

Bibliography

[1] G. O. Abell. The Astrophysical Journal, 3:221, 1958.

[2] S. W. Allen. Monthly Notices of the Royal Astronomical Society, 315:269, 2000.

[3] S. W. Allen and A. C. Fabian. Monthly Notices of the Royal Astronomical Society, 297:L57, 1998.

[4] S. W. Allen, R. W. Schmidt, and A. C. Fabian. Monthly Notices of the Royal Astronomical Society, 328:L37, 2001.

[5] S. W. Allen, R. W. Schmidt, and A. C. Fabian. Monthly Notices of the Royal Astronomical Society, 334:11, 2002.

[6] P. Anninos and M. L. Norman. The Astrophsical Journal, 459:12, 1996.

[7] J. S. Arabadjis, M. W. Bautz, and G. P. Garmire. The Astrophysical Journal, 572:66, 2002.

[8] K. A. Arnaud. ADASS, 101:5, 1996.

[9] K. A. Arnaud and A. E. Evrard. Monthly Notices of the Royal Astronomical Society, 305:631, 1999.

[10] H. Boringer at al. Astrophysical Journal Supplements, 129:435, 2000.

[11] N. A. Bahcall, X. Fan, and R. Cen. The Astrophysical Journal, 485:L53, 1997.

[12] N. A. Bahcall, J. P. Ostriker, S. Perlmutter, and P.J Steinhardt. Science, 284:1481, 1999.

[13] F. E. Bauer, D. M. Alexander, W. N. Brandt, A. E. Hornschemeier, T. Miyajl, G. P. Garmire, D. P. Schneider, M. W. Bautz, G. Chartas, R. E. Griffiths, and W. L. W. Sargent. The Astronomical Journal, 123:1163, 2002.

[14] B. A. Benson, S. E. Church, P. A. R. Ade, J. J. Bock, K. M. Ganga, C. N. Henson, and K. L. Thompson. The Astrophysical Journal, 617:829, 2004.

[15] C. M. Bird, R. F. Mushotzky, and C. A. Metzler. The Astrophysical Journal, 453:40B, 1995.

[16] H. Bohringer, Y. Tanaka, R. F. Mushotzky, Y. Ikebe, and M. Hattori. Astronomy and Astrophysics, 334:789, 1998.

[17] M. Bonamente, M. K. Joy, J. E. Carlstrom, and submitted to The Astrophysical Journal S. J. LaRoque. astroph/0403016, 2004.

[18] S. Borgani, M. Girardi, R. G. Carlberg, H. K. C. Yee, and E. Ellingson. The Astrophysical Journal, 527:561, 1999.

[19] E. T. Byram, T. A. Chubb, and H. Friedman. Science, 152:66, 1966.

[20] R. G. Carlberg, H. K. C. Yee, E. Ellingson, R. Abraham, P. Gravel, S. Morris, and C. J. Pritchet. The Astrophysical Journal, 462:32, 1996.

[21] J. E. Carlstrom, G. P. Holder, and E. D. Reese. Annual Review of Astronomy and Astrophysics, 40:643, 2002.

[22] A. Cavaliere and R. Fusco-Femiano. Astronomy and Astrophysics, 49:137, 1976.

[23] R. Cen. The Astrophysical Journal, 485:39, 1997.

[24] J. J. Condon, W. D. Cotton, E. W. Greisen, Q. F. Yin, R. A. Perley, G. B. Taylor, and J. J. Broderick. The Astronomical Journal, 115:1693, 1998.

[25] M. Davis and P. J. E. Peebles. The Astrophysical Journal, 294:70, 1983.

[26] I. P. Dell'Antonio, M. J. Geller, and D. G. Fabricant. The Astronomical Journal, 110:502, 1995.

[27] R. P. Van der Marel, J. Magorrian, R. G. Carlberg, H. K. C. Yee, and E. Ellingson. The Astrophysical Journal, 119:2038, 2000.

[28] J. M. Dickey and F. J. Lockman. Annual Reviews of Astronomy and Astrophysics, 28:215, 1990.

[29] M. Donahue, J. A. Gaskin, S. K. Patel, M. Joy, D. Clowe, and J. P. Hughes. The Astrophysical Journal, 598:190, 2003.

[30] M. Donahue, J. Mack, and C. Scharf et al. Astrophysical Journal Letters, 552:93, 2001.

[31] M. Donahue, C. Scharf, and J. Mack et al. The Astrophysical Journal, 569:689, 2002.

[32] M. Donahue, J. T. Stocke, and I. M. Gioia. The Astrophysical Journal, 385:49, 1992.

[33] T. M. D. Ebbels, J. F. Le Borgne, R. Pello, R. S. Ellis, J. P. Kneib, I. Smail, and B. Sanahuja. Monthly Notices of the Royal Astronomical Society, 281:L75, 1996.

[34] H. Ebeling, A. C. Edge, H. Bohringer, S. W. Allen, C. S. Crawford, A. C. Fabian, W. Vogues, and J. P. Huchra. Monthly Notices of the Royal Astronomical Society, 301:881, 1998.

[35] A. Edge and G. Stewart. Monthly Notices of the Royal Astronomical Society, 252:428, 1991.

[36] V. R. Eke, S. Cole, and C. S. Frenk. Monthly Notices of the Royal Astronomical Society, 282:263, 1996.

[37] V. R. Eke, S. Cole, C. S. Frenk, and J. P. Henry. Monthly Notices of the Royal Astronomical Society, 298:1145, 1998.

[38] V. R. Eke, J. Navarro, and C. S. Frenk. The Astrophysical Journal, 503:569, 1998a.

[39] A. K. Romer et al. Astrophysical Journal Supplements, 126:209, 2000.

[40] G. Soucail et al. Astronomy and Astrophysics, 191:L19, 1988.

[41] M. Elvis et al. Astrophysical Journal Supplements, 95:1, 1994.

[42] S. De Grandi et al. The Astrophysical Journal, 514:148, 1999.

[43] S. Ettori. Monthly Notices of the Royal Astronomical Society, 311:313, 2000.

[44] S. Ettori, S. De Grandi, and S. Molendi. Astronomy and Astrophysics, 391:841, 2002.

[45] S. Ettori and M. Lombardi. Astronomy and Astrophysics, 398:5, 2003.

[46] S. Ettori, P. Tozzi, S. Borgani, and P. Rosati. Astronomy and Astrophysics, 417:13, 2004.

[47] A. Evrard. The Astrophysical Journal, 363:349, 1990.

[48] A. E. Evrard. Monthly Notices of the Royal Astronomical Society, 292:289, 1997.

[49] A. E. Evrard, C. A. Metzler, and J. F. Navarro. The Astrophysical Journal, 469:494, 1996.

[50] S. N. Floor and A. E. Evrard. Systematic errors in weak lensing cluster mass estimates. In 205th Meeting of the American Astronomical Society, number 148.09. AAS, 2004.

[51] H. Ford, M. Postman, and J. P. Blakeslee et al. astroph/0408165, 2004.

[52] M. Franx, G. D. Illingworth, D. D. Kelson, P. G. van Dokkum, and K. V. Tran. The Astrophysical Journal, 486:L75, 1997.

[53] C. S. Frenk, S. D. M. White, G. Efstathiou, and M. Davis. The Astrophysical Journal, 351:10, 1990.

[54] M. Fukugita, C. J. Hogan, and P. J. E. Peebles. The Astrophysical Journal, 503:518, 1998.

[55] N. Gehrels. The Astrophysical Journal, 303:336, 1986.

[56] D. G. Gilbank, R. G. Bower, and F. J. Castander et al. Monthly Notices of the Royal Astronomical Society, 348:551, 2004.

[57] I. M. Gioia, J. P. Henry, T. Maccacaro, S. L. Morris, J. T. Stocke, and A. Wolter. The Astrophysical Journal, 356:L35, 1990.

[58] I. M. Gioia, T. Maccacaro, R. E. Schild, A. Wolter, J. T. Stocke, S. L. Morris, and J. P. Henry. Astrophysical Journal Supplements, 72:567, 1990.

[59] M. Girardi, S. Borgani, G. Giuricin, F. Mardirossian, and M. Mezzetti. The Astrophysical Journal, 530:62, 2000.

[60] M. D. Gladders. The red sequence technique and high-redshift galaxy clusters. In Clusters of Galaxies: Probes of Cosmological Structure and Galaxy Evolution, 2004.

[61] M. D. Gladders, H. Hoekstra, H. K. C. Yee, P. B. Hall, and L. F. Barrientos. The Astrophysical Journal, 593:48, 2003.

[62] M. D. Gladders and H. K. C. Yee. The Astronomical Journal, 120:2148, 2000.

[63] M. D. Gladders and H. K. C. Yee. Astrophysical Journal Supplements, 157:1, 2005.

[64] M. D. Gladders, H. K. C. Yee, and E. Ellingson. The Astronomical Journal, 123:1, 2002.

[65] C. Golse, J. P. Kneib, and G. Soucail. astroph/0103500, 2001.

[66] L. Grego, J. E. Carlstrom, E. D. Reese, G. P. Holder, W. L. Holzapfel, M. Joy, J. J. Mohr, and S. Patel. The Astrophysical Journal, 552:2, 2001.

[67] L. Grego, J. M. Vrtilek, L. Van Speybroek, L. P. David, W. Forman, J. E. Carlstrom, E. D. Reese, and M. K. Joy. The Astrophysical Journal, 608:731, 2004.

[68] Z. Haiman, J. J. Mohr, and G. P. Holder. The Astrophysical Journal, 553:545, 2001.

[69] J. P. Henry. Astrophysical Journal Letters, 489:L1, 1997.

[70] J. P. Henry. The Astrophysical Journal, 609:603, 2004.

[71] J. P. Henry, U. G. Briel, and P. E. Nulsen. Astrononomy and Astrophysics, 271:413, 1993.

[72] J. P. Henry, I. M. Gioia, T. Maccacaro, S. L. Morris, J. T. Stocke, and A. Wolter. The Astrophysical Journal, 386:408, 1992.

[73] A. K. Hicks, E. Ellingson, M. Bautz, H. K. C. Yee, M. Gladders, and G. Garmire. astroph/0410167, 2004.

[74] P. Hickson. The Astrophysical Journal, 255:382, 1982.

[75] N. Hiotelis. Extended press-schecter theory and the density profiles of dark matter haloes. Monthly Notices of the Royal Astronomical Society, 344:149, 2003.

[76] H. Hoekstra. Monthly Notices of the Royal Astronomical Society, 339:1155, 2003.

[77] W. S. Holland, C. R. Cunningham, W. K. Gear, T. Jenness, K. Laidlaw, J. F. Lightfoot, and E. I. Robson. SPIE, 3357:305, 1998.

[78] M. Joy, S. J. LaRoque, L. Grego, J. E. Carlstrom, K. S. Dawson, H. Ebeling, W. L. Holzapfel, D. Nagai, and E. D. Reese. The Astrophysical Journal, 551:L1, 2001.

[79] N. Kaiser and G. Squires. The Astrophysical Journal, 404:441, 1993.

[80] I. King. The Astronomical Journal, 67:471, 1962.

[81] J. P. Kneib, Y. Mellier, B. Fort, and G. Mathez. Astronomy and Astrophysics, 273:367, 1993.

[82] E. S. Levine, A. E. Schulz, and M. White. The Astrophysical Journal, 577:569, 2002.

[83] A. D. Lewis, E. Ellingson, S. L. Morris, and R. G. Carlberg. The Astrophysical Journal, 517:587, 1999.

[84] M. S. Longair and M. Seldner. Monthly Notices of the Royal Astronomical Society, 189:433, 1979.

[85] L. M. Lubin, J. S. Mulchaey, and M. Postman. Astrophysical Journal Letters, 601:9, 2004.

[86] R. Lynds and V. Petrosian. Large scale structures of the universe. In 130th Symposium of the IAU, number 467 in 130. IAU, 1988.

[87] M. Markevitch. The Astrophysical Journal, 504:27, 1998.

[88] P. Martini, D. D. Kelson, J. S. Mulchaey, and S. C. Trager. astroph/0208017, 2002.

[89] H. Matsumoto, T. G. Tsuru, Y. Fukazawa, M. Hattori, and D. S. Davis. PASJ, 52:153, 2000.

[90] Herman Melville. Moby Dick; or, The Whale. Harper and Brothers, New York, 1851.

[91] R. J. Mitchell, J. L. Culhane, P. J. N. Davison, and J. C. Ives. Monthly Notices of the Royal Astronomical Society, 175:29P, 1976.

[92] mohr. J. j. mohr and e. d. reese and e. ellingson and a. d. lewis and a. e. evrard. The Astrophysical Journal, 544:109, 2000.

[93] A. Moretti, D. Campana, D. Lazzati, and G. Tagliaferri. The Astrophysical Journal, 588:696, 2003.

[94] R. F. Mushotzky and Loewenstein. The Astrophysical Journal, 481:63, 1997.

[95] J. F. Naavarro, C. S. Frenk, and S. D. M. White. The Astrophysical Journal, 490:493, 1997.

[96] J. Navarro, C. S. Frenk, and S. D. M. White. Monthly Notices of the Royal Astronomical Society, 275:720, 1995.

[97] D. M. Neumann and H. Bohringer. Monthly Notices of the Royal Astronomical Society, 289:123, 1997.

[98] J. M. O'Meara, D. Tyler, D. Kirkman, N. Suzuki, J. X. Prochaska, D. Lubin, and A. M. Wolfe. The Astrophysical Journal, 552:718, 2001.

[99] A. Del Popolo. Monthly Notices of the Royal Astronomical Society, 325:1190, 2001.

[100] M. Postman, L. M. Lubin, and J. E. Gunn et al. The Astronomical Journal, 111:615, 1996.

[101] E. D. Reese, J. E. Carlstrom, M. Joy, J. J. Mohr, L. Grego, and W. L. Holzapfel. The Astrophysical Journal, 581:53, 2002.

[102] D. Richstone, A. Loeb, and E. L. Turner. The Astrophysical Journal, 393:477, 1992.

[103] P. Rosati, R. Della Ceca, C. Norman, and R. Giacconi. The Astrophysical Journal, 492:L21, 1998.

[104] J. T. Ruderman and H. Ebeling. The Astrophysical Journal, 623:L81, 2005.

[105] R. Sadat, A. Blanchard, S. C. Vauclair, D. H. Lumb, J. Bartlett, A. K. Romer, J. P. Bernard, M. Boer, P. Marty, J. Nevalainen, D. J. Burke, C. A. Collins, and R. C. Nichol. Astronomy and Astrophysics, 437:31, 2005.

[106] A. J. R. Sanderson, T. J. Ponman, A. Finoguenov, E. J. Lloyd-Davies, and M. Markevitch. The birmingham-cfa cluster scaling project - i. gas fraction and the m-t_x relation. Monthly Notices of the Royal Astronomical Society, 340:989, 2003.

[107] C. L. Sarazin. X-ray Emissions from Clusters of Galaxies. Cambridge University Press, Cambridge, 1988.

[108] P. Schecter. The Astrophysical Journal, 203:297, 1976.

[109] S. Schindler. Astronomy and Astrophysics, 305:756, 1996.

[110] R. A. Sunyaev and Y. B. Zeldovich. Astroph. Sp. Sci., 7:3, 1970.

[111] R. C. Thomas and R. Kantowski. astroph/0003463, 2004.

[112] J. Tyson, F. Valdes, and R. Wenk. The Astrophysical Journal, 349:L19, 1990.

[113] J. A. Tyson, G. P. Kochanski, and I. P. dell'Antonio. The Astrophysical Journal, 498:107L, 1998.

[114] I Valtchanov, M. Pierre, J. Willis, S. Dos Santos, L. Jones, S. Andreon, C. Adami, B. Altieri, M. Bolzonella, M. Bremer, P. A. Duc, E. Gosset, C. Jean, and J. Surdej. Astronomy and Astrophysics, 423:75, 2004.

[115] A. Vikhlinin, B. R. McNamara, W. Forman, C. Jones, H. Quintana, and A. Hornstrup. The Astrophysical Journal, 502:558, 1998.

[116] G. M. Voit. astroph/0410173, 2004.

[117] T. M. A. Webb, H. K. C. Yee, R. J. Ivison, H. Hoekstra, M. D. Gladders, L. F. Barrientos, and in prep B. C. Hsieh. 2005.

[118] R. Weymann. Phys. Fluids, 8:2112, 1965.

[119] D. A. White, C. Jones, and W. Forman. Monthly Notices of the Royal Astronomical Society, 292:419, 1997.

[120] S. D. M. White, J. F. Navarro, A. E. Evrard, and C. S. Frenk. Nature, 366:429, 1993.

[121] B. Wilkes, P. Green, R. Cameron, N. Evans, H. Ghosh, D. W. Kim, and H. Tananbaum. The chandra multi-wavelength project (champ): a serendipitous x-ray survey using chandra archival data. In Meeting of the High Energy Astrophysics Division, number 5.2105W. HEAD, 2000.

[122] L. L. R. Williams, J. F. Navarro, and M. Bartelmann. The Astrophysical Journal, 527:535, 1999.

[123] X. P. Wu, T. Chiueh, L. Z. Fang, and Y. J. Xue. Monthly Notices of the Royal Astonomical Society, 301:861, 1998.

[124] H. K. C. Yee and E. Ellingson. The Astrophysical Journal, 585:215, 2003.

[125] H. K. C. Yee and E. Ellingson. The Astrophysical Journal, 585:215, 2003.

[126] H. K. C. Yee and O. A. Lopez-Cruz. The Astronomical Journal, 117:1985, 1999.

[127] F. Zwicky. The Astrophysical Journal, 86:217, 1937.

[128] F. Zwicky, E. Herzog, M. Karpowicz, C. T. Kowal, and P. Wild. Catalogue of Galaxies and Clusters of Galaxies. Caltech, Pasadena, 1961-1969.